Low-energetic Hadron Interactions in a Highly Granular Calorimeter

Dissertation

zur Erlangung des Doktorgrades
des Department Physik
der Universität Hamburg

vorgelegt von

Nils Feege

aus Haselünne

Hamburg
2011

Gutachter/in der Dissertation:	Prof. Dr. Erika Garutti Prof. Dr. Dieter Horns
Gutachter/in der Disputation:	Prof. Dr. Erika Garutti Prof. Dr. Peter Schleper
Datum der Disputation:	11. Januar 2012
Vorsitzender des Prüfungsausschusses:	Prof. Dr. Günter Huber
Vorsitzender des Promotionsausschusses:	Prof. Dr. Peter Hauschildt
Leiterin des Department Physik:	Prof. Dr. Daniela Pfannkuche
Dekan der MIN Fakultät:	Prof. Dr. Heinrich Graener

Abstract

The CALICE collaboration develops imaging calorimeters for precision measurements at a future electron-positron linear collider. These calorimeters feature a fine granularity in both longitudinal and transverse direction, which is needed to fulfill the shower separation requirement of Particle Flow reconstruction algorithms. CALICE has constructed prototypes for several design options for electromagnetic and hadron calorimeters and has successfully operated these detectors during combined test-beam programs at DESY, CERN, and Fermilab since 2005. The focus of this dissertation is on the prototype for a hadron calorimeter with analog readout (AHCAL), which is a $1\,\mathrm{m}^3$ scintillator-steel sampling calorimeter with 38 sensitive layers and a depth of 5.3 nuclear interaction lengths. Each scintillator layer is pieced together from separate tiles with embedded silicon photomultipliers (SiPMs) for measuring the scintillation light. With a total of 7608 readout channels, the AHCAL prototype represents the first large-scale application of SiPMs.

This thesis covers the commissioning and operation of the AHCAL and other detectors for several months at the Fermilab Test-beam Facility in 2008 and 2009 and the analysis of electron and pion data collected during these measurements. The analysis covers energies from 1 GeV to 30 GeV and is the first analysis of AHCAL data at energies below 8 GeV. Because the purity of the recorded data is not sufficient for analysis, event selection procedures for electrons and pions at these energies and a method to estimate the purities of these data samples are developed.

The calibration of detectors employing SiPMs requires parameters that change with operating voltage and temperature. The correction of these parameters for the effects of temperature variations during data collection and their portability to different operating conditions are evaluated using the AHCAL as an example. This is important for the use of this technology in a collider experiment where a re-calibration after installation is not feasible on short time scales. In addition, procedures to identify dead, noisy, and unstable cells in the AHCAL, which affect the detector performance especially at low particle energies, are introduced.

The analysis of low-energetic electron data (1 GeV to 20 GeV) presented in this thesis aims at evaluating the AHCAL performance, checking the detector calibration, and validating the understanding of both the detector and the simulations in this energy range. Detailed comparisons between pion data at low energies (2 GeV to 30 GeV) and different models implemented in the GEANT4 simulation toolkit are presented as well. This analysis allows for validating the simulations and studying the features of individual models and gives indications for possible refinements of the simulation of hadron cascades. The energy range covered by this analysis is particularly important because it includes the validity limits of several of the investigated models. The imaging capabilities of the AHCAL are exploited to extend the range of comparisons from the overall detector response to topological cascade features.

Zusammenfassung

Die CALICE Kollaboration entwickelt bildgebende Kalorimeter für Präzisionsmessungen an einem zukünftigen Elektron-Positron Linearbeschleuniger. Diese Kalorimeter zeichnen sich durch eine feine Segmentierung in longitudinaler und transversaler Richtung aus, die für die Schauer-Separation durch Particle Flow Rekonstruktionsalgorithmen benötigt wird. CALICE hat Prototypen für mehrere Designoptionen für elektromagnetische Kalorimeter und Hadronkalorimeter konstruiert und seit 2005 im Rahmen kombinierter Teststrahlmessungen am DESY, CERN, und Fermilab betrieben. Der Schwerpunkt dieser Dissertation liegt auf dem Prototypen für ein Hadronkalorimeter mit analoger Auslese (AHCAL), bei dem es sich um ein $1\,\mathrm{m}^3$ großes Szintillator-Stahl Samplingkalorimeter mit einer Tiefe von 5.3 nuklearen Wechselwirkungslängen handelt. Jede Szintillatorlage ist aus mehreren Ziegeln mit integrierten Silizium Photomultipliern (SiPM) zur Auslese des Szintillationslichts zusammengesetzt. Mit insgesamt 7608 Auslesekanälen ist das AHCAL die erste Anwendung von SiPMs im großen Maßstab.

Diese Arbeit behandelt die Inbetriebnahme und den Betrieb des AHCAL und anderer Detektoren für mehrere Monate an der Fermilab Teststrahlanlage in den Jahren 2008 und 2009 und die Analyse von Elektron- und Piondaten, die während dieser Messungen aufgezeichnet wurden. Die Analyse erstreckt sich über Energien von 1 GeV bis 30 GeV und ist die erste Analyse von AHCAL-Daten unterhalb von 8 GeV. Da die Reinheit der aufgezeichneten Daten für die Analyse nicht ausreicht, werden Kriterien zur Selektion von Elektronen und Pionen bei diesen Energien und eine Methode zur Abschätzung der Reinheit dieser Datensätze entwickelt.

Für die Kalibration von Detektoren, die SiPMs verwenden, werden Parameter benötigt, die sich mit Betriebsspannung und Temperatur ändern. Die Korrektur der Effekte von Temperaturänderungen auf diese Parameter während der Datennahme und die Portierung der Parameter zu unterschiedlichen Betriebsbedingungen werden für das AHCAL ausgewertet. Dies ist wichtig für die Verwendung dieser Technologie in einem Beschleunigerexperiment, bei dem eine Rekalibrierung nach der Installation nicht mehr auf kurzen Zeitskalen möglich ist. Es werden ferner Verfahren vorgestellt, um tote, stark rauschende, und instabile AHCAL-Zellen zu identifizieren, die das Detektorverhalten insbesondere bei niedrigen Energien beeinflussen.

Das Ziel der in dieser Arbeit vorgestellten Analyse niederenergetischer Elektrondaten (1 GeV bis 20 GeV) ist die Auswertung des AHCAL-Verhaltens, die Überprüfung der Detektorkalibration, und die Bestätigung des Verständnisses des Detektors und der Simulation in diesem Energiebereich. Außerdem werden detaillierte Vergleiche zwischen niederenergetischen Piondaten (2 GeV bis 30 GeV) und verschiedenen Modellen präsentiert, die in der GEANT4 Simulationssoftware implementiert sind. Diese Vergleiche erlauben die Überprüfung der Simulationen, die Untersuchung der Eigenarten einzelner Modelle, und geben Aufschluss über mögliche Verbesserungen der Simulation hadronischer Schauer. Der Energiebereich, den diese Analyse abdeckt, ist besonders wichtig, da er sich über die Gültigkeitsgrenzen mehrerer der untersuchten Modelle erstreckt. Das bildgebende Potential des AHCAL wird ausgenutzt, um die Vergleiche vom gesamten Detektorsignal auf topologische Schauereigenschaften auszudehnen.

Contents

Prelude **1**

1 Calorimetry in High-energy Physics **5**
1.1 Particle Interactions with Matter 5
1.1.1 Electrons and Photons: Electromagnetic Cascades 5
1.1.2 Muons and Charged Hadrons: Electromagnetic Processes 7
1.1.3 Hadrons: Strong Processes and Cascades 7
1.1.4 Čerenkov Radiation 10
1.2 Detection of Stable Particles 10
1.2.1 Calorimeter Response 11
1.2.2 Energy Resolution 12
1.3 Particle Flow Calorimetry 12

2 CALICE Detectors **15**
2.1 Data Acquisition System 16
2.2 The Silicon-tungsten Electromagnetic Calorimeter 16
2.3 Components of Calorimeters with SiPM Readout 17
2.3.1 Silicon Photomultiplier Technology 17
2.3.2 Very Front End Electronics 19
2.3.3 Calibration and Monitoring System 20
2.4 The Scintillator Electromagnetic Calorimeter 20
2.5 The Tail Catcher and Muon Tracker 21
2.6 The Analog Hadron Calorimeter 21
2.7 Calibration Scheme 24
2.8 Imaging Calorimetry 25

3 The CALICE Experiment at Fermilab **27**
3.1 The Fermilab Test-beam Facility 28
3.2 Experimental Setup 30
3.3 The Differential Čerenkov Detector at the FTBF 31
3.4 AHCAL Commissioning and Operation 36

4 Calibration Studies **43**
4.1 Cell Response Equalization with Muons . . . 43
4.2 Muon Calibration Portability . . . 45
4.3 Long-range Bias Voltage Scans . . . 48
4.4 Identifying Dead, Noisy, and Unstable Cells . . . 51
4.5 Uncertainties Induced by Varying Signal Thresholds . . . 55
4.6 Uncertainties Due to the Non-linear SiPM Response . . . 55

5 Simulation **57**
5.1 Simulating Particle Interactions with Matter . . . 57
5.1.1 Models for Hadron Cascade Physics . . . 58
5.1.2 GEANT4 Physics Lists . . . 62
5.2 Detector Modeling . . . 65
5.3 Digitization of Detector Effects . . . 66

6 Event Selection **69**
6.1 Algorithms Applied for Event Selection . . . 69
6.2 Beam Quality Criteria . . . 70
6.3 Electron Selection . . . 71
6.4 Pion Selection . . . 72
6.5 Muon Selection . . . 74
6.6 Event Selection Induced Systematic Uncertainties . . . 75
6.7 Data Purity . . . 75

7 Electron Analysis and Calibration Validation **83**
7.1 Linearity of the Electron Response . . . 84
7.2 Energy Resolution for Electrons . . . 88
7.3 Applying Non-native Muon Calibration Factors . . . 89
7.4 Longitudinal Electron Cascade Profiles . . . 91
7.5 Summary . . . 92

8 Pion Analysis **95**
8.1 Energy Measurement . . . 96
8.2 Longitudinal Pion Cascade Profiles . . . 100
8.3 Radial Pion Cascade Profiles . . . 106
8.4 Summary . . . 111

Summary and Outlook **115**

A Beam-line Simulation **119**

B Performance of Applied Algorithms **123**

C Event Selection Efficiencies **127**

D Supplementary Tables **131**

Bibliography **133**

Acknowledgments **139**

Prelude

Science is a systematic quest for fundamental principles that govern the universe. This quest has advanced human civilization, has brought major technological advances, and has relentlessly revealed previously unknown aspects of nature. A long list of achievements has nourished the ambitions of scientists to search for even more fundamental principles, to unify the observed particles and forces, and to trace the history of the universe back to the very beginning of time itself.

The Standard Model of particle physics [1, 2, 3] includes twelve fermions (six quarks and six leptons) as basic constituents of all visible matter and four forces determining the interactions between them. However, the origin of the masses of these particles is not utterly resolved yet. The Standard Model includes the Higgs mechanism to explain the emerging of masses, but this mechanism predicts an additional particle, the Higgs boson, which has not been observed by experiments yet. There are other limitations to the Standard Model. For example, astrophysical data have revealed a new type of massive matter, known as *dark matter*, which has never been observed directly by an experiment and which is not included in the Standard Model.

Collider experiments provide vital contributions to shape and validate models of nature. These experiments exploit the conversion from matter to energy and from energy to matter. The Large Hadron Collider (LHC) at CERN[1] collides protons with center of mass energies of up to $\sqrt{s} = 14\,\text{TeV}$ and has opened the door to the Terascale, an energy regime beyond the limits of previous collider experiments [4]. Exploring this regime makes the discovery of previously not measured particles like the Higgs boson, dark matter candidates, or even not predicted particles possible. However, the LHC has some limitations despite its great discovery potential. The colliding protons are compound objects comprising quarks and gluons. These constituents are the actually colliding objects and their momentum is only a fraction of the overall proton momentum, which is why the energy of each individual collision is not accurately known. Furthermore, the strong force gives rise to a strong background and to a considerable radiation exposure of the detectors. All these effects make precise measurements of parameters such as spin and parity of the Higgs boson or other particles extremely difficult.

The proposed International Linear Collider (ILC) is a precision machine that complements the measurements at the LHC [5]. At the ILC, electrons and positrons collide at a center of mass energy of $\sqrt{s} = 500\,\text{GeV}$. According to current knowledge, electrons and positrons are elementary particles. Therefore, the initial states of collisions at the ILC are well known. Furthermore, the events at the ILC expose the detectors to less radiation and have less background. This clean environment allows for highly precise measurements.

[1] Conseil Européenne pour la Recherche Nucléaire, Geneva, Switzerland

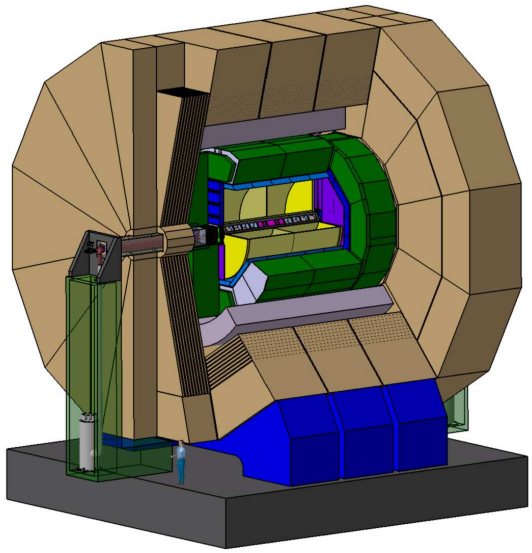

Figure 1: View of the ILD design [6]. See text for a description of the detector components.

Exploiting the full potential of the ILC demands a new generation of detectors. The ILC physics program is dominated by multi-boson processes resulting in final states with many jets. The intended physics analyses require a clear separation of jets originating from hadronic decays of W and Z bosons and therefore detectors with a jet energy resolution $\leq \frac{30\,\%}{\sqrt{E}}$. In addition, the detectors have to be close to hermetic to allow for the observation of missing energies in order to search for particles which leave no directly measurable signals. The International Large Detector (ILD, [6]) is designed to meet these requirements.

Figure 1 illustrates the layout of the current ILD design, which is typical for collider experiments. A vertex detector is the detector component closest to the interaction point and provides a high spacial resolution for identifying secondary vertizes. The main tracking device is a cylindrical time-projection chamber (with a diameter of about 3.6 m and a length of 4.3 m) which surrounds the vertex detector. An electromagnetic calorimeter and a hadron calorimeter enclose the tracking system and are encompassed by a magnetic coil. The inner diameter of the coil is 7.2 m and constrains the size of the calorimeters. The longitudinal magnetic field of several Tesla strength inside the detector bends the tracks of charged particles and allows the tracking system to measure the momenta of these particles from their curvatures. The outermost detector component is an iron return yoke for the magnetic flux with instrumented gaps holding a muon detection system. Different technology options are being investigated for the individual detector components.

The ILD design relies on Particle Flow reconstruction algorithms to reach the aspired jet energy resolution. This approach implies a close interplay between all detector components and sophisticated pattern recognition algorithms, i.e. detector hardware and software have to be developed interdependently. Particle Flow algorithms demand novel calorimeters featuring a fine granularity in both longitudinal and transverse direction to separate the signals from all individual particles in a jet. The CAlorimeter for the LInear Collider with Electrons (CALICE) collaboration investigates imaging calorimeters optimized for this purpose. This thesis focuses on the physics prototype for a scintillator-steel sampling calorimeter with analog readout for hadrons (AHCAL). Each scintillator layer of this detector is pieced together from separate $3 \times 3\,\mathrm{cm}^2$ tiles with embedded silicon photomultipliers

(SiPMs) for measuring the scintillation light.

General principles of measuring particle energies with calorimeters and the idea of Particle Flow are explained in Chapter 1. Chapter 2 describes the physics prototypes for the AHCAL and other calorimeters developed, built, and extensively operated by CALICE in an integrated setup at various test-beam facilities. Chapter 3 covers the commissioning and combined operation of the AHCAL and other CALICE detectors for several months at the Fermilab[2] Test-beam Facility and explains the beam line with its instrumentation. Electron and pion data collected at beam momenta from 1 GeV to 30 GeV during these measurements form the basis for the analysis presented in this thesis. This momentum range covers the typical hadron momenta in jets from hadronic decays of e.g. Z^0 bosons and is therefore particularly important for the operation of calorimeters in an ILD-like detector at the ILC and the application of Particle Flow algorithms.

Due to the fine segmentation, the number of readout channels for an imaging calorimeter at the ILD adds up to several million. Therefore, the calibration of these calorimeters requires robust procedures which can be commonly applied to all cells. Moreover, the calibration of calorimeters employing SiPMs requires parameters that change with operating voltage and temperature. Chapter 4 discusses the correction of these parameters for the effects of temperature variations during data collection and the portability of these parameters to different operating conditions using the example of the AHCAL physics prototype. The portability is vital for the use of calorimeters with SiPM readout in a collider experiment, where a (re-)calibration after installation takes a long time. This chapter also presents procedures to identify dead, noisy, and unstable cells in the AHCAL, which affect the stability and homogeneity of the detector response.

Simulations play a key role in physics analyses and in the development of new technologies like detectors for collider experiments. The predictive power of the simulations requires their prior validation with measurements. The GEANT4 toolkit provides simulations of particle interactions with matter [7]. While the modeling of electromagnetic cascades is well understood, the description of hadron cascades still needs validation and improvement. This validation is an important part of the CALICE efforts. GEANT4 provides different models for describing hadron cascades. Validating these models close to the limits of their applicability is particularly interesting. Chapter 5 presents GEANT4 and different models for hadron physics provided. Furthermore, this chapter explains the simulation of the AHCAL physics prototype and the incorporation of detector effects in the simulation (digitization).

Chapter 6 covers algorithms and event selection criteria applied to improve the purity of recorded electron and pion data. In addition, this chapter describes a procedure to quantify the purity of the data samples. The analysis of low-energetic electron data (between 1 GeV and 20 GeV) presented in Chapter 7 allows to evaluate the AHCAL performance, check the detector calibration, and validate the understanding of both the detector and the simulations in this energy range. These steps are prerequisites for the analysis of pion data and the validation of different Monte Carlo models implemented in GEANT4 (between 2 GeV and 30 GeV) presented in Chapter 8. The imaging capabilities of the AHCAL are exploited to extend the range of the comparisons between data and simulations from the overall detector response to topological shower features.

[2]Fermi National Accelerator Laboratory, Batavia, IL, USA

Chapter I

Calorimetry in High-energy Physics

Calorimetry in high-energy physics is the measurement of particle energies via detecting the energy deposited by these particles in matter during total absorption. Calorimeters are the devices utilized for these measurements. Usually, calorimeters provide additional information about the position, the direction, and the nature of absorbed particles. The way a particle deposits energy in an absorber medium depends on the type and energy of the particle and on the composition of the traversed material. Charged leptons and photons interact electromagnetically with the atoms of the absorber (the weak force and gravity are negligible for these particles), whereas the strong force governs the scattering of neutral hadrons with the absorber nuclei. Charged hadrons interact with the absorber atoms both via electromagnetic and strong processes. Each class of interactions involves different processes. The secondary particles generated by some of these processes interact again and a cascade develops.

Section 1.1 describes the basic physics of electromagnetic and hadronic cascades in matter, the emission of Čerenkov radiation, and other processes of energy deposition for charged particles. An overview of general calorimeter properties and figures of merit is given in Section 1.2. For a detailed treatment of all these topics, see References [8, 9]. The Particle Flow approach to calorimetry is briefly described in Section 1.3.

1.1 Particle Interactions with Matter

1.1.1 Electrons and Photons: Electromagnetic Cascades

Electrons (and positrons) traversing matter lose energy due to several electromagnetic processes, where the relative contributions of these processes to the total energy loss depend on the particle energy. Above about 10 MeV, the dominant process is energy loss via the emission of bremsstrahlung. This radiative energy loss is due to the deflection of electrons (and positrons) in the electric field of the absorber atoms. At lower energies, most energy is deposited in the absorber via ionization. Other processes contributing to a minor degree to the energy loss at low energies are Moeller scattering for electrons and Bhabha scattering and annihilation for positrons. Figure 1.1(a) summarizes these processes and their contribution at different energies for electrons and positrons in lead. The energy at which electrons lose as much energy via bremsstrahlung as via ionization defines the

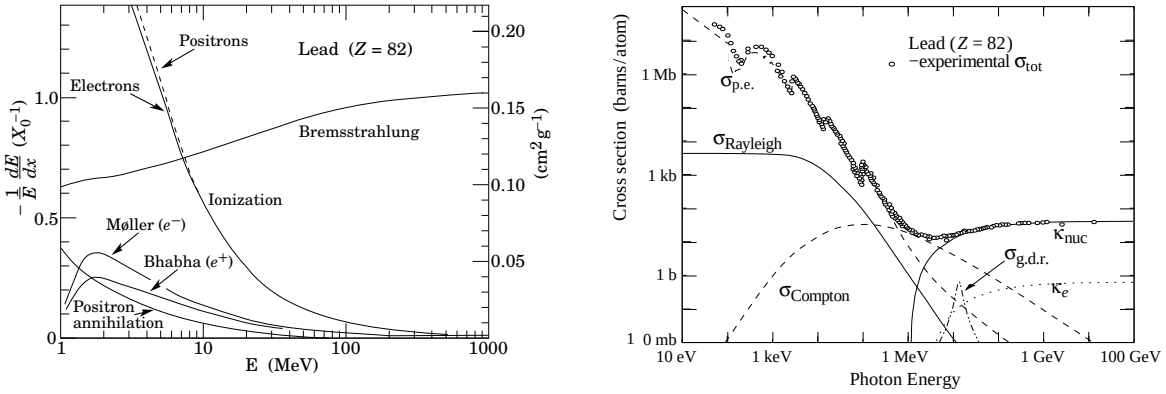

(a) (b)

Figure 1.1: (a) Fractional energy loss per radiation length in lead as a function of electron or positron energy. (b) Photon total cross sections as a function of energy in lead, showing the contributions of different processes. See text for more details. Both figures are taken from [10].

critical energy ϵ_c, which is about 7.42 MeV for lead and 21.04 MeV for iron [9]. Therefore, the intersection between radiative energy losses and energy losses due to ionization visible for lead in Fig. 1.1(a) is shifted to higher energies for iron. In addition to these processes, electrons can emit Čerenkov light. However, the contribution of this effect to the overall energy loss is negligible.

Photons passing through matter lose energy via different processes. Figure 1.1(b) summarizes these processes and their importance for different photon energies. For photon energies above twice the electron mass m_e, the electron-positron pair production in the field of a nucleus (κ_{nuc}) or atomic electrons (κ_e) is dominant. At low energies, photons lose most energy via the photo-electric effect ($\sigma_{p.e.}$). Another major energy loss process for photons is Compton scattering ($\sigma_{Compton}$). Minor processes are Rayleigh scattering ($\sigma_{Rayleigh}$) and photo nuclear interactions (mainly the giant dipole resonance, $\sigma_{g.d.r.}$).

The successive alternation of the emission of bremsstrahlung-photons (electrons and positrons) and electron-positron pair production (photons) multiplies the number of particles and leads to the development of an electromagnetic cascade. The cascade approximately reaches its peak multiplicity and starts to die out when the electrons (and positrons) reach the critical energy ϵ_c. The maximum shower depth increases logarithmically with the energy of the particle initiating the cascade.

A common scale for the description of electromagnetic cascades is the radiation length X_0, which is the distance after which a high-energetic electron traversing matter has lost $(1-e^{-1}) = 63.2\%$ of its initial energy. The radiation length of an absorber is approximated by

$$X_0 = \frac{716.4\,\mathrm{g\,cm^{-2}}A}{Z(Z+1)\ln(287/\sqrt{Z})}, \tag{1.1}$$

where A is the number of nucleons and Z the number of protons of the material [10]. The radiation length is correlated with the local energy loss $\left(\frac{dE}{dx}\right)_{brems}$ of an electron of energy E via bremsstrahlung, where $\left(\frac{dE}{dx}\right)_{brems} = \frac{E}{X_0}$.

High-energetic electrons (or positrons) traversing matter start emitting Bremsstrahlung immediately. In contrast to this, a photon entering matter may travel a certain distance

before converting to an electron-positron pair. The mean distance photons travel before pair production is the mean free path length I_γ and is related to the radiation length via $I_\gamma = \frac{9}{7}\mathrm{X}_0$.

The Moilère radius ρ_M is the radius of a cylinder containing 90% of the energy of an electromagnetic cascade (3.5 ρ_M correspond to 99% containment). Thus, this parameter describes the lateral extension of an electromagnetic shower. The Molière radius is given in [8] as

$$\rho_\mathrm{M} = 21.2\,\mathrm{MeV}\frac{\mathrm{X}_0}{\epsilon_\mathrm{c}}, \tag{1.2}$$

where ϵ_c is the critical energy.

1.1.2 Muons and Charged Hadrons: Electromagnetic Processes

Ionization is the main electromagnetic process of energy loss in matter for muons and heavier charged particles of moderate momenta ($\beta\gamma \approx 0.1 - 1000$). The emission of bremsstrahlung scales with energy E and mass m of a particle as $\frac{E}{m^4}$ and is therefore suppressed for these particles. The mean energy loss $\mathrm{d}E$ per path length $\mathrm{d}x$ for a particle of charge ze of moderate momentum traversing an absorber with atomic number Z and atomic mass A via ionization is given by the Bethe-Bloch formula

$$-\frac{\mathrm{d}E}{\mathrm{d}x} = \mathrm{K}z^2\frac{Z}{A}\frac{1}{\beta^2}\left(\frac{1}{2}\ln\frac{2m_\mathrm{e}c^2\beta^2\gamma^2T_\mathrm{max}}{I^2} - \beta^2 - \frac{\delta(\beta\gamma)}{2}\right)\,, \tag{1.3}$$

where T_max is the maximum energy that can be transfered to an electron of the absorber material in a single collision, I is the mean excitation energy, and K substitutes for a constant term including Avogadro's number, the elementary charge e, and the electron mass m_e. At relativistic energies, the electric field of charged particles flattens and extends until it is screened by polarization of the absorber atoms. The function $\delta(\beta\gamma)$ takes this density effect into account. Figure 1.2 presents the energy loss via ionization for muons traversing copper. The energy deposition has a broad minimum around $\beta\gamma \approx 3-4$. Particles having energies in this range are called minimum ionizing particles (MIPs). Below $\beta\gamma \approx 0.1$, additional corrections need to be applied [10]. Above $\beta\gamma \approx 1000$, energy losses due to radiation processes become dominant.

Charged particles with high momentum can transfer an amount of energy much larger than the ionization energy to an electron of the absorber atom, creating a so-called knock-on electron, or δ-ray. If their energy is high, these δ-ray electrons initiate an electromagnetic cascade as described in Section 1.1.1. At very high energies, the electromagnetic interactions of charged particles with the atoms of the absorber material can cause nuclear reactions. In addition, muons and charged hadrons can emit Čerenkov radiation, but the energy loss due to this effect is negligible.

1.1.3 Hadrons: Strong Processes and Cascades

Charged hadrons lose energy in matter via the electromagnetic processes described in Section 1.1.2. All hadrons passing through matter can scatter elastically or inelastically on the nuclei of the absorber. In elastic scattering processes, hadrons transfer part of their

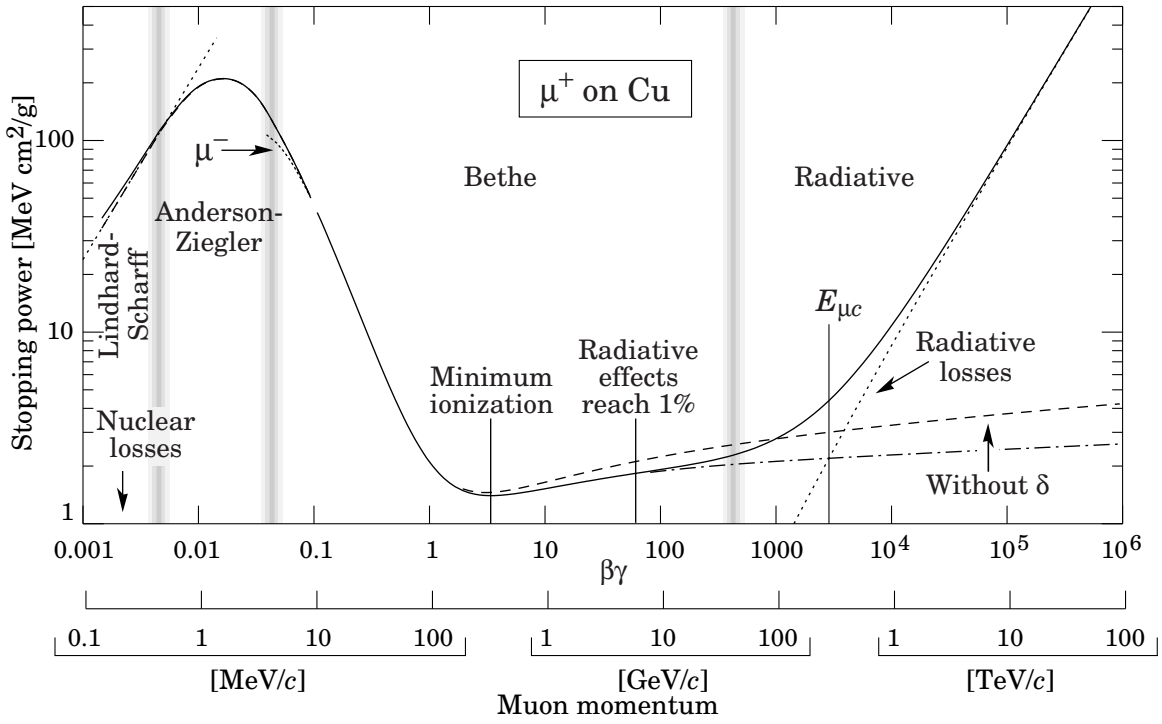

Figure 1.2: Energy loss (stopping power) for positive muons in copper over nine orders of magnitude in momentum (12 orders of magnitude in kinetic energy) from [10]. Solid curves indicate the total energy loss. Vertical bands indicate boundaries between different approximations. For moderate energies (labeled Bethe), the dominant energy loss process is ionization of absorber atoms and is described by equation 1.3.

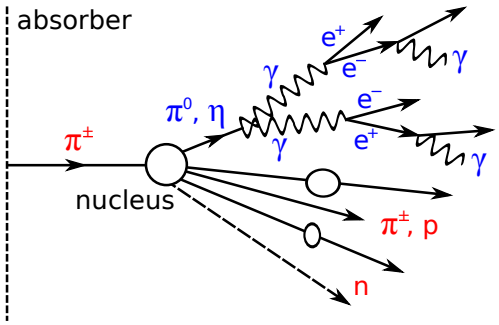

Figure 1.3: Illustration of a hadronic cascade: A hadron (e.g. a charged pion π^-) traverses the absorber medium until it scatters inelastically with an absorber nucleus and a variety of secondary particles is generated. Neutral mesons (π^0 and η) decay almost instantaneously into two photons γ and give rise to the electromagnetic fraction, i.e. a purely electromagnetic sub-cascade inside the hadron cascade (with electrons e^- and positrons e^+), whereas other hadrons (mainly charged pions $\pi^\pm$, protons p, and neutrons n) traverse the absorber until interacting strongly.

momentum to a nucleus and change their direction. In inelastic scattering interactions, the hit nucleus, the incident hadron, or both of them change their identity and various secondary particles can be generated. Most generated secondaries are charged or neutral pions ($\pi^{\pm}$ or π^0) or η mesons. Nuclear reactions release protons (p) and neutrons (n) from the struck nucleus.

The list of processes for hadron interactions leading to energy depositions in matter is diverse and includes spallation, fission, and breakup. In contrast to purely electromagnetic energy depositions, a significant amount of energy deposited by nuclear interactions in matter is invisible because it goes to the excitation or recoil of nuclei or is absorbed as nuclear binding energy. The energy from neutrinos generated in a hadron cascade is practically invisible as well.

Secondary hadrons (except for π^0s and ηs) created in inelastic hadron-nucleus scattering continue their way through the absorber until they interact again. The particle multiplicity increases and a cascade develops. As for electromagnetic cascades, the particle multiplicity reaches a maximum and the shower dies out eventually. The mean distance a high energetic hadron passes through a medium before interacting strongly with an atomic nucleus is given by the nuclear interaction length λ_{int} and defines the scale of hadronic cascades. Hadron cascades have a much larger spacial extension in a given absorber than electromagnetic showers. For example, the ratio between the nuclear interaction length and the radiation length $\frac{\lambda_{\text{int}}}{X_0}$ is about 9.5 for iron. The mean shower depth of hadron cascades increases with the logarithm of the hadron energy.

Neutral π^0s and ηs decay into two photons. This decay is almost instantaneous ($c\,\tau \approx 25\,\text{nm}$) due to its electromagnetic nature. The photons give rise to electromagnetic cascades as described in Section 1.1.1. The energy in a hadron shower deposited via these electromagnetic cascades is called the electromagnetic fraction f_{em} of the cascade and leads to similar average shapes of hadronic and electromagnetic cascades. The mean electromagnetic fraction and the similarity between hadronic and electromagnetic cascades increase with the energy of the hadrons initiating the cascades according to a power law

$$f_{\text{em}} = 1 - \left(\frac{E}{E_0}\right)^{k-1}, \tag{1.4}$$

where E is the energy of the hadron initiating a cascade, E_0 is the cutoff-energy for π^0 production, and $(k-1)$ is related to the multiplicity of π^0 mesons produced in single hadronic interactions [11, 12]. Typical values of E_0 are close to 1 GeV and k lies usually between 0.7 and 0.9. Because of the increase of the average electromagnetic fraction, the mean lateral extension of hadron cascades decreases with energy. Figure 1.3 illustrates a typical hadron cascade.

A special type of interaction are the so-called charge conversion reactions where the products of an incoming hadron scattering with an absorber nucleon are a hadron and a nucleon of different charge, e.g. $\pi^- + p \rightarrow \pi^0 + n$ [13, 14]. The resulting π^0 decays to two photons and the electromagnetic fraction of the hadron cascade is close to one, i.e. the hadron cascade looks like an electromagnetic cascade.

There are strong fluctuations from one hadron shower to another [15]. Many processes depositing different amounts of visible energy contribute to the inelastic hadron-nucleus interactions. Due to the random contributions from these processes, the electromagnetic

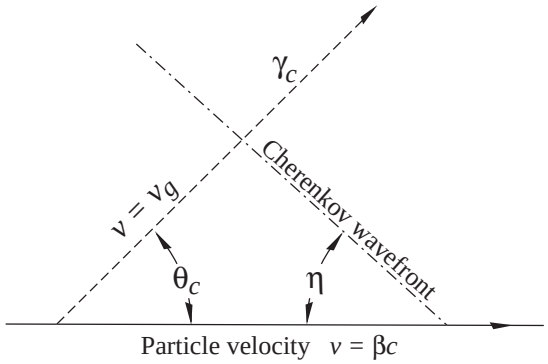

Figure 1.4: Čerenkov light emission and wavefront angles from [10]. The angle θ_c is the opening angle of the Čerenkov light cone. In a dispersive medium, $\theta_c + \eta \neq 90°$.

fraction and the overall visible energy vary. These fluctuations make hadron calorimetry especially challenging and limit the energy resolution that can be achieved by hadron calorimeters.

1.1.4 Čerenkov Radiation

Čerenkov light is emitted in a cone with opening angle θ_c with respect to the direction of motion of a particle if the velocity v of the particle in a dispersive medium of refractive index n is larger than the phase speed $\frac{c}{n}$ of light in this medium [10]. The opening angle θ_c is given by

$$\cos\theta_c = \left(\frac{1}{n\beta}\right) , \tag{1.5}$$

where $\beta = \frac{v}{c}$. Figure 1.4 illustrates the emission direction. Čerenkov light is generated because charged particles polarize excited atoms along their path. The contribution of Čerenkov radiation to the energy loss of charged particles is negligible. Nevertheless, Čerenkov light could be useful for calorimetry because measuring this light allows of estimating the electromagnetic fraction within hadronic cascades. This method is subject of ongoing research on dual-readout calorimeters but is not proven to work yet [16, 17, 18].

1.2 Detection of Stable Particles

Particle energy measurements with calorimeters exploit the scaling of the energy deposited by a cascade in matter with the energy of the particle initiating the cascade. These measurements require the total absorption of the particle energy in matter, or additional information about the energy fraction leaking from the detector. Therefore, the use of calorimeters in particle physics experiments is only feasible because the mean cascade length increases logarithmically with the energy of the cascade, which allows for containing even high-energetic cascades within a reasonable amount of absorber material.

There are two classes of calorimeter designs: homogeneous calorimeters and sampling calorimeters. Homogeneous calorimeters consist of only one material, which serves both as absorber and sensitive material. In contrast to this, sampling calorimeters consist of

insensitive absorber material and sensitive material, where most energy is deposited in the absorber material. However, the energy deposited in the sensitive areas is a measure of the energy of the whole cascade. The advantage of sampling calorimeters is the possibility to freely choose the absorber and the readout technology for the sensitive layers. For example, a high-density absorber could be chosen to yield the same shower containment (i.e. for the same radiation length X_0 or nuclear interaction lengths λ_{int}) as a homogeneous calorimeter at reduced dimensions (and cost). The optimization of size and containment is particulalry important if the calorimeter size is constrained, like e.g. in the case of Particle Flow detectors where the calorimeters have to fit inside the magnetic coil. Another feature of sampling calorimeters is the possibility of longitudinal segmentation, which allows for measuring the longitudinal distribution of the energy deposited by a cascade. The main drawback of sampling calorimeters is a worse energy resolution compared to homogeneous calorimeters due to sampling fluctuations, i.e. varying fractions of energy deposited in the sensitive and non-sensitive material.

Calorimeters are oftenly either optimized to measure electromagnetic or hadronic cascades, hence the separation in electromagnetic calorimeters (ECAL) and hadron calorimeters (HCAL). Due to the relation $\lambda_{\text{int}} > X_0$, hadron calorimeters need more or denser material to contain a given fraction of a cascade and to minimize leakage, i.e. to yield the same containment for hadrons as an electromagnetic calorimeter does for electrons, positrons, or photons of the same energy. However, hadron calorimeters can also measure electromagnetic cascades and vice versa. Some calorimeter designs are optimized to measure both electromagnetic and hadronic showers. The advantage of a combined calorimeter is the lack of transition effects and intercalibration between different detectors due to different sampling fractions, while the advantages of the separate approach are an independent optimization of both calorimeters for their specific needs and a reduction of the overall cost of the system.

1.2.1 Calorimeter Response

All energy deposited by an electromagnetic cascade in matter can, in principle, be detected. Due to the fact that some processes in hadron cascades deposit energy as invisible energy and the energy dependence of the mean electromagnetic fraction of hadronic cascades, the fraction of detectable energy deposited by a hadron cascade scales in a non-linear way with the cascade energy. The $\frac{e}{h}$ ratio is the ratio between the response of a calorimeter to a given amount of energy deposited by a purely electromagnetic and a purely hadronic cascade, which is a theoretical quantity that cannot be measured directly due to the electromagnetic fraction of real hadron cascades. Calorimeters for which this ratio is not one are called non-compensating.

A careful choice of absorber and sensitive materials and the respective dimensions allows to artificially increase the hadron response of a calorimeter (with respect to the electromagnetic response) to compensate for invisible energy depositions, i.e. to tune the e/h ratio to approach unity [19]. Calorimeters with calorimeters with $\frac{e}{h} = 1$ are called compensating. The calorimeters built so far with e/h ratios closest to one use depleted uranium as absorber material and organic scintillators as sensitive material [20, 21]. In the absorber plates, the fission processes induced in the hadronic part of hadronic cascades contribute additional energy in the form of nuclear photons and soft neutrons, which can be

detected particularly well with organic scintillators (because of the large hydrogen content of these materials).

The response of non-compensating calorimeters to hadrons is not linear because of the energy dependence of the electromagnetic fraction f_{em} in hadron showers parametrized by Eq. (1.4). The $\frac{\pi}{e}$ ratio is the ratio between the response of a calorimeter to pions and electrons of the same energy and can be described by

$$\frac{\pi}{\mathrm{e}} = \frac{1 - f_{\mathrm{em}}\left(1 - \frac{e}{h}\right)}{\frac{e}{h}}. \tag{1.6}$$

In contrast to $\frac{e}{h}$, the $\frac{\pi}{e}$ ratio can be determined experimentally. However, detector effects like signal thresholds or noise influencing the response linearity of a calorimeter also affect the $\frac{\pi}{e}$ ratio and have to be accounted for to extract the theoretical quantity $\frac{e}{h}$ from measurements of the $\frac{\pi}{e}$ ratio.

1.2.2 Energy Resolution

The energy resolution $\frac{\sigma_E}{E}$ of a calorimeter is a function of the cascade energy E and can be parametrized by

$$\frac{\sigma_E}{E} = \frac{a}{\sqrt{E}} \oplus b \oplus \frac{c}{E} = \sqrt{\left(\frac{a}{\sqrt{E}}\right)^2 + (b)^2 + \left(\frac{c}{E}\right)^2}, \tag{1.7}$$

where a is the stochastic term. Depending on the calorimeter design and the type of the incoming particle, different types of fluctuations dominate this term. For sampling calorimeters with solid sensitive material, the main contribution when measuring electron or photon energies are the sampling fluctuations. In case of hadron measurements, the intrinsic fluctuations of the hadronic cascade development become dominant. The constant term b takes into account calibration uncertainties, response inhomogeneities of the sensitive areas, and leakage effects. The relative contribution of this term is the same for all particle energies. The noise term c reflects electronics noise and background signals. The noise is independent from the particle energy and therefore the relative contribution of the noise to the overall signal decreases with the particle energy. At low energies, the noise term limits the resolution achieved by a calorimeter, while at higher energies the constant term is the resolution limiting factor.

Examples for calorimeters with very good energy resolutions employed by high-energy physics experiments are the homogeneous lead-tungstate electromagnetic calorimeter used by the CMS experiment with an energy resolution of $\frac{2.8\,\%}{\sqrt{E}}$ for single electrons [22] and the compensating scintillator-uranium sampling calorimeter for hadrons used by the ZEUS experiment with a hadron energy resolution of $\frac{35\,\%}{\sqrt{E}}$ [23].

1.3 Particle Flow Calorimetry

In high-energy physics experiments at colliders, typically hadron jets are measured rather than single particles. The jet energy resolution is usually worse than the energy resolution

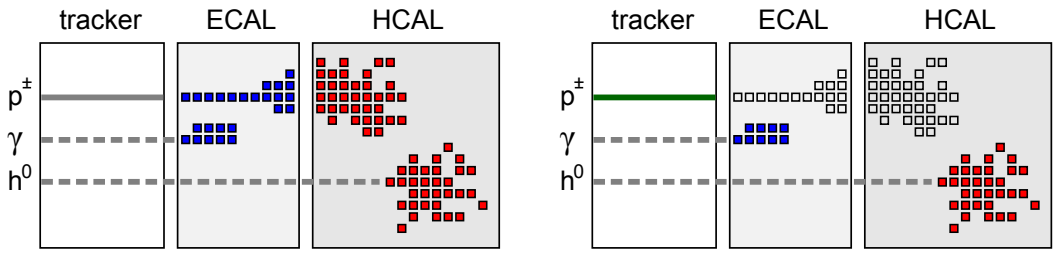

Figure 1.5: (a) Simple calorimetry: The calorimeters (ECAL + HCAL) measure the total energy deposited by all particles in a jet (charged particles $p^{\pm}$, photons γ, and neutral hadrons h^0). The track information is not used. (b) Particle Flow approach: The tracking system measures the energy of all charged particles (via the particle momentum) and the associated energy depositions are removed from the calorimeters. Photon energies are measured with the ECAL and neutral hadron energies are measured with the HCAL (and the ECAL, if the cascade starts already in the ECAL).

for single hadrons due to transition regions between individual detector components, different sampling fractions of different subdetectors, and not instrumented regions. The Particle Flow approach is a promising strategy to improve the jet energy resolution to $\sigma_{\text{jet}} \leq \frac{30\,\%}{\sqrt{E}}$ for an integrated detector system with tracker, electromagnetic calorimeter, and hadron calorimeter by employing sophisticated pattern recognition algorithms [24, 25, 26].

On average, charged particles account for $f_{\text{p}^{\pm}} \approx 60\,\%$ of the energy of a jet. Photons contribute with $f_{\gamma} \approx 30\,\%$ to the jet energy, and neutral hadrons constitute the remaining $f_{\text{h}^0} \approx 10\,\%$. Particle Flow algorithms reconstruct each individual particle in a jet and use the energy measurements from the detector component with the best resolution for the respective particle type. In order to put this into practice, the calorimeters need to be capable of clearly separating individual showers, i.e. each energy deposition has to be associated with the correct particle. Figure 1.5 illustrates the Particle Flow approach and shows a typical detector setup with a tracking system, an electromagnetic calorimeter, and a hadron calorimeter and the signatures of a charged hadron, a photon, and a neutral hadron. Without applying Particle Flow, the energy of these three particles (Fig. 1.5(a)) is measured by summing up all energy deposited in the calorimeters, thereby ignoring the tracker information. In Particle Flow calorimetry (Fig. 1.5(b)), the energy depositions from charged particles are removed from the calorimeter measurements and the momentum measurements from the tracker are used for these particles instead. Photons are measured with the electromagnetic calorimeter and neutral hadrons with the hadron calorimeter and partially with the electromagnetic calorimeter, if the cascade starts already in this detector.

The energy resolutions σ_{track} of the tracker, σ_{em} of the electromagnetic calorimeter, and σ_{had} of the hadron calorimeter contribute to the jet energy resolution with the weight of the particle type the respective detector measures. Wrong assignments of cascades, or parts of cascades, to charged or neutral particles contribute with a confusion term σ_{conf} to the resolution and constitute the resolution limiting factor in Particle Flow calorimetry. Other effects degrading the resolution are energy losses from particles that are not reconstructed (σ_{loss}) and effects of detector thresholds (σ_{thr}). Summing up all these contributions, the

jet energy resolution for a detector applying a Particle Flow algorithm is

$$\sigma^2_{\text{jet}} = f_{\text{p}^\pm}\sigma^2_{\text{track}} + f_\gamma\sigma^2_{\text{em}} + f_{\text{h}^0}\sigma^2_{\text{had}} + \sigma^2_{\text{conf}} + \sigma^2_{\text{thr}} + \sigma^2_{\text{loss}} \,. \tag{1.8}$$

Detector optimization for Particle Flow aims for minimizing the contributions from σ_{conf} by improving the separation of cascades from different particles and σ_{loss} by minimizing gaps, uninstrumented areas, and leakage. Chapter 2 describes the designs and the physics prototypes for highly granular imaging calorimeters with analog readout designed by the CALICE collaboration for this purpose.

The high granularity of imaging calorimeters developed for Particle Flow detectors supports the application of software compensation algorithms [27]. These algorithms reweight measured energy depositions from hadronic cascades based on local energy densities and the shower shapes to correct for fluctuations in the visible energy in order to improve the linearity of the response and the energy resolution of the detector.

Chapter II

CALICE Detectors

The CALICE collaboration conducts research on imaging calorimeters for Particle Flow detectors. Imaging calorimeters feature a fine granularity in both longitudinal and transverse direction, which is needed to fulfill the shower separation requirement of Particle Flow reconstruction algorithms. CALICE realizes its designs for electromagnetic and hadron calorimeters as physics prototypes and operates these detectors during combined test-beam measurements. The objectives of this program are diverse. The recorded data allow for evaluating the new technologies, prooving the principle of Particle Flow reconstruction algorithms, and studying hadron showers in great detail to validate and refine the simulation models of these showers. The pursuit of these goals profits from the integrated operation of electromagnetic and hadron calorimeters with a joint data acquisition system (DAQ) and the same beam-line instrumentation. Furthermore, CALICE benefits from synergies by employing common technologies for different calorimeters.

CALICE investigates four sampling calorimeter designs with analog readout: an analog hadron calorimeter (AHCAL), a tail catcher and muon tracker (TCMT), a scintillator-tungsten electromagnetic calorimeter (Sci-ECAL), and a silicon-tungsten electromagnetic calorimeter (Si-W ECAL). The sensitive layers of the AHCAL, the TCMT, and the Sci-ECAL are pieced together from separate tiles or strips. Silicon photomultipliers (SiPMs) measure the scintillation light from each cell. The silicon layers of the Si-W ECAL are subdivided into separate readout pads. Physics prototypes for these designs have been built and successfully operated during combined test-beam measurements at DESY[1], CERN, and Fermilab [28, 29, 30]. In addition to analog technologies, CALICE develops imaging calorimeters with digital or semi-digital readout of the sensitive layers (using Gas Electron Multiplier foils, Micromegas, or Resistive Plate Chambers). However, these technology options are not discussed in this thesis.

The DAQ used by all CALICE physics prototypes with analog readout is briefly described in Section 2.1. Section 2.2 presents the Si-W ECAL physics prototype. Section 2.3 gives an overview of the SiPM technology and other components used by all CALICE detectors with SiPM readout. The designs of the Sci-ECAL, the TCMT, and the AHCAL are covered by Sections 2.4, 2.5, and 2.6. The main focus lies on the AHCAL because the analysis presented in this thesis is based on this detector. Section 2.7 discusses the calibration scheme commonly applied to all calorimeters with SiPM readout. Finally, the imaging

[1] Deutsches Elektronen SYnchrotron, Hamburg, Germany

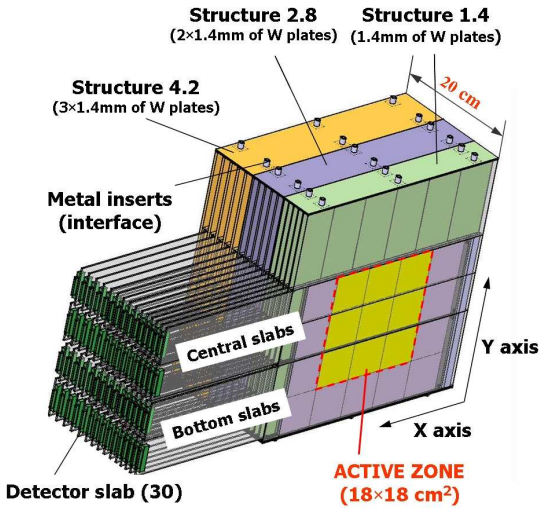

Figure 2.1: The physics prototype of the Si-W ECAL [32].

capabilities of the CALICE detectors and an integrated setup with several calorimeters are illustrated in Section 2.8.

2.1 Data Acquisition System

CALICE uses a central DAQ for recording the signals from all calorimters used in an integrated setup simultaneously. The central components of the DAQ for the detectors with analog readout are the CALICE readout cards (CRCs, [31]). These cards comprise 16-bit analog to digital converters (ADCs) for digitizing the analog signals from the very front end electronics of the calorimeters before routing them to a PC (one ADC level corresponds to 76 μV input signal). The CRCs are built into a VME crate and connected to it via the back-end (BE) panel. The CRCs also control and distribute trigger information. The BE panel provides the trigger logic that can be steered via software. The trigger signal is distributed to the CRCs via the BE panel, where a common trigger decision is used for all calorimeters and the data from all detectors are stored together.

2.2 The Silicon-tungsten Electromagnetic Calorimeter

The Si-W ECAL is a sampling calorimeter optimized for measuring electromagnetic showers. Figure 2.1 presents the design of the Si-W ECAL physics prototype. The absorber structure of this detector consists of 30 tungsten absorber layers grouped in three modules. The tungsten layers of the first module are 1.4 mm thick, the layers of the second group are 2.8 mm thick and the layers of the third module are 4.2 mm thick. The tungsten layers are interleaved with 30 sensitive layers. The silicon of these layers is segmented into pads measuring $1 \times 1\,\mathrm{cm}^2$ and functioning as a PIN diodes. The sensitive area of the detector is $18 \times 18\,\mathrm{cm}^2$, which results in a total of 9720 readout channels. The depth of the Si-W ECAL prototype is 24 radiation lengths, or about one nuclear interaction length. A more detailed description of the design is given in [32].

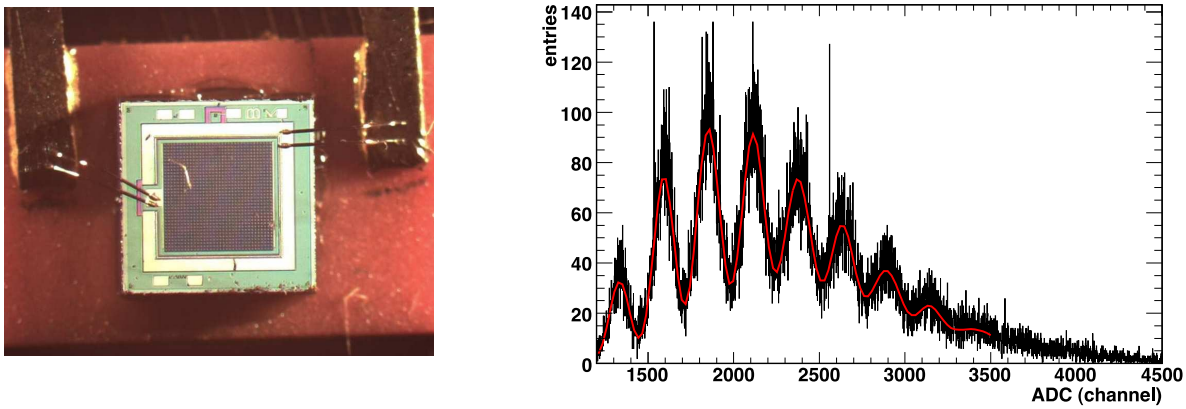

(a) (b)

Figure 2.2: (a) A SiPM as it is used for the AHCAL physics prototype. The device consists of an array of 34×34 pixels on an area of $1\,\mathrm{mm}^2$. (b) Single pixel spectrum of an individual SiPM that is used for measuring the SiPM gain [33]. A multi-gaussian fit is performed on the spectrum to determine the distance of consecutive peaks.

2.3 Components of Calorimeters with SiPM Readout

2.3.1 Silicon Photomultiplier Technology

Silicon Photomultipliers are novel semiconductor devices for measuring light intensities with a gain comparable to that of conventional photodetectors like photomultiplier tubes (PMTs) [34, 35, 36]. The advantages of SiPMs over PMTs are their small size of only few mm^2, their low operating voltage of less than 100 V, and their insensitivity to magnetic fields. These features allow for using SiPMs directly inside experimental setups and make light guides to external PMTs dispensable.

Silicon photomultipliers are built from a pixel array of pn-diodes. Figure 2.2(a) shows one of the SiPMs produced for the AHCAL physics prototype. These devices comprise 34×34 pixels on an area of $1\,\mathrm{mm}^2$. Each pixel operates in Geiger mode, i.e. its reverse bias voltage U_{bias} is larger than its breakdown voltage U_{bd}. Free electrons generated via the absorption of photons in the depletion region are accelerated by the electric field in this region and can trigger a self-sustaining electron avalanche, which is termed Geiger discharge, or *firing*, of a pixel. Adding a resistor (with adequate resistivity R_{q}) quenches the avalanche and allows the pixel to recover after the time $\tau = R_{\mathrm{q}} \cdot C_{\mathrm{pix}}$. The capacitance C_{pix} of a single pixel depends on the pixel geometry and on the silicon doping. Random Geiger discharges, which can be initiated by electrons from thermal excitation, give rise to the noise and dark current of a SiPM. Photons created by a Geiger discharge may trigger an avalanche in an adjacent pixel and cause optical inter-pixel crosstalk.

The gain G of a silicon photomultiplier (which is the number of electrons generated during a Geiger discharge) is given by

$$G = C_{\mathrm{pix}} \cdot (U_{\mathrm{bias}} - U_{\mathrm{bd}})/e \,, \tag{2.1}$$

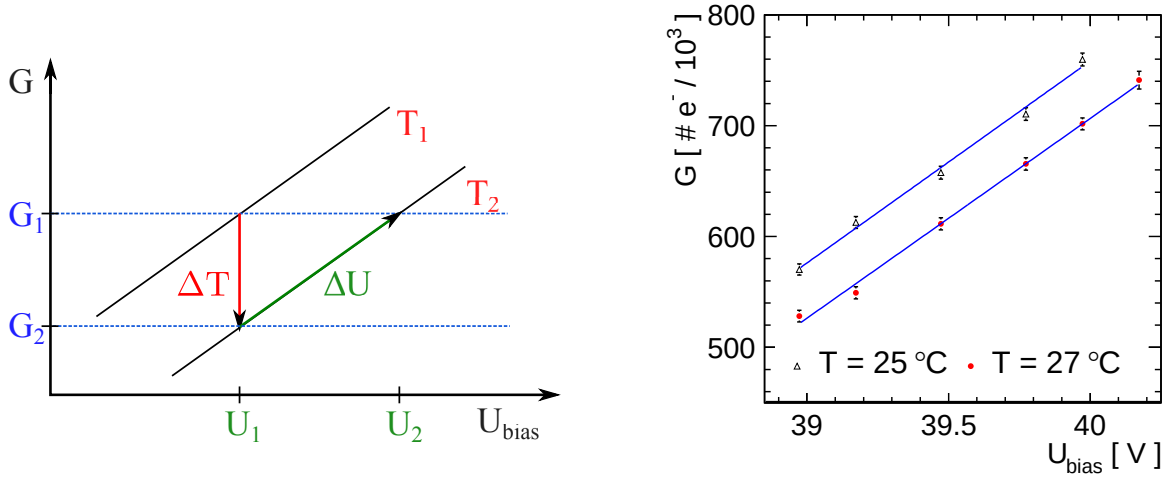

(a) (b)

Figure 2.3: (a) Sketch of the bias voltage U and temperature T dependence of the SiPM gain [37]. The gain increases (decreases) linearly with increasing bias voltage (temperature). Adjusting the bias voltage compensates temperature changes. (b) The gain G of a single AHCAL SiPM as a function of the operating voltage U_{bias} for two different temperatures T [37].

where e is the elementary charge [35]. The gain is measured with the SiPM itself, i.e. SiPMs are self-calibrating devices. Figure 2.2(b) shows the SiPM response to pulsed light of low intensity from a light-emitting diode (LED). The first peak in this spectrum is the pedestal, the second peak corresponds to one pixel firing, the third to two pixels firing, and so on. Therefore, the gain is given by the difference between two adjacent peaks.

According to Eq. (2.1), G depends linearly on the difference between U_{bias} and U_{bd}. Because U_{bd} increases with temperature, G decreases with rising temperature for fixed U_{bias}. Figure 2.3(a) illustrates the dependence of the SiPM gain on bias voltage and operation temperature. Furthermore, this sketch illustrates the possibility to compensate the effect of temperature variation on the gain by adjusting the bias voltage. Figure 2.3(b) presents a measurement of these dependencies for a SiPM from the AHCAL physics prototype.

The photon detection efficiency ε of a SiPM is the product of three independent parameters: the ratio between the sensitive area and the total SiPM surface (geometrical efficiency ε_{A}), the probability for a photon inside the depletion region to generate an electron hole pair (quantum efficiency ε_{Q}), and the probability for a free electron in the depletion region to trigger a Geiger discharge (Geiger efficiency ε_{G}). Like G, ε_{G} (and therefore ε) depends on the difference $U_{\text{bias}} - U_{\text{bd}}$. However, in contrast to G, ε_{G} saturates at 100 % for large $U_{\text{bias}} - U_{\text{bd}}$. SiPMs are usually operated below this saturation region.

The signal from a single pixel is independent from the number of absorbed photons. However, the combination of several pixels in an array allows for an analog measurement of light intensity. The total response A of a SiPM to incident light is a function of the number N_γ of photons hitting the device. These photons generate $N_{\text{ph.e.}}$ photo electrons. This number is determined by $N_{\text{ph.e.}} = N_\gamma \cdot \varepsilon \cdot (1 + \kappa)$, where κ is the probability for optical inter-pixel crosstalk. The SiPM response saturates for large $N_{\text{ph.e.}}$, since the number of pixels N_{pix} is limited and a pixel cannot fire again while recovering. Figure 2.4 shows

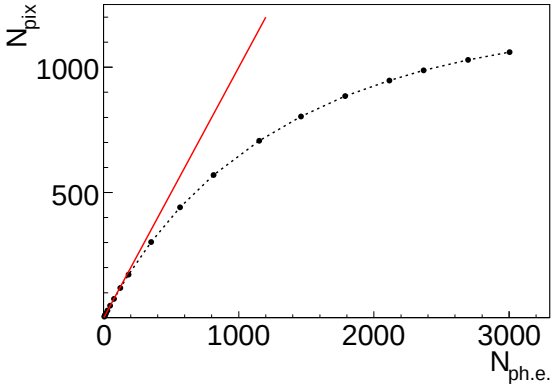

Figure 2.4: SiPM response as a function of increasing light intensity [37]. For a linear device, this relation would follow the solid line. The dots show the response curve for a SiPM. The saturation of this curve is caused by the limited number of SiPM pixels.

the relation between $N_{\text{ph.e.}}$ and N_{pix} for a SiPM used in the AHCAL physics prototype (measured with the fully assembled calorimeter). The solid line indicates the equality between $N_{\text{ph.e.}}$ and N_{pix}. In this case, κ is absorbed in the calibration of $N_{\text{ph.e.}}$. Thus, A is given by

$$A(N_\gamma) = f_{\text{pix}}(N_\gamma \cdot \varepsilon) \cdot G \cdot e \ . \tag{2.2}$$

The function $f_{\text{pix}}(N_{\text{ph.e.}})$ gives the real number of firing pixels taking saturation into account. The larger $N_{\text{ph.e.}}$ becomes, the more the observed relation deviates from linearity.

Because A is a function of G and ε, the sensitivity of A to voltage and temperature changes is the sum of the respective dependencies of G and ε. Therefore, measuring light intensities with SiPMs requires knowledge of the gain, the photon detection efficiency, and the saturation behavior of the devices under the conditions (bias voltage, temperature) of the measurement.

2.3.2 Very Front End Electronics

Printed circuit boards (PCBs) comprise the very-front-end electronics (VFE) of the CALICE detectors with SiPM readout [31]. Each board comprises 12 application specific integrated circuit chips (ASICs). The chips are a development of the Laboratoire de l'Accélérateur Linéaire (LAL) in France and are based on the readout chips for the Si-W ECAL [32]. The ASICs amplify and shape the SiPM signals. Due to this shaping, these signals are delayed and reach their maximum after the generation of a trigger decision (e.g. in a test-beam setup). The time between the trigger decision and the signal maximum needs to be measured and provided to the chip. Each ASIC processes the signals from 18 SiPMs and guides the multiplexed output to the external DAQ.

The ASICs are operated in two modes. The physics mode (PM) features a nominal amplification of $G^{\text{PM}} = 8.18\,\frac{\text{mV}}{\text{pC}}$ and a shaping time of 150 ns. This mode provides the needed dynamic range for measuring energy depositions in the calorimeter. The calibration mode (CM) features a nominal gain of $G^{\text{CM}} = 92.3\,\frac{\text{mV}}{\text{pC}}$ and a shaping time of 40 ns. The high amplification allows for resolving single pixel spectra for measuring the SiPM gain. The electronics intercalibration factor IC_{i} of a readout channel i is the ratio between a

SiPM signal measured in physics mode ($A_{\mathrm{i}}^{\mathrm{PM}}$) and the same signal measured in calibration mode ($A_{\mathrm{i}}^{\mathrm{CM}}$):

$$IC_{\mathrm{i}} = \frac{A_{\mathrm{i}}^{\mathrm{PM}}}{A_{\mathrm{i}}^{\mathrm{CM}}} \,. \tag{2.3}$$

This factor depends not only on the ratio between the amplifications of the two modes, but due to different integration times also on the shape of the SiPM signal. The boards supporting the ASICs amplify the signal by an additional factor of two.

The optimal bias voltage differs from SiPM to SiPM. The digital to analog converters (DACs) on the ASICs allow for adjusting the voltages, which are commonly supplied for groups of SiPMs, for each channel individually.

2.3.3 Calibration and Monitoring System

The calibration and monitoring boards (CMBs) developed by CALICE provide LED light for calibrating SiPMs and for monitoring their operation stability [31]. The monitoring is important because of the sensitivity of the SiPM signals to voltage and temperature changes. A CMB comprises 12 UV LEDs and 12 PIN photodiodes (Hamamatsu SFH250) for monitoring the LEDs. A Controller-area Network bus (CAN-bus) connection is used to control the LEDs. In addition, the CMBs comprise a 12-bit ADC for digitizing the readout from temperature sensors in the calorimeters before transferring it via the CAN-bus connection to the slow-control system and the DAQ. The CMBs are used by the Sci-ECAL and the AHCAL physics prototypes, whereas the TCMT uses a different LED system based on the same principles.

The LED system is used to illuminate SiPMs with low intensity light (1-5 generated photoelectrons, < 10 ns pulse width). Recording the responses in calibration mode allows for measuring and monitoring the SiPM gains. Another CMB application is the illumination of SiPMs with light of higher intensity to monitor the response change with time and operating conditions in physics mode. A third purpose of the CMBs is to generate response curves by stepwise increasing the LED intensity and measuring the SiPM response in calibration and physics mode. The ratios of these curves provide the intercalibration factor of each channel. The response curves recorded in physics mode and approaching full saturation allow for measuring the maximum number of SiPM pixels that can be illuminated [37].

2.4 The Scintillator Electromagnetic Calorimeter

The Sci-ECAL consists of 30 tungsten absorber plates and 30 sensitive scintillator layers. Figure 2.5(a) shows a picture of this detector. The absorber plates are each 3.5 mm thick. Each scintillator layer is divided into four rows of 18 scintillator strips, where strips in consecutive layers are oriented orthogonally to each other. The strips are 45 mm long, 10 mm wide, and 3 mm thick. The scintillation light from each strip is collected by a wavelength shifting fiber (WLS) and guided to a multi-pixel photon counter (MPPC). The Sci-ECAL physics prototype employs 2160 MPPCs (with 1600 pixels) produced by Hamamatsu [40, 41]. The working principles of SiPMs explained in Section 2.3.1 and

(a) (b)

Figure 2.5: Pictures of (a) the Sci-ECAL [38] and (b) the TCMT absorber structure [39].

MPPCs are the same. The lateral extension of the sensitive area of the Sci-ECAL is $18 \times 18\,\mathrm{cm}^2$. The depth of this detector is 21.5 radiation lengths. More details on this device are given in [38].

2.5 The Tail Catcher and Muon Tracker

The TCMT is a scintillator-steel sampling calorimeter. The absorber structure consists of 16 steel plates measuring $1 \times 1\,\mathrm{m}^2$ and is depicted in Fig. 2.5(b). The first eight plates are 2 cm thick, whereas the other eight plates are 10 cm thick. The first sensitive layer is placed in front of the first absorber layer. The scintillator material of the 16 sensitive layers is segmented into 20 parallel strips. Each strip is 1 m long, 5 cm wide, and 5 mm thick. The orientation of the strips alternates by 90 degrees between consecutive layers. The scintillation light from each strip is collected by a WLS and guided to a SiPM. The total thickness of the TCMT is 5.5 nuclear interaction lengths. A more detailed description of the TCMT is given in [39]. The main usage of the TCMT is to measure leakage from hadron showers in the AHCAL. In addition, it is used to identify muons.

2.6 The Analog Hadron Calorimeter

The AHCAL physics prototype is a scintillator-steel sandwich calorimeter [31]. The 39 absorber plates (which measure $1 \times 1\,\mathrm{m}^2$ and are approximately 17 mm thick) of the detector are interleaved with 38 modules housing the scintillator material. The front and back covers of the modules each add 2 mm of steel to the absorber material. The scintillator layers are 5 mm thick and are pieced together from separate tiles. A WLS collects the light from each tile and guides it to a SiPM. Altogether, the AHCAL physics prototype comprises 7608 readout channels and has a depth of 5.3 nuclear interaction lengths λ_n or 4.3 pion interaction lengths λ_π.

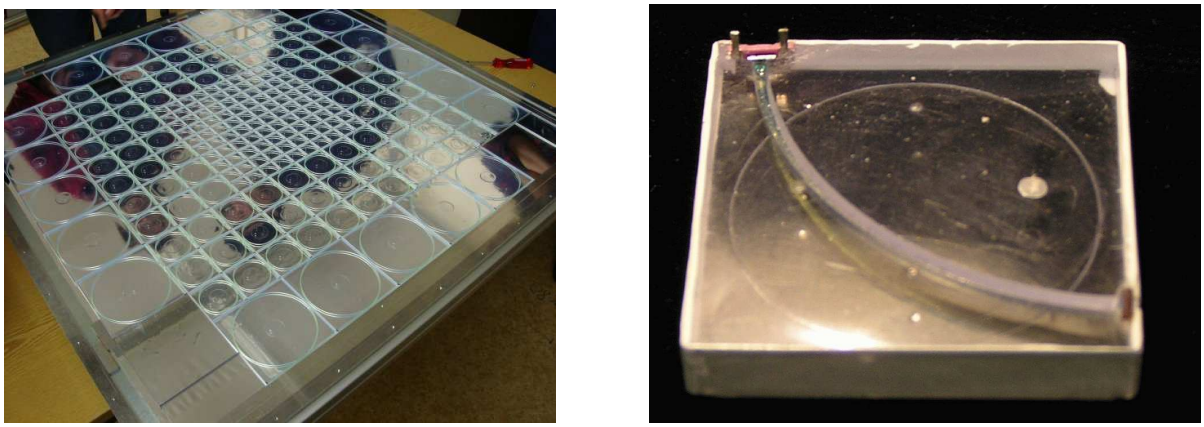

(a) (b)

Figure 2.6: (a) A single AHCAL layer with 216 separate scintillator tiles [31]. (b) A $3 \times 3\,\mathrm{cm}^2$ scintillator tile with SiPM, mirror, and WLS [37].

The layout of the AHCAL physics prototype modules is illustrared in Fig. 2.6(a) and Fig. 2.7. The center part of these modules is a steel cassette ($1 \times 1\,\mathrm{m}^2$ in size), which houses 216 scintillator tiles. The 100 central tiles measure $3 \times 3\,\mathrm{cm}^2$ and are surrounded by 96 tiles which are $6 \times 6\,\mathrm{cm}^2$ in size and an outer ring of 20 tiles measuring $12 \times 12\,\mathrm{cm}^2$. Eight modules have a coarser granularity with 25 additional $6 \times 6\,\mathrm{cm}^2$ tiles replacing the $3 \times 3\,\mathrm{cm}^2$ tiles. Figure 2.7 also indicates the positions of the attached CMB and the VFE boards. Nine temperature sensors (LM35D from National Semiconductor) are distributed over each module. Five sensors reside inside the central cassette, two on the CMB, and two on the VFE board.

Figure 2.6(b) displays a $3 \times 3\,\mathrm{cm}^2$ tile. The tiles are made from organic scintillator material (BASF 143 from UNIPLAST). The spectrum of the scintillation light peaks at 430 nm. Each tile has a groove with an embedded WLS (Y11, 300 ppm from Kuraray). This fiber absorbs the UV scintillation light and re-emits light with a peak wave length of 500 nm. One end of the fiber is covered by a mirror, the other end guides the light to the SiPM connected to the tile. Top and bottom side of each tile are covered by reflective foil (VN2000 super-radiant from 3M). A chemical treatment of the tile edges minimizes light losses and optical crosstalk to neighboring tiles.

The AHCAL physics prototype employs SiPMs comprising 34×34 pixels on an area of $1\,\mathrm{mm}^2$ (produced by the Moscow Engineering and Physics Institute (MEPhI) and Pulsar Enterprise [42, 43]). The capacitance of a single pixel of 50 fF and the quenching resistors of 2 to 20 MΩ yield a recovery time of $100 - 1000$ ns. The SiPMs are operated at Geiger efficiencies of $90 - 95\,\%$. The gain within this SiPM sample ranges from $0.9 \cdot 10^6$ to $2.5 \cdot 10^6$. The devices are most sensitive to green light. Their geometrical efficiency is approximately $20 - 35\,\%$ and their quantum efficiency is about $80\,\%$. The majority of these SiPMs is operated at an average reverse bias voltage of about 3.8 V above the breakdown voltage. The mean gain variation with voltage and temperature of these SiPMs is $2.6\,\frac{\%}{100\,\mathrm{mV}}$ and $-1.7\,\frac{\%}{\mathrm{K}}$.

The signal-to-noise ratio (SNR) and the dynamic range are important figures of merit for detectors. In case of the AHCAL, the SNR is the ratio between the most probable

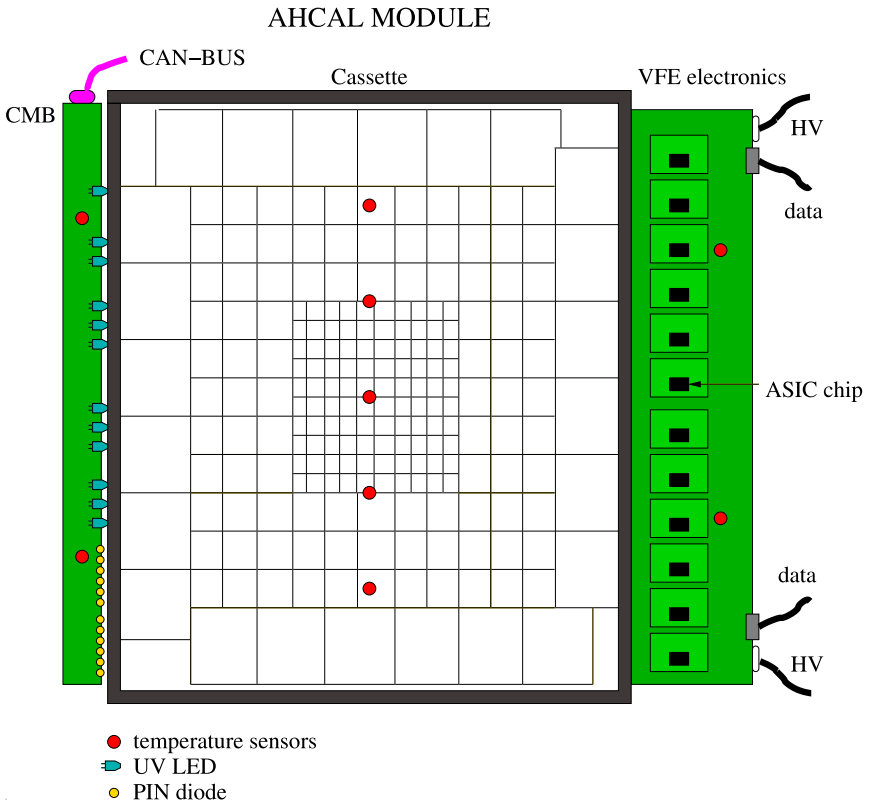

Figure 2.7: Module layout of the AHCAL physics prototype [31]. Center: steel cassette ($1 \times 1\,\mathrm{m}^2$), housing 216 (or 141) scintillator tiles. Left: CMB, containing 12 UV LEDs and 12 PIN diodes. Right: VFE board, comprising 12 ASIC chips and providing connections to both the external DAQ and the high voltage (HV) power supplies. Nine temperature sensors are distributed over each module.

muon signal above pedestal in a single cell and the pedestal width. The dynamic range is the difference between the largest and the smallest measurable signal. Increasing the SiPM bias voltage increases the signal from a given energy deposition and the pedestal width and reduces the dynamic range. The best SNR at an acceptable dynamic range is obtained at a light yield of 15 $\frac{\mathrm{pix}}{\mathrm{MIP}}$ [28]. The light yield LY_i of a cell i is defined as the number of pixels firing when a single muon passes through the cell, i.e.

$$LY_\mathrm{i}\left[\frac{\mathrm{pix}}{\mathrm{MIP}}\right] = \frac{A_\mathrm{i}^\mathrm{MIP}\,[\mathrm{ADC}]}{G_\mathrm{i}\,[\mathrm{ADC}] \cdot IC_\mathrm{i}}\,, \tag{2.4}$$

where IC_i is the electronics intercalibration factor, $A_\mathrm{i}^\mathrm{MIP}$ is the most probable cell response to muons, and G_i is the SiPM gain. The light yield depends on the tile size because the light collection efficiency varies with the tile dimensions and the length and the positioning of the WLS fiber [31]. Due to the voltage and temperature dependencies of A^MIP and G, the light yield depends on these parameters as well. The nominal operation voltage determined for each AHCAL SiPM during production is selected to yield a SiPM response of 15 pixels to LED light with an intensity corresponding to the light generated by 1 MIP in a scintillator tile.

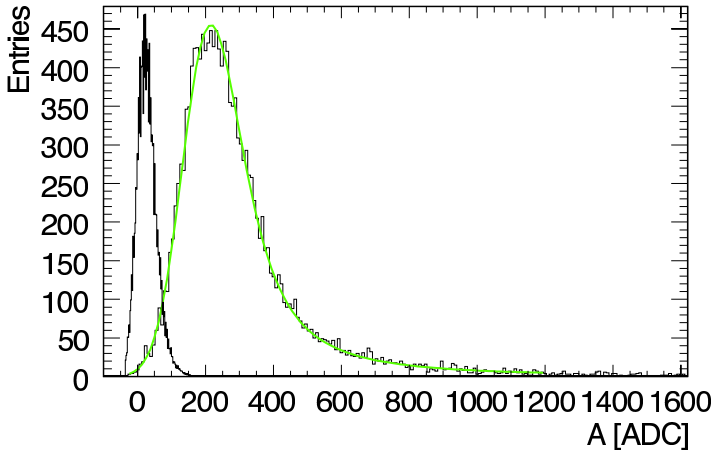

Figure 2.8: Pedestal of a single AHCAL cell (from random-trigger events, left histogram) and the response of the cell to passing muons (right histogram) [31]. Performing a fit of a Landau distribution convolved with a Gaussian function on the muon response and subtracting the mean pedestal from the most probable muon energy deposition yields the MIP calibration factor for this cell.

2.7 Calibration Scheme

The responses of all cells in the CALICE calorimeters with SiPM readout are equalized to a common physics signal using muons acting as minimum ionizing particles (MIPs). One MIP (as an energy unit) corresponds to the most probable energy deposited by a MIP. Figure 2.8 presents the response of a single AHCAL cell i to muons. A Landau distribution convolved with a Gaussian function is fitted to this histogram to extract the most probable value $A_{\mathrm{i}}^{\mathrm{MPV}}$ of the visible energy. The Landau distribution describes the energy deposition of MIPs in matter [44] and the Gaussian smearing accounts for the noise of the SiPM and the electronics. The difference between $A_{\mathrm{i}}^{\mathrm{MPV}}$ and the mean noise $A_{\mathrm{i}}^{\mathrm{ped}}$ of this cell gives the MIP calibration factor $A_{\mathrm{i}}^{\mathrm{MIP}}$. The parameter $A_{\mathrm{i}}^{\mathrm{MIP}}$ needs to be measured for each cell individually.

Several steps are necessary to translate signals measured in the CALICE calorimeters with SiPM readout (in ADC levels) to information about the deposited energy (in GeV). The response $A_{\mathrm{i}}\,[\mathrm{ADC}]$ of each cell i is corrected for effects of the non-linear SiPM response by multiplying A_{i} with a function $f_{\mathrm{i}}^{-1}(A_{\mathrm{i}}\,[\mathrm{pix}])$. This function is the inverse of the SiPM response function f_{i} deduced from test-bench measurements of the SiPM response curve. The relation

$$A_{\mathrm{i}}\,[\mathrm{pix}] = \frac{A_{\mathrm{i}}\,[\mathrm{ADC}]}{G_{\mathrm{i}}\,[\mathrm{ADC}] \cdot IC_{\mathrm{i}}} \tag{2.5}$$

converts A_{i} given in ADC levels to A_{i} in numbers of firing pixels, where IC_{i} is the electronics intercalibration factor of a given cell. Dividing the corrected signal by A_i^{MIP} yields the visible energy in MIP:

$$E_{\mathrm{i}}\,[\mathrm{MIP}] = \frac{A_{\mathrm{i}}\,[\mathrm{ADC}]}{A_{\mathrm{i}}^{\mathrm{MIP}}\,[\mathrm{ADC}]} \cdot f_{\mathrm{i}}^{-1}(A_{\mathrm{i}}\,[\mathrm{pix}])\ . \tag{2.6}$$

The deduction of the total deposited energy in GeV (taking into account the sampling

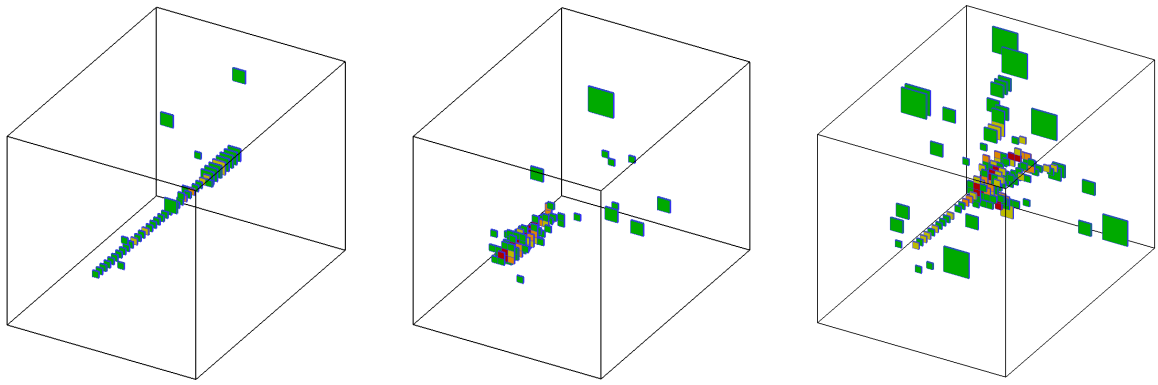

(a) (b) (c)

Figure 2.9: Illustrations of the measured energy depositions in the AHCAL physics prototype for (a) a 32 GeV negative muon, (b) a 10 GeV electron, and (c) a 10 GeV negative pion. Dark green cells correspond to visible energies between 0.5 MIP and 1.65 MIP, light green cells to visible energies between 1.65 MIP and 2.9 MIP, orange cells to visible energies between 2.9 MIP and 5.4 MIP, and red cells to visible energies above 5.4 MIP.

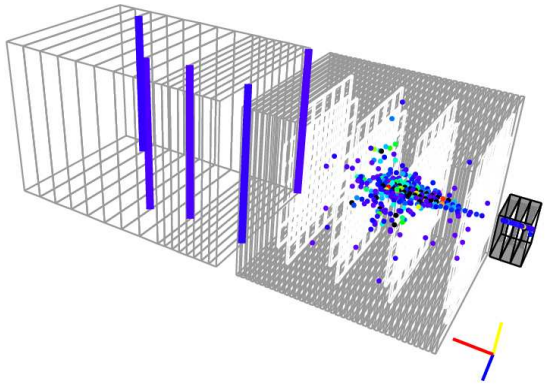

Figure 2.10: Online event display for a 30 GeV pion cascade measured with the Si-W ECAL, the AHCAL, and the TCMT (from right to left).

fraction, i.e. the ratio between visible and deposited energy) uses reference measurements of known energy (e.g. electrons from test-beam measurements).

In order to reduce the noise in the detector, a threshold of 0.5 MIP is applied for each cell, i.e. all signals below 0.5 MIP are rejected. The MIP detection efficiency is the integral of the muon response above threshold divided by the integral over the full range. The mean MIP detection efficiency of the AHCAL prototype cells is 94% [45]. More details about the calibration procedure and its application to the AHCAL physics prototype are given in [31].

2.8 Imaging Calorimetry

The imaging capability of the AHCAL is illustrated in Fig. 2.9. Figure 2.9(a) shows the typical detector response to a 32 GeV negative muon from test-beam measurements. The muon acts as a minimum ionizing particle, i.e. it leaves a straight ionization track in the

AHCAL and deposits small amounts of visible energy in each scintillator layer. The small energy depositions apart from the track are attributed to noise. Tracking algorithms can easily identify this type of events and locate the muon position.

Figure 2.9(b) presents the AHCAL response to a 10 GeV electron. The electromagnetic cascade starts in the first absorber layer and extends over less than half the detector in longitudinal direction. Since the dimension of the $3 \times 3\,\mathrm{cm}^2$ tiles corresponds approximately to one Molière radius in the AHCAL, most energy is deposited in a single tower of tiles with some energy deposited in adjacent tiles. As for muon events, the isolated hits apart from the cluster are attributed to noise. All electromagnetic cascades give the same characteristic image.

Figure 2.9(c) shows the visible energy deposited by a 10 GeV negative pion in the AHCAL. In the first part of the detector, the pion leaves an ionization track like a muon. The first inelastic pion scattering with a nucleus of the absorber material marks the end of the primary ionization track and the beginning of the hadronic cascade. The way the cascade evolves fluctuates strongly from one pion event to another. Signals in isolated cells are attributed both to noise and to energy depositions from neutral particles originating from the hadronic cascade. In general, the energy density of a pion cascade is much smaller and the spatial extension is much larger than for an electromagnetic cascade. The AHCAL granularity provides a detailed picture of the substructure of the pion cascade, e.g. secondary ionization tracks after the start of the cascade are visible.

Figure 2.10 presents the energy depositions from a 30 GeV pion measured with an integrated detector system comprising the Si-W ECAL, the AHCAL, and the TCMT. The pion leaves an ionization track in the Si-W ECAL before initiating a cascade in the AHCAL. Combined event display like this are available already during data collection and are a valuable tool for the online data quality assurance. Overlaying two or more measured cascades allows to evaluate the capability of Particle Flow algorithms to separate individual showers using data [46].

Chapter III

The CALICE Experiment at Fermilab

The CALICE collaboration successfully operated the physics prototypes of the AHCAL, the Si-W ECAL, the Sci-ECAL, and the TCMT (all described in Chapter 2) in an integrated setup with different configurations at the MTest beam line of the Fermilab Test-beam Facility (FTBF, formerly known as the Meson Test-beam Facility MTBF) in 2008 and 2009. The Si-W ECAL was installed together with the AHCAL and the TCMT in May and July 2008. The Sci-ECAL was commissioned in September 2008 and operated together with the AHCAL and the TCMT during this month and in May 2009. Both in July 2008 and in May 2009, the AHCAL and the TCMT recorded data without any ECAL being installed. The data collected at Fermilab complement test-beam measurements conducted with the AHCAL, the Si-W ECAL, and the TCMT at the H6 beam line of the CERN SPS accelerator in 2006 and 2007.

The test-beam data acquired at CERN (in 2006 and 2007) cover beam momenta from 6 GeV to 180 GeV and provide measurements of the detector response to electrons, positrons, muons, pions, and protons at different impact positions and angles. The analysis of these data provides a good understanding of the detector technologies employed and their performances [47, 33]. In addition, these data form the basis for detailed validations of hadron shower simulations [48, 49], the test of particle flow reconstruction algorithms [46], and the development of software compensation methods [27].

One of the main objectives achieved at Fermilab in 2008 and 2009 is the completion of the energy scans for electrons and pions down to 1 GeV. These data are necessary for studying the performance of the detectors in this energy range. In addition, low-energetic pions are particularly interesting for the validation of Geant4 simulations for hadrons. Another purpose of the measurements conducted at Fermilab is the collection of supplementary data at varying detector positions and angles for extending the corresponding studies. In addition, the stable operation of the detector prototypes for another two years yields information about the long-term performance of the devices. Finally, the test-beam program completed at Fermilab comprises the successful commissioning of the Sci-ECAL physics prototype and the operation of this detector in a combined setup with the AHCAL and the TCMT. Among the tasks accomplished in the context of this thesis are contributions to the AHCAL commissioning at Fermilab, the operation and maintenance of the detector during data acquisition, and the on-scene coordination of the whole experiment.

This chapter describes the MTest beam line at the FTBF (Section 3.1), the beam line instrumentation, and the setup of the CALICE detectors (Section 3.2). In addition,

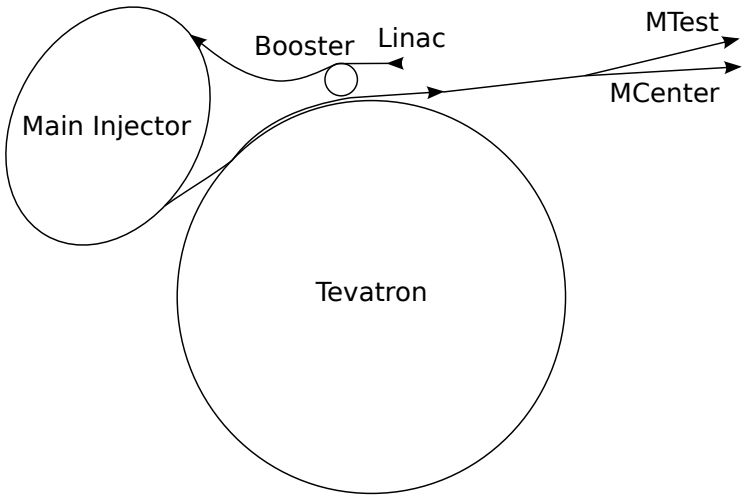

Figure 3.1: The beam delivery chain to the FTBF beam lines. The Linac accelerates negative hydrogen ions. After stripping off the electrons from the ions, the remaining protons are accelerated by the booster and the main injector to 120 GeV before they are delivered to MTest, MCenter, or the Tevatron.

Section 3.3 presents the operation of the Čerenkov detector provided by the FTBF for separating particles of different types in the beam. Section 3.4 discusses some aspects of the AHCAL commissioning and the stability of the detector operation.

3.1 The Fermilab Test-beam Facility

The FTBF is located at the Fermi National Accelerator Laboratory in Illinois, USA, and provides the infrastructure for exposing detectors to particle beams (electrons, muons, and charged hadrons) between 0.5 GeV and 120 GeV [50, 51]. The facility consists of two separate beam lines, MTest and MCenter, and several areas for setting up experiments. The CALICE detector prototypes and auxiliary instrumentation were installed in sector MT6-2B of the MTest beam line (see Section 3.2).

The primary beam for both the MTest and the MCenter beam lines consists of 120 GeV protons. The protons originate from a source of negative hydrogen ions (H^-). The ions are extracted at an energy of 750 keV. Afterwards, a linear accelerator (Linac, [52]) increases their energy to 400 MeV and transfers them to a booster [53]. The booster is a small synchrotron. The electrons are stripped off the hydrogen ions and the energy of the remaining protons is raised to 8 GeV. The protons are fed into a larger synchrotron, the so-called main injector. The main injector continues the proton acceleration and provides 120 GeV protons to the FTBF beam lines and other experiments. Figure 3.1 illustrates the way the protons travel from the source to the MTest beam line.

The MTest beam line offers different operation modes for various purposes. In proton mode, the primary beam is guided through a collimator and forwarded to the experimental areas. For the pion mode, the primary beam is directed to a target (MT1-TGT, 435 m upstream of MT6, 25 cm of aluminum) to generate a beam of secondary particles. In addition to protons, the secondary beam mainly contains pions, electrons, and muons. In pion mode, the MTest beam line can provide secondary particles between 8 GeV and

66 GeV. The low-energy pion mode uses a different target (MT4-TGT, 145 m upstream of MT6, 30 cm of aluminum) and delivers secondary beam momenta from 1 GeV to 32 GeV. In any of these modes, closing the beam dumps (MT6AB1 and MT6AB2, each 1.5 m of steel) upstream of the MT6-2 area stops all particles but muons and generates a high flux of pure muons on an area of 1 square meter in MT6-2. This muon mode is needed for the calibration of the CALICE detector prototypes (see Section 2.7). The momentum spread of the MTest beam is about 1-3% (depending on the particle type, the beam momentum, and collimator settings, [54]). The standard deviation of the beam spot is 7 mm for the primary proton beam and 2-5 cm for secondary beams at lower momenta [50].

A differential Čerenkov counter is installed at the upstream end of the MT6 area. The device consists of an 18.5 m long pressure tank with 100 μm titanium windows (0.003 X_0 each) at the beam entrance and exit points. A glass mirror is located inside the tank. At the nominal beam position, the thickness of the mirror is 2.5 mm (0.023 X_0). The working principle of this Čerenkov counter is described in Section 3.3. A second Čerenkov detector is attached to the upstream end of the first one and adds three titanium windows (100 μm and 0.003 X_0 each) and a 4 mm plastic mirror (0.009 X_0) to the material in the beam line. During the CALICE measurements, the upstream Čerenkov counter is not used and is kept evacuated. Thus, the vacuum of the MTest beam pipes extends to the beginning of the downstream Čerenkov counter. The distance between this point and the last momentum selecting dipole magnet (MT5E) is about 30 m.

The FTBF provides various instrumentation for monitoring the beam intensity, position, and width. Downstream the differential Čerenkov counter, there are a scintillator (MT6SC1, 4 mm of plastic, 0.009 X_0) and a proportional wire chamber (WT6WC1, 0.007 X_0 [55]). More wire chambers and scintillators are available, but are removed for the CALICE measurements to reduce the amount of material in the beam line.

Beam tubes installed during part of the measurements reduce the multiple scattering of electrons and low-energetic pions on the way from the differential Čerenkov counter to the CALICE detectors. Mylar windows (25 μm, 0.0001 X_0) seal the ends of the tubes, which are filled with Helium at atmospheric pressure. In the CALICE setup, there are six beam tubes covering a total length of 20 m. With the beam tubes installed, the material between the last momentum selecting magnet (MT5E, about 30 m upstream of the downstream Čerenkov counter) and the beginning of the CALICE setup (Section 3.2) adds up to $0.08 - 0.16\,X_0$, depending on the Čerenkov pressure.

Figure 3.2 presents an estimate of the MTest secondary beam composition (in low-energy pion mode) measured by CALICE using data from the Sci-W ECAL, the AHCAL, and the TCMT with preliminary detector calibrations during data acquisition [56, 51]. The different event categories are muons (low energy deposition in all three calorimeters), electrons (large visible energy in the Sci-W ECAL, only noise in the AHCAL), two-particle events (visible energy higher than expected for given beam momentum), and pions (all other events). The measurement illustrates the momentum dependence of the secondary beam composition and emphasizes the challenge of collecting pion data at low beam momenta. Charged pions have a limited lifetime (mean decay length $c\tau = 7.8$ m, rest mass $m = 140$ MeV) and can decay into muons on the way from the target to the CALICE detectors (the distance d between the low-energy target MT4-TGT and the CALICE calorimeters is about 175 m). The surviving fraction f_π of pions with energy E after a distance d is given

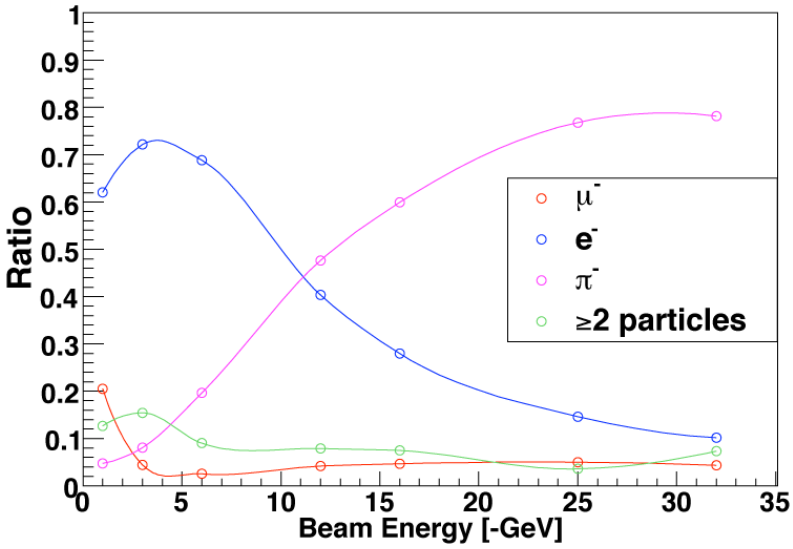

Figure 3.2: MTest secondary beam composition (in low-energy pion mode) measured with the CALICE detectors [51, 56].

by

$$f_\pi = \exp\left(-\frac{m}{E}\cdot\frac{d}{c\,\tau}\right) . \tag{3.1}$$

According to this equation, about 5% of the pions generated in MT4-TGT is expected to reach the CALICE detectors at 1 GeV. This number agrees with the measured pion fraction in Fig. 3.2. For low beam momenta, the electron fraction increases significantly. In addition, an increased fraction of two-particle events is observed at lower beam momenta.

3.2 Experimental Setup

Figure 3.3 illustrates the arrangement of the CALICE detector prototypes and auxiliary beam line instrumentation installed in the MT6-2 area of the MTest beam line at the FTBF. The AHCAL prototype resides on a movable stage. This stage allows for moving the detector in x- and y-direction, i.e. orthogonal to the beam axis, and to rotate and stagger the calorimeter layers by up to 30 degrees in the x-z-plane. The TCMT is located behind the AHCAL. While operated, the Si-W ECAL and the Sci-ECAL are placed on the movable stage in front of the AHCAL. Figure 3.4 depicts the integrated setup with the Si-W ECAL, the AHCAL, and the TCMT.

A set of plastic scintillators with PMT readout provides information for triggering the DAQ and about the beam quality. The main DAQ trigger is the coincidence between the signals from two $10 \times 10\,\mathrm{cm}^2$ scintillators (8 mm thick, $0.019\,\mathrm{X}_0$) placed 2.5 m apart from each other. For collecting muon data, the coincidence between the signals from two $1 \times 1\,\mathrm{m}^2$ scintillators is used instead. The upstream $1 \times 1\,\mathrm{m}^2$ scintillator is only installed during muon measurements. The downstream $1 \times 1\,\mathrm{m}^2$ scintillator allows to veto muon events in all data sets. The analog signal from a $20 \times 20\,\mathrm{cm}^2$ scintillator (termed multiplicity counter, 16 mm thick, $0.039\,\mathrm{X}_0$) is used to identify events with two or more particles passing the scintillator simultaneously. In addition, the $20 \times 20\,\mathrm{cm}^2$ scintillator provides an alternate

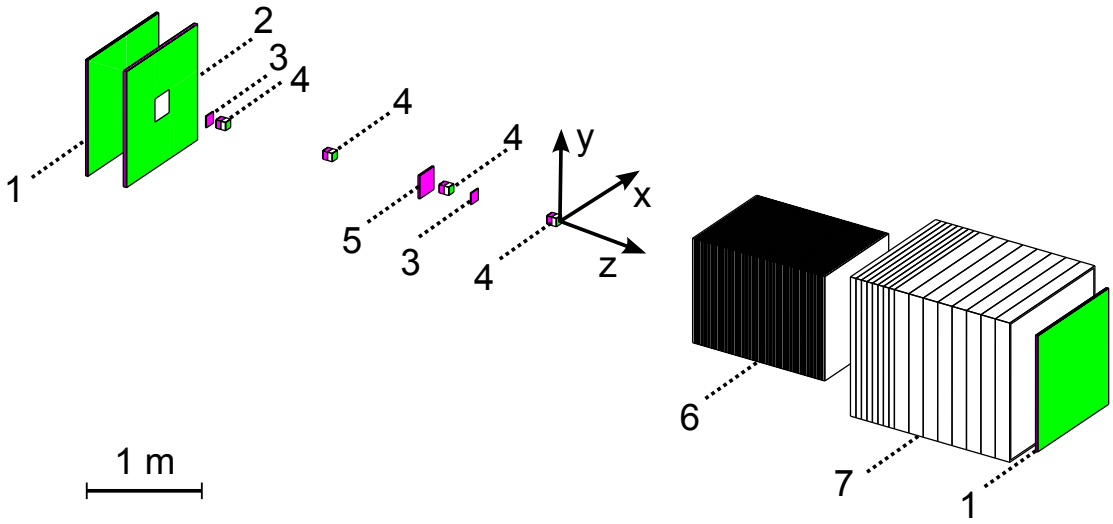

Figure 3.3: The experimental setup at MTest: (1) $1 \times 1\,\mathrm{m}^2$ scintillators, (2) $1 \times 1\,\mathrm{m}^2$ veto wall, (3) $10 \times 10\,\mathrm{cm}^2$ scintillators, (4) drift chambers, (5) $20 \times 20\,\mathrm{cm}^2$ multiplicity counter, (6) AHCAL, and (7) TCMT. While operated, the Si-W ECAL and the Sci-ECAL are located upstream of the AHCAL. The upstream $1 \times 1\,\mathrm{m}^2$ scintillator is only installed during muon measurements. The z-axis indicates the beam position and direction. This figure is a visualization of the test-beam geometry implemented in the Mokka simulation explained in Section 5.2.

main trigger signal for the DAQ. A veto wall detects additional particles in the beam halo and particles that initiate a shower before reaching the AHCAL. The veto wall is a $1 \times 1\,\mathrm{m}^2$ scintillator plane with a $20 \times 20\,\mathrm{cm}^2$ hole in its center. The plane is pieced together from four scintillator planes measuring $60 \times 40\,\mathrm{cm}^2$ each. Each plane is connected to a separate PMT.

Four drift chambers ($0.001\,X_0$) operated with a gas mixture of 50% argon and 50% ethane measure the position of the beam particles [57]. The center of the backplane of the most downstream drift chamber defines the origin of the global CALICE coordinate system. The distance between the downstream end of the downstream MTest Čerenkov detector (Section 3.3) and the most downstream CALICE drift chamber is 29 m. The material between the veto wall and the calorimeter prototypes adds up to roughly $0.09\,X_0$.

All CALICE detectors and beam line instrumentation are centered on the nominal beam axis. Table I gives the order of the drift chambers (1 = upstream, 4 = downstream) and alignment of the centers of the drift chambers with respect to the nominal beam axis (measured by the Fermilab alignment group). In the CALICE coordinate system shown in Fig. 3.3, the horizontal offsets correspond to shifts of the drift chambers in x-direction and the vertical offsets correspond to shifts in y-direction. The second value for DC3 is the alignment of this drift chamber after the temporary removal for repairs and re-alignment in 2009.

3.3 The Differential Čerenkov Detector at the FTBF

The secondary beams provided at the FTBF comprise charged particles of various types. Most particles are electrons, pions, or muons for negatively charged beams and positrons,

Figure 3.4: Picture of the integrated detector setup with the Si-W ECAL (front), the AHCAL (center), and the TCMT (back). The Si-W ECAL and the AHCAL reside on the movable stage. Part of the DAQ commonly used by all three calorimeters is visible on the right.

TABLE I
ORDER AND ALIGNMENT OF THE CALICE DRIFT CHAMBERS.

drift chamber	DC1	DC2	DC3	DC3 (2009)	DC4
position	2	1	3	3	4
horizontal offset [mm]	1.1	1.3	1.4	0.3	1.0
vertical offset [mm]	-0.1	-0.1	0.0	0.0	-0.1

pions, muons, or protons for positively charged beams [51]. A differential Čerenkov detector is part of the MTest beam line instrumentation and allows the identification of particles based on their masses. Using the signal from the Čerenkov detector in the on-line trigger decision enhances the electron, pion, or proton content in the recorded data.

Charged particles with momentum p emit Čerenkov light when passing through a medium of refractive index n if their mass m lies below the threshold mass m_{thr} (see Section 1.1.4 and Reference [58]). This threshold is given by

$$m_{\text{thr}} = \frac{p}{c} \cdot \sqrt{n^2 - 1}\,, \tag{3.2}$$

where c is the speed of light in vacuum. The opening angle θ_{cone} of the Čerenkov light cone is proportional to $\Delta m = (m_{\text{thr}} - m)$. Figures 3.5(a) and 3.5(b) sketch the layout and show a picture of the differential Čerenkov counter used at MTest. The Čerenkov light is generated in an 18.5 m long pressure tank filled with nitrogen (alternatively, helium can be used). The gas pressure is adjustable up to 1.36 atm. A glass mirror inside the tank focuses the Čerenkov light on a second mirror, which has a hole in its center. For narrow Čerenkov cones, the light shines through the hole on the inner PMT. If the light cone is wider than the hole, the light is reflected further to the outer PMT. The refractive index of gas is proportional to the gas pressure. Therefore, adjusting the gas pressure changes both m_{thr} and θ_{cone}. In addition, the Čerenkov light intensity (and thus the detection efficiency with the PMTs) increases with the gas pressure.

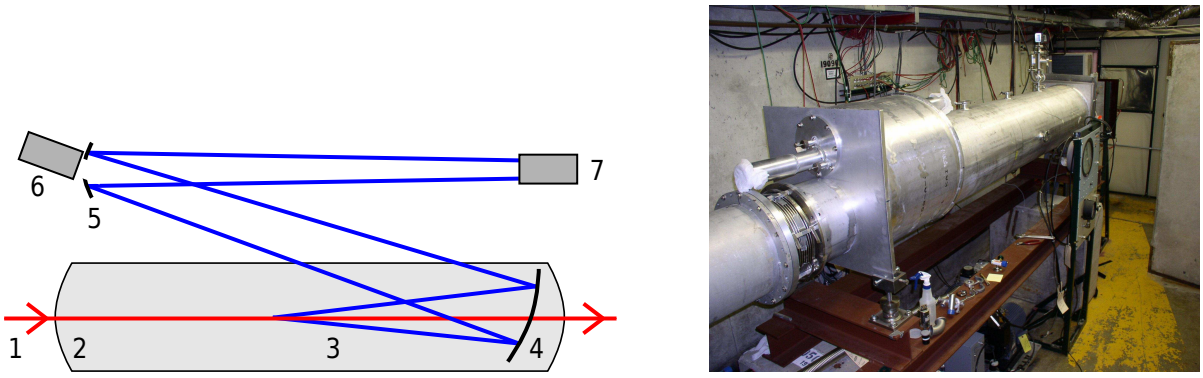

(a) (b)

Figure 3.5: (a) The differential Čerenkov counter at MTest: (1) incoming particle, (2) pressure tank with gas, (3) Čerenkov light, (4) mirror, (5) mirror with hole, (6) inner PMT, (7) outer PMT. (b) Picture of the differential Čerenkov counter at MTest (looking downstream).

Both the light detection efficiency and the noise rate of the inner and the outer Čerenkov PMTs increase with the operation voltage. Figure 3.6(a) presents the fraction of charged particles detected by the downstream scintillator and generating a signal in the inner (filled circles) or outer (open circles) PMT for varying PMT operation voltages. The beam momentum is 32 GeV and the Čerenkov gas pressure is 0.12 atm. A voltage at the beginning of the plateau (at 1800 V) is chosen to operate both PMTs.

Figure 3.6(b) shows the fraction of negatively charged particles traversing the Čerenkov detector and generating a signal in the inner or the outer PMT at different gas pressures. The gas tank is filled with Nitrogen and the beam momentum is 10 GeV. A scintillator placed downstream of the pressure tank counts the total number of passing particles. At pressures between 0.14 atm and 0.34 atm, the outer PMT detects light from electrons (45% of the beam particles), while no signal is detected by the inner PMT. Between 0.34 atm and 0.41 atm, the threshold m_{thr} rises above the pion and muon masses and the inner PMT starts to detect Čerenkov light from these particles. Due to their low mass difference, 10 GeV muons and pions cannot be separated by this Čerenkov detector. At higher pressures, the difference between m_{thr} and the pion and muon masses increases. The Čerenkov cones of these particles become wider and the light moves from the inner to the outer PMT. Within the pressure limit of the gas tank, 10 GeV kaons (or protons) cannot generate Čerenkov light.

The threshold pressure P_{T}^{π} at which the inner PMT starts to detect Čerenkov light from pions (and muons) is extracted from pressure scans recorded for different beam momenta. Figure 3.7(a) summarizes the results for beam momenta between 6 GeV and 30 GeV (the measurement errors are smaller than the marker sizes). The theoretical prediction for the threshold pressure P_{T} of a particle with mass m is given by

$$P_{\mathrm{T}} = 1\,\mathrm{atm} \cdot \left(\frac{\frac{1}{\sqrt{1-\frac{m^2}{E^2}}} - 1}{\delta} \right) + O\ , \tag{3.3}$$

where $\delta = n_{1\mathrm{atm}} - 1 = 0.000297$ (nitrogen) [59]. The offset O takes into account a systematic gauge uncertainty of the pressure sensor. The solid line in Fig. 3.7(a) shows the prediction

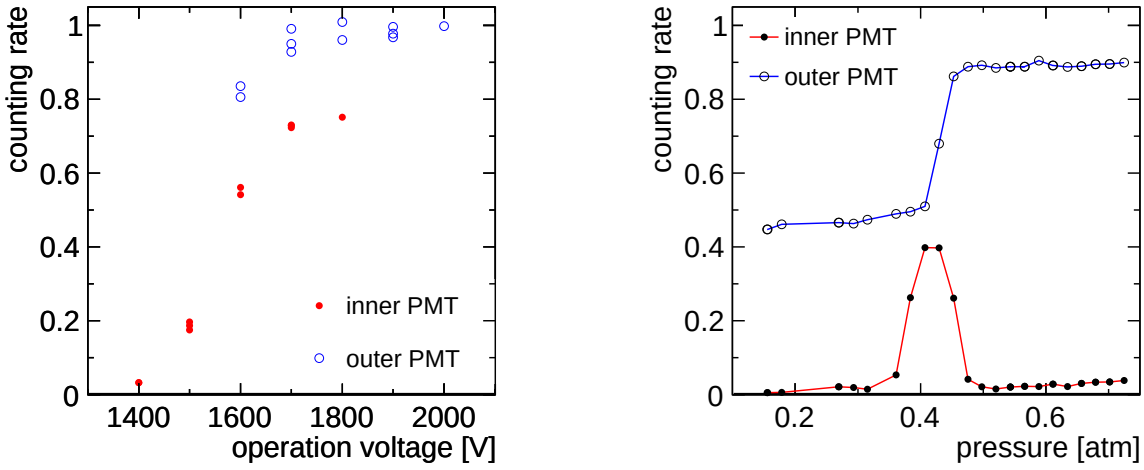

(a) (b)

Figure 3.6: (a) Fraction of charged particles detected by the downstream scintillator and generating a signal in the inner (filled circles) or outer (open circles) PMT as a function of the PMT operating voltages. (b) Čerenkov pressure scan using nitrogen and negatively charged particles at 10 GeV beam momentum. See text for a more detailed description.

of Eq. (3.3) after fitting the function to the pion measurements. The offset O is determined as 0.05 atm.

Integrating the Čerenkov detector signal in the on-line trigger decision enhances the pion, electron, or proton content in the recorded data (the integration procedure is described in [30]). Pions are measured both with negative and positive beams, electrons with negative beams, and protons with positive beams. From 8 GeV to 30 GeV, pions are identified by setting the Čerenkov pressure to the pion threshold P_{T}^{π} and requiring a signal in the inner PMT. At the pion threshold, the Čerenkov light generated by electrons is detected in the outer PMT. For pion momenta below 6 GeV, the threshold pressure exceeds the 1.36 atm pressure limit of the Čerenkov gas tank (Eq. (3.3) yields $P_{\mathrm{T}}^{\pi} = 1.37$ atm for 5 GeV pions, $P_{\mathrm{T}}^{\pi} = 2.12$ atm for 4 GeV pions, and $P_{\mathrm{T}}^{\pi} = 33.6$ atm for 1 GeV pions). Thus, the strategy for enhancing the pion content of the recorded data between 1 GeV and 4 GeV is to reject all events with particles that generate a signal in the Čerenkov detector, i.e. all electrons (or positrons). This approach does not allow to tag kaon or (anti-) proton events, but the contribution from these particles to the beam at low momenta is small and cannot be observed. To maximize the Čerenkov detection efficiency, the Čerenkov pressure is set to the maximum of 1.36 atm for measuring pions between 2 GeV and 4 GeV. Because of a very low data acquisition rate for pions at 1 GeV, the threshold is lowered to 0.14 atm to minimize the effects of multiple scattering at this beam momentum. Testing both pion selection strategies at 6 GeV yields a 20% higher data acquisition rate for the second approach (rejecting electrons, Čerenkov pressure at 0.68 atm because 1.36 atm is above P_{T}^{π} for 6 GeV pions) than for the first approach (tagging pions, Čerenkov pressure at P_{T}^{π}) at a comparable pion purity. At higher beam momenta, the proton content in the beam increases and the first selection strategy has to be applied.

Figure 3.7(b) presents the operation pressures applied for enhancing the fraction of

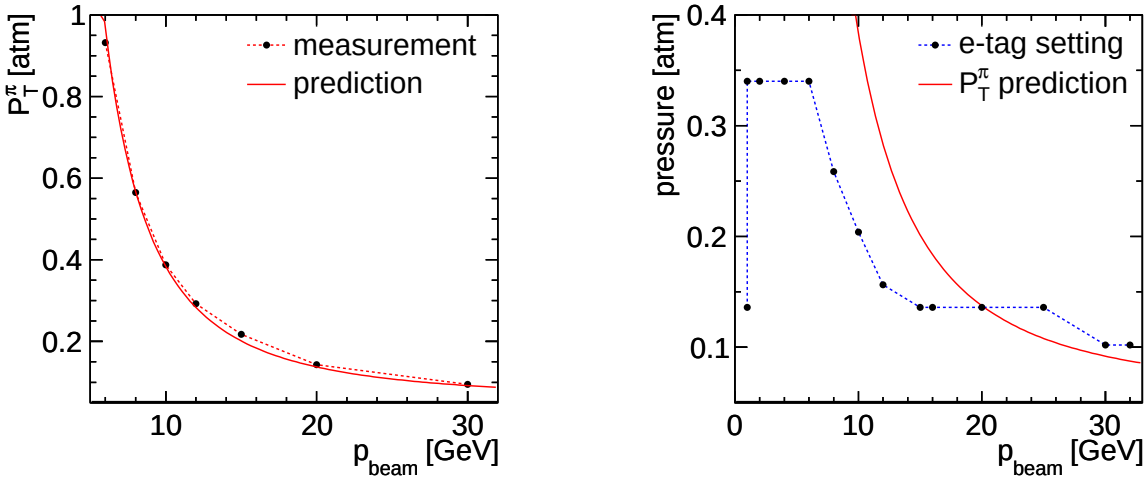

(a) (b)

Figure 3.7: (a) Measured threshold pressures P_T^π for pions at different beam momenta and the result of performing a fit of Eq. (3.3) to these values. (b) Čerenkov detector operating pressure for enhancing the electron content in the recorded data at different beam momenta. The solid line indicates the pion threshold pressure.

electron events in the collected data (negatively charged beam) between 1 GeV and 30 GeV beam momentum. The red line is the theory prediction for the pion threshold from Eq. (3.3) (taking into account the measurement offset $O = 0.05$ atm). Only events with a signal in the Čerenkov detector are recorded. Two pressure settings tested at 1 GeV (0.34 atm and 0.14 atm) yield comparable data acquisition rates, while the lower pressure reduces the amount of material in the beam line.

Protons are selected by setting the gas pressure to 1.36 atm and requiring no signal in the inner and the outer Čerenkov PMTs (positive beam). This selection suppresses positron, pion, and muon events for beam momenta down to 6 GeV. Due to this limitation and the low proton content of the beam at low momenta, proton data are only collected for 10 GeV and above. The selection approach excludes kaons above 18 GeV (Eq. (3.3) yields a threshold pressure of 1.31 atm for 18 GeV kaons).

Figures 3.8(a) and 3.8(b) illustrate the gain of using the Čerenkov signal in the online trigger decision. The black histogram in Fig. 3.8(a) shows the visible energy in the AHCAL for measurements using only the $10 \times 10\,\text{cm}^2$ scintillator coincidence as trigger and a positive beam at 10 GeV. The Čerenkov pressure is at 1.36 atm. The red histogram presents the proton content selected offline using the Čerenkov information. The proton content in the recorded data is below 10%. The green histogram shows the positron events (right peak) and pion events (left shoulder on the positron peak) from the same set of data. The positron content is roughly 55%, the pion content 40%. The small peak at low energies (red and green histograms) are muons (about 5%). The numbers confirm the measurements from [56] presented in Fig. 3.2. Figure 3.8(b) shows the visible energy for three different sets of measurements at 10 GeV using the Čerenkov signal to enhance the electron (blue), the pion (green), or the proton (red) content in the recorded data. The pion and proton data show a remaining muon contamination of less than 6%. For the

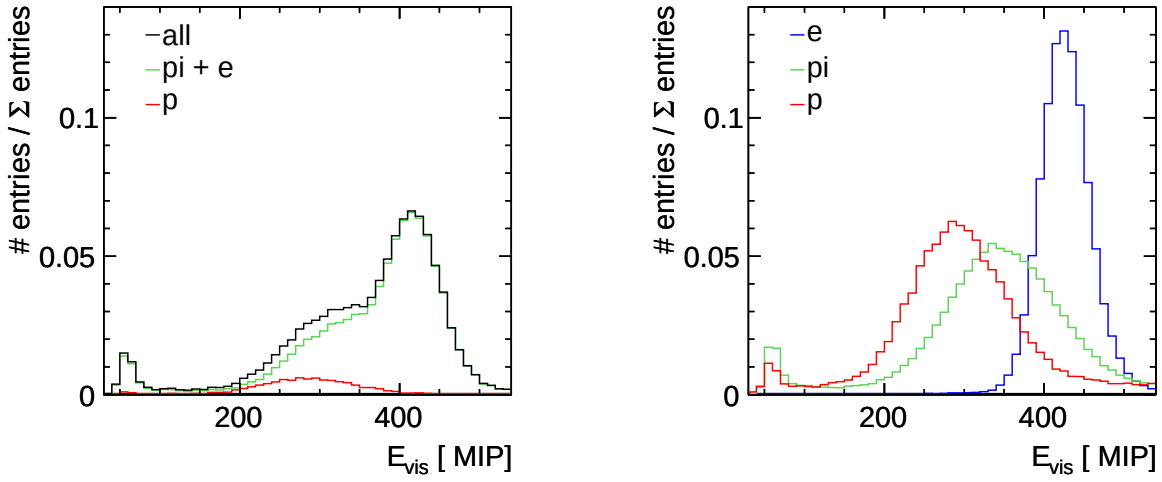

(a) (b)

Figure 3.8: (a) Visible energy in the AHCAL for all beam events at 10 GeV (one measurement, black). Using the Čerenkov information in offline analysis allows to separate the proton content (red) from pions and positrons (green). The small peak at low energies is attributed to a contamination with muons. (b) Visible energy in the AHCAL for data collected with the Čerenkov signal included in the online trigger decision to enhance the particle content of a certain type in the recorded data (three measurements, electron data in blue, pion data in green, and proton data in red). The purity of the data samples is discussed in Chapter 6.

electron data, no contamination is visible in this figure.

3.4 AHCAL Commissioning and Operation

Thanks to a smooth installation and stable running of all CALICE detectors installed at Fermilab in 2008 and 2009, all data required to achieve the goals of the program like extending the calorimeter performance studies and the validation of GEANT4 simulations for hadron cascades to lower beam momenta (down to 1 GeV) have been recorded. In total, more than 40 million events are available for analysis. This section discusses the optimization of the AHCAL working point during the commissioning phase in May 2008 and some aspects of the AHCAL performance and calibration during the operation at Fermilab.

Working Point Optimization

The light yield is a figure of merit for finding the optimum operation voltage for the AHCAL SiPMs. Cells (scintillator tile and SiPM) with a light yield of 15 $\frac{\text{pix}}{\text{MIP}}$ show the best signal to noise ratio at an acceptable dynamic range [28]. Tuning the operation voltages of the AHCAL SiPMs changes the light yield. A procedure for determining the voltage adjustments needed to shift the light yield to a target value is described in [37]. Applying this procedure during the commissioning at Fermilab shifts the mean light yield of all AHCAL cells to 14 $\frac{\text{pix}}{\text{MIP}}$. The target value lies below the optimum of 15 $\frac{\text{pix}}{\text{MIP}}$ to avoid stressing the

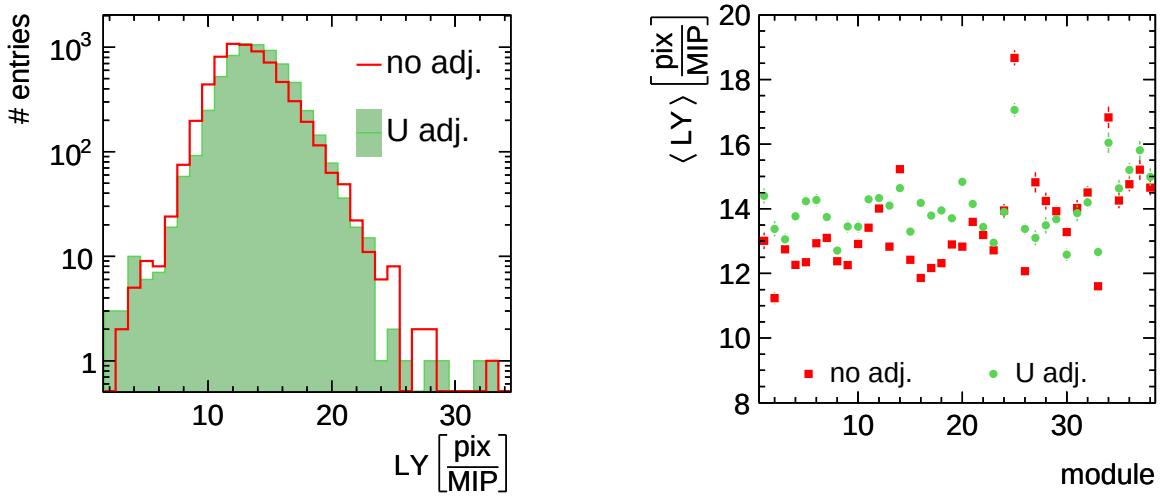

(a) (b)

Figure 3.9: (a) Light yield of all AHCAL cells and (b) mean light yield for all AHCAL modules before (no adj.) and after (U adj.) adjusting the bias voltages for each module to shift the mean light yield to 14 $\frac{\text{pix}}{\text{MIP}}$.

SiPMs with too high bias voltages. To keep the procedure simple, common shifts are applied to each layer. Therefore, the adjustment procedure only shifts the mean light yield of each layer to the target value, but does not reduce the spread of the light yield between the cells within one layer. Figure 3.9(a) compares the mean light yield of all AHCAL cells obtained before optimizing the SiPM bias voltages (mean 13 $\frac{\text{pix}}{\text{MIP}}$, average detector temperature 27 °C) and values measured after applying the voltage adjustment procedure (mean 14 $\frac{\text{pix}}{\text{MIP}}$, average detector temperature 25.3 °C). Figure 3.9(b) compares the mean light yields for the individual AHCAL modules from these measurements. The adjustment procedure successfully shifts the mean of all modules towards the target value and reduces the spread between the modules. Establishing the procedures for optimizing the light yield (and therefore the detector performance) are important results for future test-beam measurements as well as for operating a calorimeter using the AHCAL technology in a detector at a collider experiment.

Pedestal Stability

Figure 3.10 presents the mean pedestal width (standard deviation) of all AHCAL cells (from random trigger events without threshold cut) for several measurements performed throughout July 2008, September 2008, and May 2009 at fixed SiPM bias voltages. The mean pedestal width is stable within one ADC level (indicated by the green band). The stability of the pedestal width indicates the long-term stability of the detector performance.

Monitoring the SiPM Gain

The SiPM gains and electronics intercalibration factors for each cell are measured daily during data collection periods (the respective measurements are explained in Chapter 2).

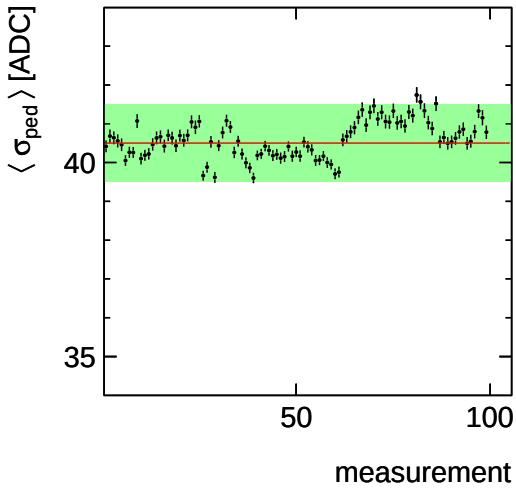

Figure 3.10: Mean pedestal width $\langle\sigma_{\text{ped}}\rangle$ (from random trigger events) of all AHCAL channels for several measurements performed throughout the data collection periods in July 2008, September 2008, and May 2009 at fixed SiPM bias voltages.

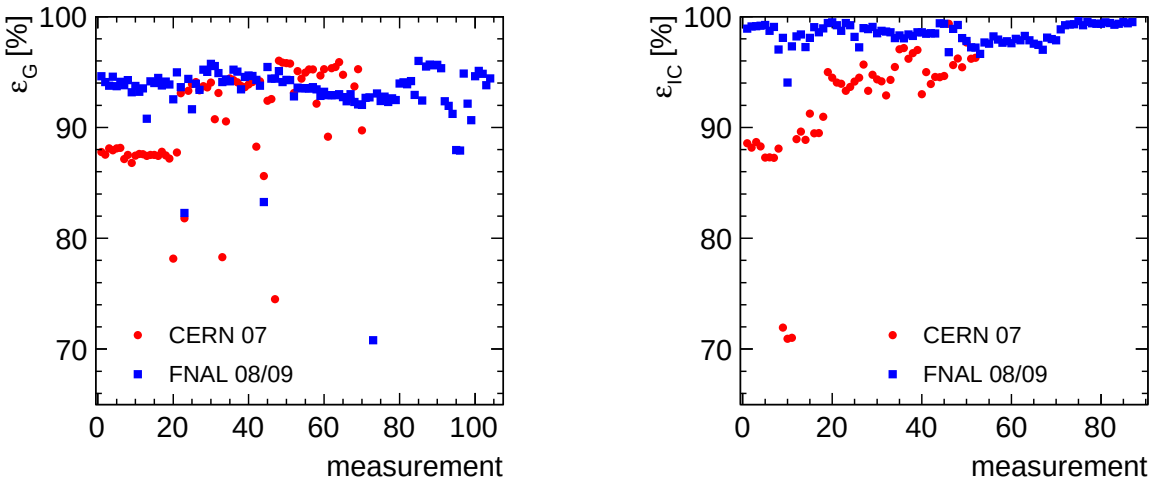

(a) (b)

Figure 3.11: Calibration efficiency ε of single measurements for (a) the SiPM gains G and (b) the electronics intercalibration factors IC.

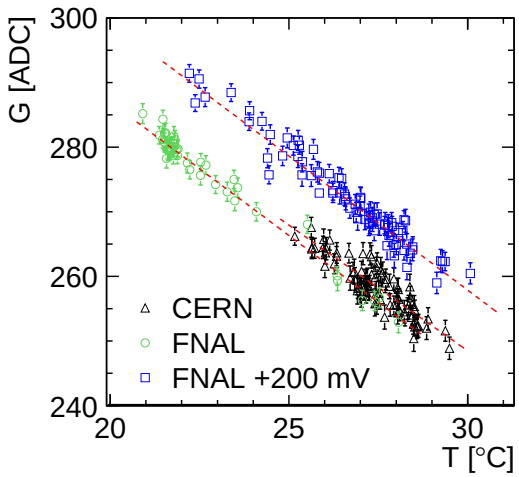

Figure 3.12: SiPM gain G for a single AHCAL cell measured at different temperatures T at CERN (triangles) and Fermilab (circles) at the same operation voltages and at Fermilab at 200 mV higher bias voltages (squares). The dashed lines indicate the results of linear fits performed on the three data sets.

Figures 3.11(a) and 3.11(b) present the efficiency of these measurements performed at CERN in 2007 (red) and at Fermilab in 2008 and 2009 (blue). The calibration efficiency is the ratio between the number of successfully calibrated channels and the total number of AHCAL channels (about 2% dead cells are accounted for [31]). In addition, for the CERN efficiencies, 916 SiPMs without LED light are not taken into account. The efficiency of the early CERN measurements of the SiPM gain and the electronics intercalibration is below 90% and jumps to 95% after fixing several CMBs. Throughout all data collection periods at Fermilab, the efficiencies for the gain measurements are at 95% and the efficiencies for the electronics intercalibration measurements are at 99%. Both the measurement histories for CERN and for Fermilab show individual bad measurements with low efficiency. The results are averaged for calibrating the data. Therefore, single bad measurements do not affect the overall calbration efficiency. The default values used for calibrating cells without measurement results are 300 ADC levels ($6.8 \cdot 10^5$ electrons) per photon for the SiPM gain and 10 for the electronics intercalibration factor.

Figure 3.12 shows gain measurements for a single AHCAL SiPM at different temperatures. The triangles correspond to measurements performed at CERN and the circles correspond to measurements performed at Fermilab at the same SiPM bias voltage. The gains obtained with both setups agree. The squares represent Fermilab measurements done after a voltage increase of 200 mV. As expected, the gain for a fixed temperature increases by roughly 2%. The dashed lines present linear fits to the three measurement sets. The slopes agree within their uncertainties (CERN: $(-3.9 \pm 0.2)\,\frac{\mathrm{ADC}}{\mathrm{K}}$, FNAL: $(-4.1 \pm 0.1)\,\frac{\mathrm{ADC}}{\mathrm{K}}$, FNAL +200 mV: $(-4.1 \pm 0.1)\,\frac{\mathrm{ADC}}{\mathrm{K}}$). The offsets obtained from the linear fit for the CERN set and FNAL set at the same operation voltage agree within uncertainties as well ((365 ± 5) ADC and (370 ± 3) ADC). The other AHCAL cells show comparable agreements between the different setups and voltage settings.

The analysis presented this thesis uses data collected at fixed SiPM bias voltages. The mean temperature of the gain measurements used to calibrate these data is 26.5 °C. An

average temperature dependence of the gain of $-1.6\,\frac{\%}{\mathrm{K}}$ is used. The mean gain-temperature dependence of $-1.6\,\frac{\%}{\mathrm{K}}$ corresponds to the factor obtained for previous calibration sets obtained at different voltage and temperature settings ($-1.7\,\frac{\%}{\mathrm{K}}$ [37]) after scaling this factor by the mean ratio between the gains measured under the respective operation conditions, i.e. after taking into account the different references for the relative slopes.

The open histogram in Fig. 3.13(a) shows the difference between the gain calibration factors obtained from measurements at Fermilab (native calibration, set A) and previous gain measurements from CERN (non-native calibration, set B) without correcting for the effects of different measurement temperatures and SiPM bias voltages. The three peak structure is due to different bias voltage adjustments applied for different groups of SiPMs. The filled histogram shows the difference after correcting for the effects of voltage and temperature differences [37]. The corrections reduce the mean difference from -6% to below 1% and the spread from 7% to 5%. Figure 3.13(b) presents the 98% correlation between native and non-native gain calibration factors after correcting for voltage and temperature differences.

The difference between the electronics intercalibration factors obtained from measurements at native (set A) and non-native (set B) operating conditions is presented in Fig. 3.13(c). The electronics intercalibration factors do not depend on operation voltage or temperature. The mean difference is below 1% and the spread is below 3%. This illustrates the high stability of the electronics intercalibration measurement. Figure 3.13(d) presents the 94% correlation between the two independent extractions of the electronics intercalibration factors.

Between the extraction of the two sets of SiPM gain and electronics intercalibration factors, about 10% of the front-end electronics cards were replaced (because of transport damages). The parameters of the cards have a spread of 5% between individual devices, which contributes to the spread observed in the previous comparisons. The good agreement of the SiPM gain and electronics intercalibration measurements conducted under different operation conditions and after several years of detector operation illustrate the stability of the calibration system of the AHCAL physics prototype.

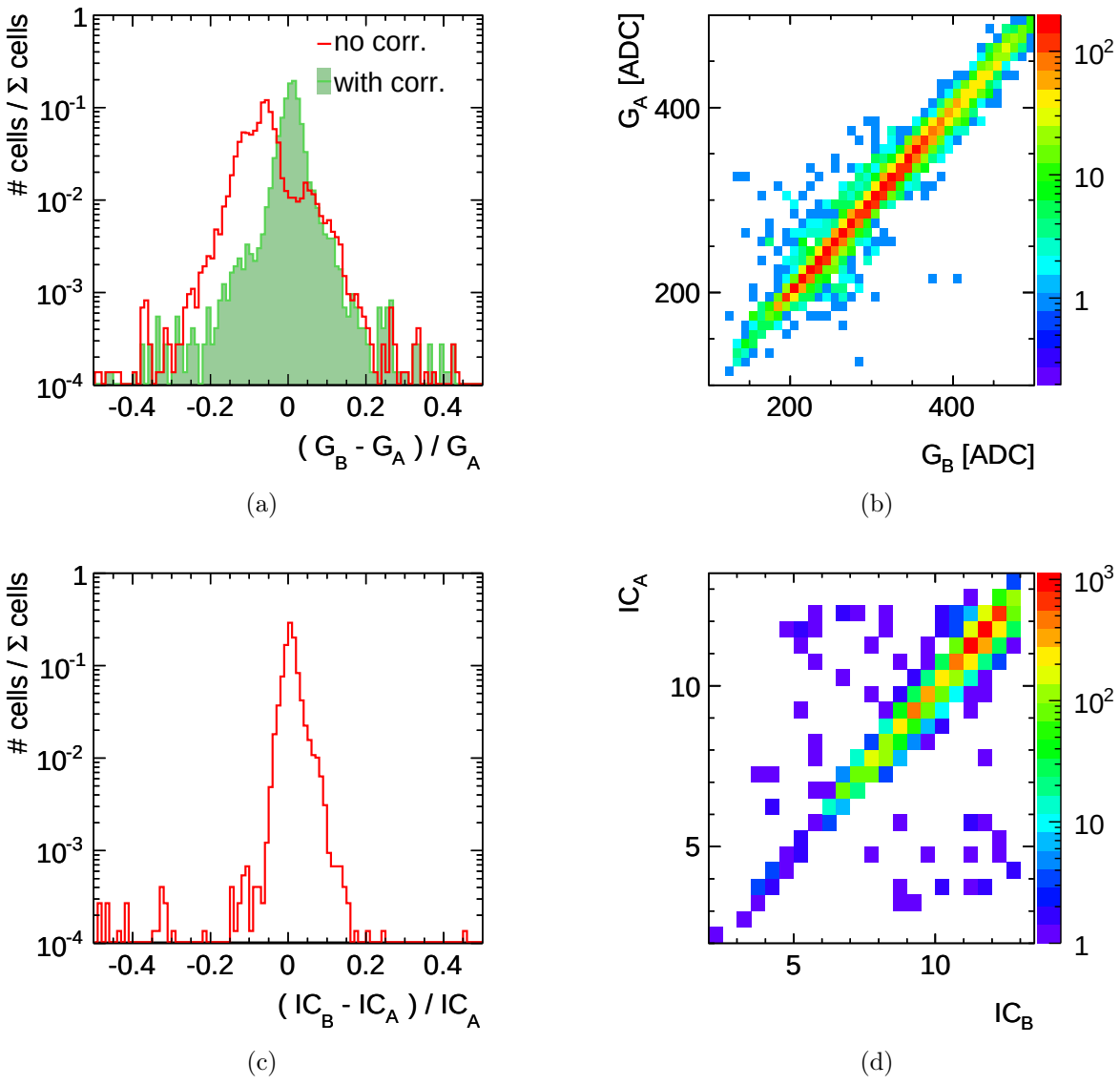

Figure 3.13: (a) Difference between native (G_{A}) and non-native (G_{B}) gain calibration factors before and after correcting for the effects of voltage and temperature differences between these sets. (b) Correlation between the native and non-native gain calibration factors after correcting for the effects of voltage and temperature differences. (c) Difference between electronics intercalibration factors obtained at native (IC_{A}) and non-native (IC_{B}) operating conditions. (d) Correlation between the native and non-native electronics intercalibration factor measurements (the electronics intercalibration factors are independent from operating voltages and temperatures).

Chapter IV

Calibration Studies

The calibration of a calorimeter like the AHCAL physics prototype requires robust procedures which can be commonly applied to all cells. This calibration aspect becomes even more important when proposing the AHCAL technology for a detector at a collider experiment (like the ILD mentioned in the Introduction) where the number of readout channels amounts to several million. The response of all cells needs to be equalized to a common physics signal and the stability of the calibration for each cell needs to be monitored during operation. Section 4.1 discusses the muon calibration factors applied for equalizing the responses of all AHCAL cells for the test-beam data used for the analysis presented in this thesis. This section also covers the correction of these factors for temperature changes. The possibility to transport muon calibration factors to different operating conditions and varying experimental setups is evaluated in Section 4.2. Section 4.3 presents measurements of the bias voltage dependence of the SiPM response, while Section 4.4 introduces procedures for identifying single dead, noisy, or unstable cells that deteriorate the overall detector performance and response homogeneity. Section 4.5 covers the sensitivity of the AHCAL response to uncertainties of the signal threshold which are caused by the uncertainties of the muon calibration factors. Finally, systematic uncertainties induced by correcting for the non-linear SiPM response are discussed in Section 4.6.

4.1 Cell Response Equalization with Muons

The analysis presented in this thesis is based on data collected at fixed SiPM bias voltages. The muon calibration factors used to equalize the responses of all AHCAL cells for these data are extracted from a set of muon measurements performed at an average detector temperature T of $(25.3 \pm 0.3)\,^{\circ}\mathrm{C}$ and a mean difference between the applied bias voltage and the breakdown voltage of all the SiPMs of 4 V. At these operation conditions, the mean light yield of all cells is $14.0\,\frac{\mathrm{pixel}}{\mathrm{MIP}}$. Only cells with energy depositions above 0.5 MIP, which are termed hits, are used for analysis. With this threshold cut, the average detection efficiency of single AHCAL cells for MIP-like energy depositions is 94% [45].

The average AHCAL temperature during the collection of the electron and pion data used for this analysis ranges from 24 °C to 28 °C. Therefore, the response variations of the SiPMs with temperature need to be accounted for. An average temperature dependence of the muon response of $-3.4\,\frac{\%}{\mathrm{K}}$ is applied to extrapolate the muon calibration factors of all

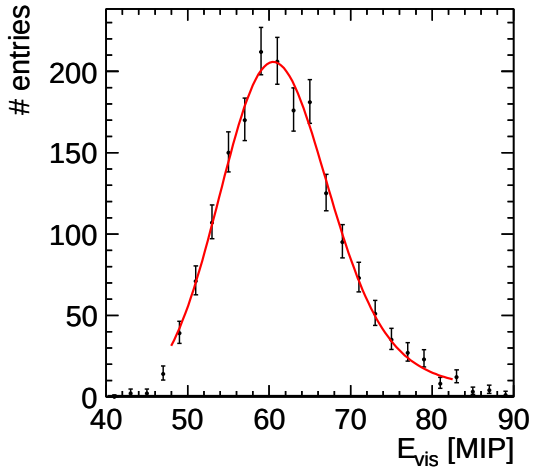

Figure 4.1: Measurement of the total AHCAL response to single muons and the result of performing a fit of a Landau distribution convolved with Gaussian function to this distribution.

cells to the temperature of each measurement. This value is determined from muon data collected at the same operating voltage and in the same temperature range as the electron and pion data.

A Landau distribution convolved with a Gaussian function describes the AHCAL response to muons. Because the Gaussian function only accounts for the smearing of the signal due to noise, the mean of the Gaussian is fixed to zero. Figure 4.1 presents the fit result for a single set of measurements. The uncertainty of the most probable value is estimated by varying the fit parameters within their errors (taking correlations into account). The requirements for selecting only single-muon events are described in Section 6.5.

On average, 14 noise hits contribute to the total AHCAL response (depending on the temperature, see Section 4.4). Subtracting the mean noise contribution from the peak position of the convolved function yields the most probable muon signal $\langle E^{\mu}_{\text{vis}} \rangle_0$.

Figure 4.2(a) shows $\langle E^{\mu}_{\text{vis}} \rangle_0$ for different mean detector temperatures without applying any correction for temperature effects. Measurements with a pure 32 GeV muon beam, more than 250 events, and a mean noise contribution of less than 10 MIP are selected. Fits are accepted if they yield yield a $\frac{\chi^2}{\text{NDF}} < 2$. Two third of the selected measurements meet the $\frac{\chi^2}{\text{NDF}}$ requirement. Squares mark measurements that are used for extracting the muon calibration factors. The dotted line in Fig. 4.2(a) shows the result of performing a linear fit to the measurements. The fit yields a slope of $-3.4\,\frac{\%}{\text{K}}$ with respect to the applied muon calibration, i.e. with respect to $\langle E^{\mu}_{\text{vis}} \rangle_0$ at 25.3 °C. This slope is in agreement with previous measurements performed under different operating conditions.

Figure 4.2(b) shows $\langle E^{\mu}_{\text{vis}} \rangle_0$ for different mean detector temperatures for muon data collected in-between the pion data which are used for the analysis presented in this thesis. Temperature corrections are applied and the most probable muon signals scatter around a constant line. The standard deviation of these values divided by the mean is 1.6% and is an estimate of the overall AHCAL calibration uncertainty after temperature correction. This error does not cover uncertainties induced by correcting for the non-linear SiPM response (discussed in Section 4.6), because muon energy measurements are not affected by this.

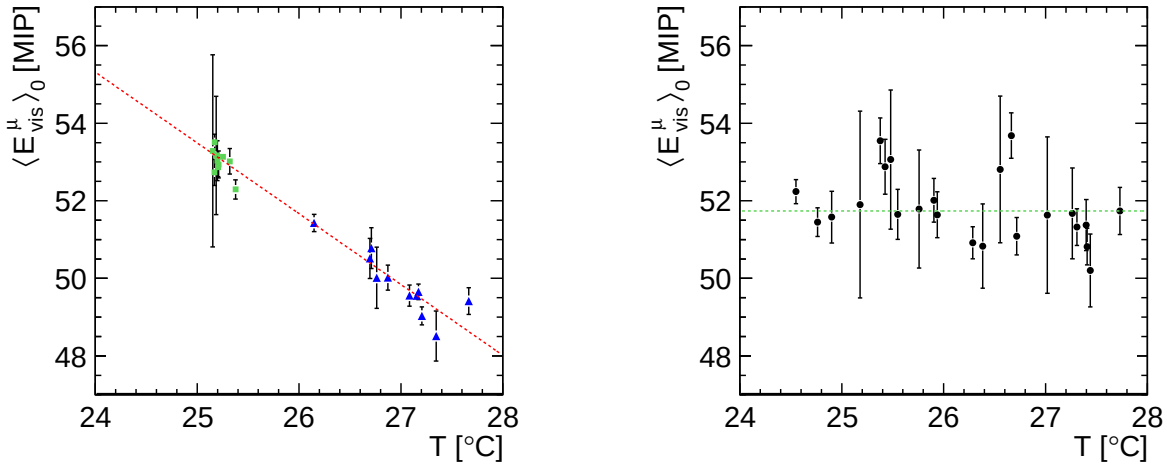

(a) (b)

Figure 4.2: (a) AHCAL response $\langle E^{\mu}_{\text{vis}} \rangle_0$ to muons from dedicated muon measurements at as a function of the detector temperature. Temperature effects are not corrected for. Squares represent measurements used for extracting the muon calibration factors. The dashed line indicates the result of a linear fit performed on all measurements. (b) AHCAL response $\langle E^{\mu}_{\text{vis}} \rangle_0$ to muons measured in between pion measurements at different detector temperatures. Temperature effects are corrected for. The dashed line marks the mean of the response measurements (51.5 MIP).

The 1.6% calibration uncertainty is of the same order as the 2% uncertainty of extracting the muon calibration factor for an individual cell [33].

Figure 4.3 shows the mean energy per layer for muons after subtracting the mean noise in each layer. The line marks the mean response of all layers at 1.43 MIP (the mean of a Landau distribution is larger than its most probable value). The standard deviation of the energy in individual layers divided by the mean is 8%. This value is an estimate for the uncertainty of the energy measurement in a single cell after extrapolating the respective muon calibration factor to a different temperature. Due to the single-cell MIP detection efficiency of 94%, on average the signals from 35 cells out of 38 cells in a tower contribute to the AHCAL response to single muons. Therefore, the uncertainty on the response is expected to be about $\frac{8\%}{\sqrt{35}} = 1.4\%$ and agrees with the 1.6% observed before.

4.2 Muon Calibration Portability

As mentioned before, the calibration of the AHCAL requires to equalize the signals from all cells to a reference physics process and this equalization is achieved by measuring the response of each individual cell to muons acting as MIPs. Collecting enough statistics for calibrating the 38 layers of the AHCAL physics prototype with high-intensity muon beams in test-beam facilities takes about 12 hours of beam time. Because of the need for high muon statistics in each cell, the layers of a calorimeter for a future collider detector like the ILD need to be calibrated with dedicated muon beams before installation.

The SiPM response changes with operation voltage and temperature. Usually, the bias

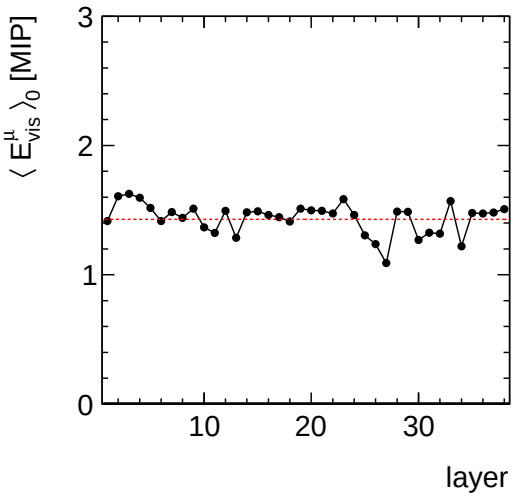

Figure 4.3: Mean AHCAL response $\langle E^{\mu}_{\text{vis}} \rangle_0$ per layer for muon measurements after subtracting the mean noise per layer (extracted from random trigger events). The dashed line marks the mean response of all layers (1.43 MIP).

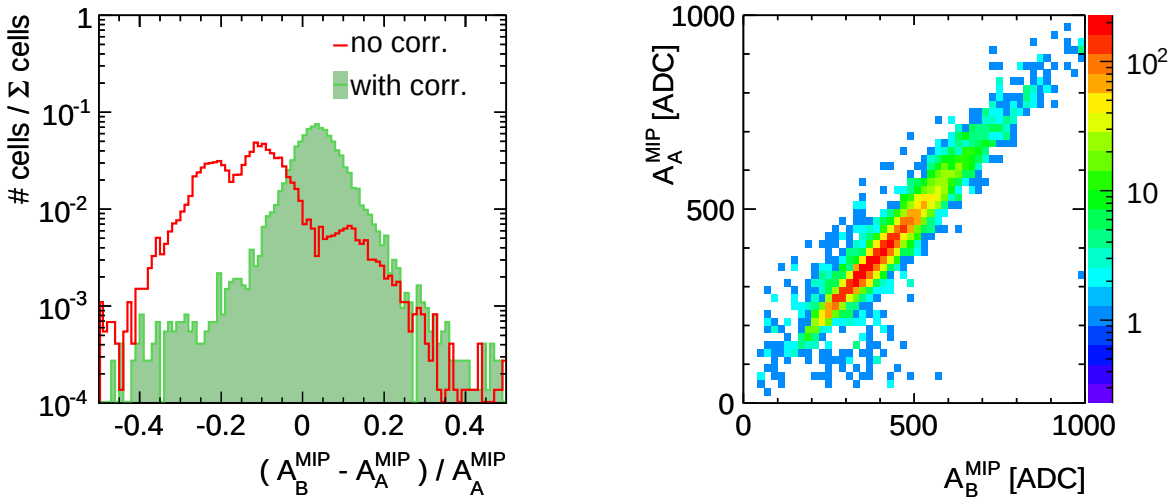

(a) (b)

Figure 4.4: (a) Difference between native ($A_{\text{A}}^{\text{MIP}}$) and non-native ($A_{\text{B}}^{\text{MIP}}$) muon calibration factors before (open histogram) and after (filled histogram) correcting for the effects of voltage and temperature differences. (b) Correlation between the native and non-native muon calibration factors after correcting for the effects of voltage and temperature differences.

voltage does not change during operation. However, compensation for temperature changes or the optimization of operation parameters may require adjustments of the bias voltages. Knowing the voltage dependence of the SiPM response allows to apply a set of muon calibration factors to data measured with different operation voltages instead of re-doing the muon calibration after each voltage change. This procedure is crucial for proposing a calorimeter for a collider experiment where the operation voltages may need adjustment but a muon calibration of the installed layers is not feasible on short time scales. Furthermore, transporting the muon calibration to different experimental setups and operating conditions is an alternative to repeating the extraction of new muon calibration factors with AHCAL physics prototype at the start of a new test-beam operation or after adjusting the SiPM bias voltages.

For the SiPMs used in the AHCAL physics prototype, the mean temperature dependence of the breakdown voltage is $65\,\frac{\mathrm{mV}}{\mathrm{K}}$ [37]. Given the temperature dependence of the muon calibration factors applied to reconstruct the data used in this thesis ($-3.4\,\frac{\%}{\mathrm{K}}$, see Section 4.1) and the temperature dependence of the breakdown voltage, the mean voltage dependence of these calibration factors is $-3.4\,\frac{\%}{\mathrm{K}}/65\,\frac{\mathrm{mV}}{\mathrm{K}} = 5.2\,\frac{\%}{100\,\mathrm{mV}}$. This set of muon calibration factors is referred to as native calibration. A second set of muon calibration factors extracted with a different experimental setup (at a different test-beam facility) and under different operation conditions (bias voltage and temperature) has a mean voltage dependence of $5.6\,\frac{\%}{100\,\mathrm{mV}}$, which is consistent with the different reference for the relative slope [37]. This set is termed non-native muon calibration. The native calibration is extracted from a 32 GeV muon beam, the non-native calibration from an 80 GeV muon beam. The expected increase of the most probable muon energy deposition for 80 GeV muons with respect to 32 GeV muons is about 0.5% [60, 61].

Figure 4.4(a) shows the difference between the native ($A_{\mathrm{A}}^{\mathrm{MIP}}$) and non-native ($A_{\mathrm{B}}^{\mathrm{MIP}}$) muon calibration factors before (open histogram) and after (filled histogram) correcting for the effects of different temperatures and voltages (the non-native calibration is shifted to the voltage and temperature of the native calibration). Due to different voltage adjustments applied to different groups of SiPMs between the measurements, the open histogram shows three peaks. The corrections reduce the mean difference from -12% to 4%, which is 3.5% larger than the expected difference due to the different muon energies. The overcorrection is of the same order as the response change with 1 K and is attributed to the uncertainty of the temperature measurement in the AHCAL due to the limited number and the distribution of the temperature sensors. After corrections, the remaining standard deviation of the differences divided by the mean is reduced from 12% to 8%. Considering the 3% uncertainty of each calibration set, the spread increases by 7% due to the transport of the calibration constants. Between the extraction of the two calibration sets, about 10% of the front-end electronics cards were replaced (because of transport damages). The parameters of the cards have a spread of 5% between individual devices. This contributes to the 7% spread observed when comparing the two calibration sets after corrections. Figure 4.4(b) illustrates the correlation (correlation factor 95%) between the native and non-native muon calibration factors after correcting for the voltage and temperature differences between these sets.

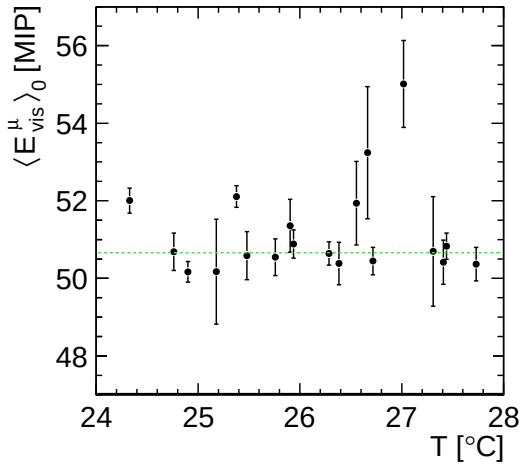

Figure 4.5: AHCAL response $\langle E^{\mu}_{\text{vis}} \rangle_0$ to muons measured in between pions at different detector temperatures. The data are calibrated using the non-native muon calibration factors. Effects of different operating voltages and temperatures are corrected for. The dashed line marks the mean of the response measurements (50.5 MIP).

Applying Non-native Muon Calibration Factors

Figure 4.5 presents the most probable energy deposition of muons measured at different temperatures calibrated with the non-native muon calibration. The effects of voltage and temperature differences between the measurements and the calibration factors are corrected for. No temperature dependence is visible, i.e. the correction for different measurement temperatures works with the non-native calibration. Comparing these results to Fig. 4.2(b) (the same measurements calibrated with the native muon calibration factors), the mean response is shifted downwards by 2% (50.5 MIP instead of 51.5 MIP) and the spread between the measurements increases by a factor two (3.3% instead of 1.6%).

These studies demonstrate the possibility to transport a set of AHCAL muon calibration factors to a different experimental setup and to different operation conditions. The SiPM behavior is robust and understood well enough for this purpose. The transport procedure shifts the MIP scale with respect to using a native calibration. This shift is absorbed by the final calibration to the GeV scale. Therefore, it is possible to calibrate the layers of a calorimeter using the AHCAL technology in a collider detector with muon beams before installation and to correct these calibration factors for the effects of changing bias voltages or temperatures during operation. The impact of using non-native muon calibration factors on the linearity and the resolution of the AHCAL response to single electrons and the impact on the response to single pions are discussed in Sections 7.3 and 8.1, respectively.

4.3 Long-range Bias Voltage Scans

The procedures applied to correct the AHCAL muon calibration factors for temperature changes and to transport these parameters to different operating conditions assume a linear dependence of the SiPM response A on the temperature T and the applied bias

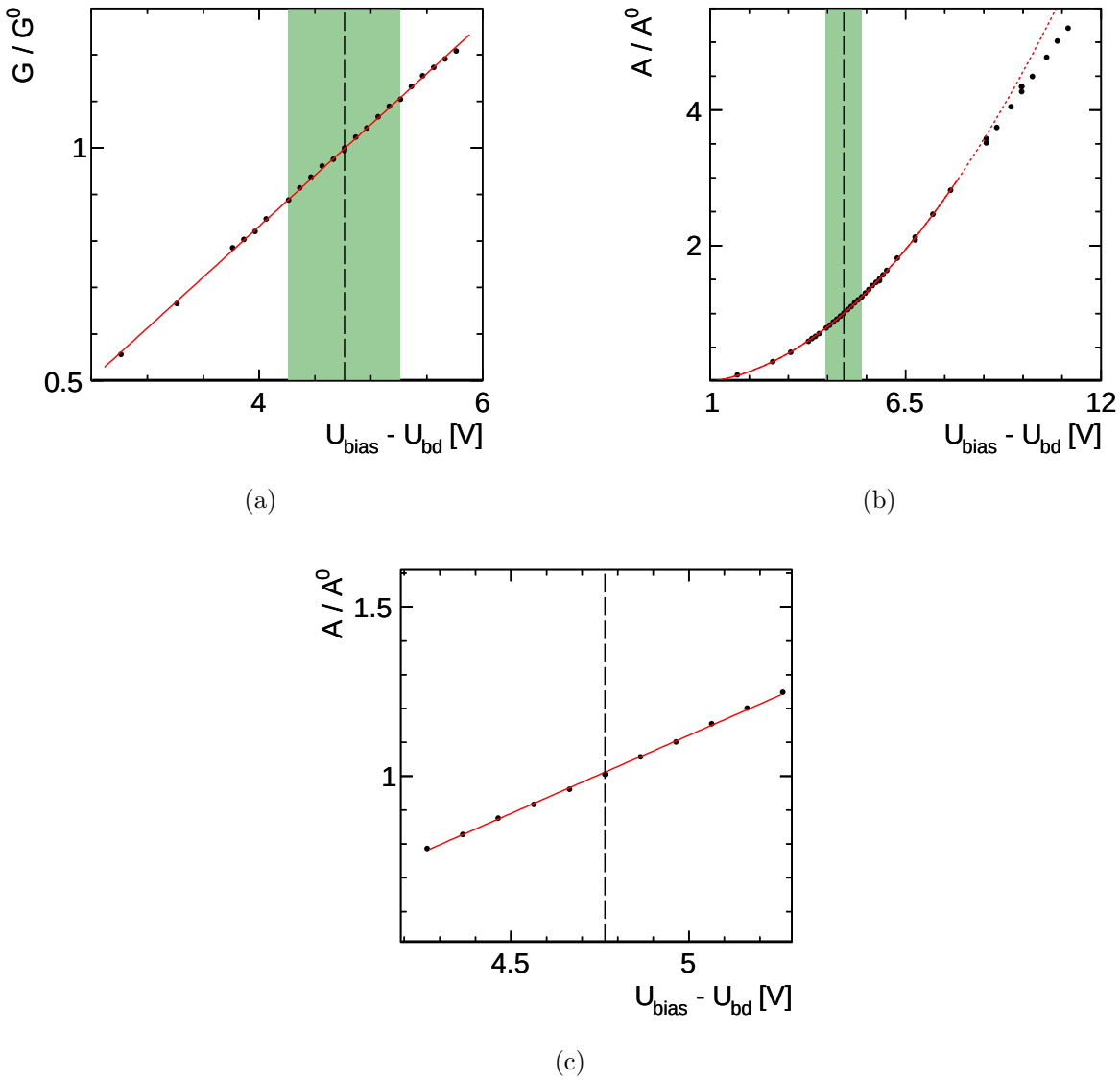

(a) (b)

(c)

Figure 4.6: (a) SiPM gain G (of a single AHCAL cell) normalized to G^0 at nominal bias voltage U_{nom} as a function of the difference between bias voltage U_{bias} and breakdown voltage U_{bd}. The solid line shows the result of performing a linear fit to all measurements. (b) Response A (of a single AHCAL cell) to LED light of fixed intensity normalized to the response A^0 at $U_{\text{bias}} = U_{\text{nom}}$ as a function of $U_{\text{bias}} - U_{\text{bd}}$. The solid line shows the result of a performing a second order polynomial fit to the measurements between $U_{\text{bias}} - U_{\text{bd}} = 1\,\text{V}$ and $U_{\text{bias}} - U_{\text{bd}} = 8\,\text{V}$. The dotted line indicates the extension of the fit result to higher $U_{\text{bias}} - U_{\text{bd}}$. (c) Close-up view of the voltage scan of A/A^0 in the maximum test-beam operation range and the result of a linear fit performed to these measurements. The dashed line in (a-c) marks $U_{\text{bias}} = U_{\text{nom}}$. The shaded area in (a-b) indicates the estimated test-beam operation range for this SiPM ($U_{\text{nom}} \pm 0.5\,\text{V}$).

voltage U_{bias}. As discussed in Section 2.3.1, the SiPM gain G and the photon detection efficiency ε depend linearly on the effective bias voltage $U_{\text{bias}} - U_{\text{bd}}$, where U_{bd} is the SiPM breakdown voltage U_{bd} and scales linearly with T. Because A scales with $G \cdot \varepsilon$, a non-linear dependence of A on the effective bias voltage, i.e. on both U_{bias} and on T, is expected. For large effective bias voltages, ε saturates and the U_{bias} and T dependence of A converge towards the respective dependencies of G.

Measurements of G and A for different effective bias voltages (varying U_{bias} at fixed T) allow to test the linearity expectation of G and to estimate the uncertainty introduced by assuming a linear dependence for correcting A for U_{bias} and T changes. Two modules of the AHCAL physics prototype are used for these measurements. Figures 4.6(a) and 4.6(b) present measurements of G and A (response to LED light of fixed intensity) for a single SiPM mounted on a tile in the AHCAL physics prototype as a function of the effective bias voltage. The measurements are normalized to G^0 and A^0, which are G and A at the nominal operating voltage U_{nom} for this SiPM. The dashed line marks the effective bias voltage for $U_{\text{bias}} = U_{\text{nom}}$. The shaded area indicates an estimate of the maximum effective bias voltage range covered by the AHCAL operation during test-beam measurements. The range extends over 1 V and accounts for T variations of up to 10 K, which change U_{bd} by approximately 0.7 V, and U_{bias} adjustments applied for optimizing the AHCAL performance, which are commonly of the order 0.3 V. The mean detector temperature during these measurements is 21 °C and varies by less than 0.5 °C (the spread of the measurements at the same effective bias voltage reflects the temperature variation).

A linear fit performed to all gain measurements in Fig. 4.6(a) yields a good description of the effective bias voltage dependence of G over the full voltage range covered. All studied SiPMs show the same behavior. This result confirms the expectation that the gain depends linearly on the effective bias voltage (and therefore on U_{bias} and T) even beyond the range of effective SiPM bias voltages relevant for the AHCAL test-beam operation.

A second order polynomial performed to the LED response measurements in Fig. 4.6(b) between $U_{\text{bias}} - U_{\text{bd}} = 1\,\text{V}$ and $U_{\text{bias}} - U_{\text{bd}} = 8\,\text{V}$ describes the measurements well and confirms the non-linear voltage dependence of the SiPM response. The extension of the fit result to higher effective bias voltages shows a disagreement between the curve and the measurements that increases with increasing effective bias voltages. This effect is attributed to the saturation of the photon detection efficiency. The maximum test-beam operation region lies several volts below the saturation region. All other investigated SiPMs behave similarly.

Figure 4.6(c) presents a close-up view of the measured A/A^0 for the estimated range of test-beam operation voltages and a linear fit applied to the measurements. The maximum deviation of the second order polynomial fit from the linear fit in this voltage range is below 2%. This is an upper limit for the uncertainty introduced by approximating the relation between SiPM response and bias voltage (or temperature) by a straight line. In a range of 0.3 V around the nominal voltage, which corresponds to the temperature range of 4 K covered by the data used in this thesis, the maximum deviation between the second order polynomial and the linear fit result is below 0.2%. Therefore, using a polynomial instead of a linear relation to correct the response for temperature variations is not expected to improve the performance of the temperature correction procedure. For simplicity, the linear approximation is used.

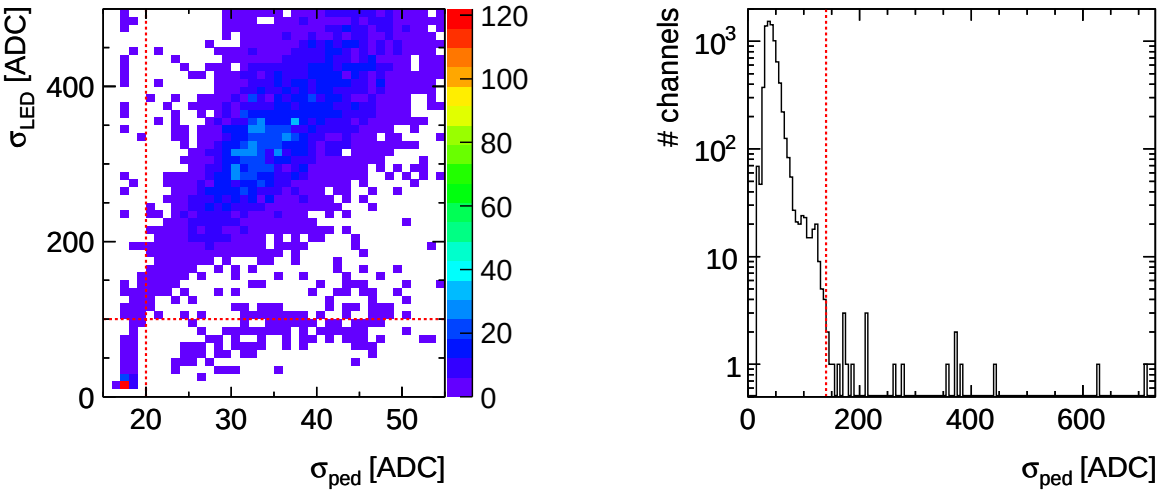

(a) (b)

Figure 4.7: (a) Correlation between the minimum pedestal width for each AHCAL channel from a series of random-trigger measurements (σ_{ped}) and the minimum pedestal width from a series of LED measurements (σ_{LED}). The dashed lines mark $\sigma_{\text{ped}} = 20\,\text{ADC}$ and $\sigma_{\text{LED}} = 100\,\text{ADC}$, respectively. (b) Maximum σ_{ped} for each channel from a series of pedestal measurements. The dashed line marks $\sigma_{\text{ped}} = 140\,\text{ADC}$.

4.4 Identifying Dead, Noisy, and Unstable Cells

Some of the 7608 cells of the AHCAL physics prototype are dead or noisy. Dead cells are attributed to badly soldered or broken SiPM connections, while noisy cells are ascribed to SiPMs with long-discharge behavior, i.e. unstable currents. All dead and noisy cells need to be identified and excluded from analysis. Dead cells not removed from Monte Carlo simulations lead to different detector responses in data and in simulations. Noisy cells disturb the homogeneity and stability of the detector response both in data and in simulations. Two types of measurements allow for identifying these cells: Pedestal measurements using a random trigger and LED measurements using the LED system to illuminate all AHCAL cells with a constant amplitude. The pedestal measurements are either performed separately with 20000 events per measurement or in blocks of 500 events during the intervals between beam spills. The LED measurements are performed in blocks of 500 events between beam spills.

The pedestal width σ_{ped} (i.e. the standard deviation of the signal for random-trigger events) of dead cells is less than 20 ADC levels [31]. However, some cells with a pedestal width below this limit respond to LED light. Thus, only cells with a pedestal width of less than 20 ADC levels and an width σ_{LED} of less than 100 ADC levels during LED illumination are considered dead. For the classification of each cell, the lowest pedestal width and LED width from a series of noise and LED measurements is used. Figure 4.7(a) illustrates this selection.

Long discharge SiPMs show an increased pedestal width and channels with a maximum pedestal width of more than 140 ADC levels are assigned to this group of cells. Figure 4.7(b) presents this threshold. Figure 4.8(a) shows the noise frequency for all

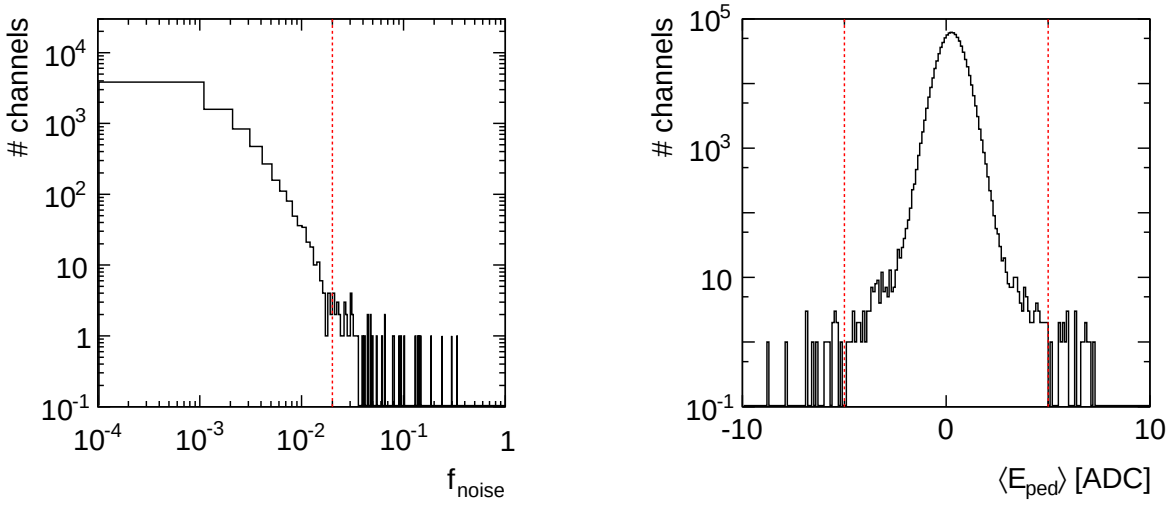

(a) (b)

Figure 4.8: (a) Noise hit frequency f_{noise} above 0.5 MIP threshold for all cells and a series of pedestal measurements. The dashed line indicates $f_{\text{EM}} = 0.02$. (b) Mean pedestal (after subtracting the mean of a subset of the events from same measurement). Each entry corresponds to the maximum mean A_{ped} found for one AHCAL channel in a series of pedestal measurements. The thresholds $A_{\text{ped}} = -5$ and $A_{\text{ped}} = 5$ are represented by the dashed lines.

AHCAL cells. The noise frequency of a cell is the fraction of pedestal events in which the cell gives a signal above the 0.5 MIP threshold. Cells with a noise frequency of more than 0.02 are classified as noisy. Figure 4.8(b) shows the mean pedestal A_{ped} of each cell after pedestal subtraction. By construction, this value should be at zero ADC levels for cells with stable pedestal. Cells for which A_{ped} deviates by more than 5 ADC levels from zero are considered unstable. A few channels show pedestal shifts which result in multiple peaks in the pedestal histogram for a single noise measurement. Channels with more than one peak are considered unstable and are excluded from subsequent analyses. Table I summarizes the numbers of cells meeting the different selection criteria for dead, noisy, or unstable cells.

In total, 3.5% of the AHCAL cells are suppressed both for the analysis of data and Monte Carlo simulations. The excluded cells are not distributed equally over the AHCAL. Figure 4.9(a) shows the number of removed cells in the individual AHCAL layers for the data collected at Fermilab in 2008 and 2009. Modules 3 and 30 are the modules with most suppressed cells. Figure 4.9(b) gives the number of suppressed cells in single AHCAL towers in layers 1-30 (the coarse modules in layers 31-38 are not taken into account). The figure shows that there are no areas in lateral direction where removed cells pile up.

Figures 4.10(a) and 4.10(b) illustrate the improvement due to the exclusion of dead, noisy, and unstable cells from analysis. Figure 4.10(a) shows the noise signal above the 0.5 MIP threshold (E_{vis}) in the AHCAL and Fig. 4.10(b) shows the mean noise signal above threshold ($\langle E_{\text{vis}} \rangle$) for all AHCAL layers for random trigger events in-between beam spills. The open histogram and round markers represent the result before and the filled histogram and square markers represent the result after the exclusion of dead, noisy, and unstable cells identified by the procedures described in this section. Excluding the noisy

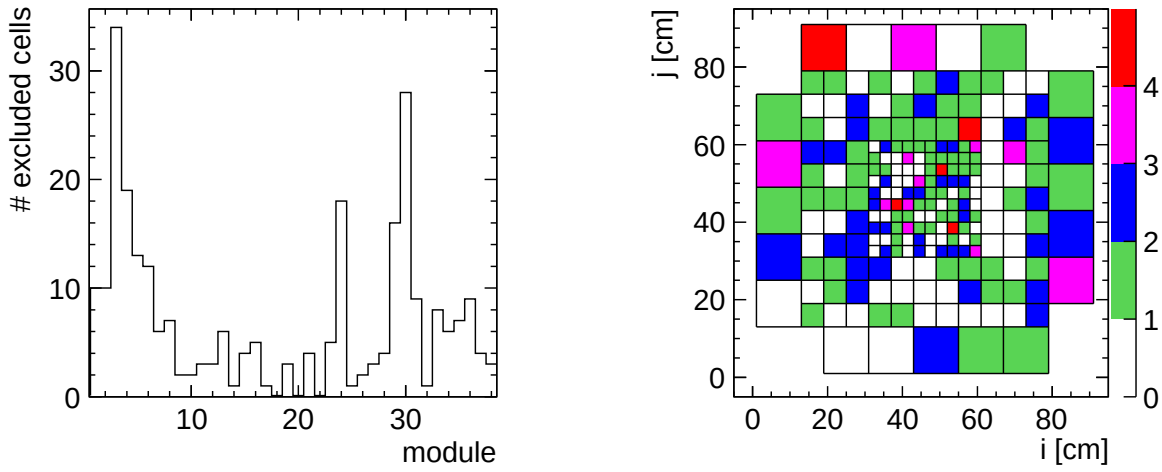

(a) (b)

Figure 4.9: (a) Number of excluded cells in all AHCAL modules. (b) Front view of the AHCAL layers 1-30 (the other 8 layers have a coarser granularity in the center, see Section 2.6). The i and j coordinates give the lateral position of a cell inside a module. The colors reflect the number of suppressed cells for each tower (cells at the same lateral position in each layer).

and unstable cells reduces the long tail in the noise distribution (dead cells do not contribute to the noise). Figures 4.11(a) and 4.11(b) show the same for the number of hits above the 0.5 MIP threshold in the AHCAL. The layer-to-layer fluctuations are due to different SiPM production batches used to equip individual layers.

Figures 4.12(a) and 4.12(b) present the mean noise signal and the number of hits above the 0.5 MIP threshold for random trigger events collected at different mean detector temperatures after applying temperature corrections to the muon calibration factors. The noise increases by 3 MIP (40%) or 5 hits over 4 K. The mean noise occupancy in the AHCAL is about 0.16%, which is roughly one order of magnitude higher than the initial design goal.

TABLE I
STATISTICS OF DEAD, NOISY, AND UNSTABLE CELLS.

Selection	Cells
$\sigma_{\text{ped}} < 20 \wedge \sigma_{\text{LED}} < 100$	204
$\sigma_{\text{ped}} > 140$	22
noise rate > 0.02	55
multiple peaks	17
$A_{\text{ped}} < -5 \vee A_{\text{ped}} > 5$	9
total	270

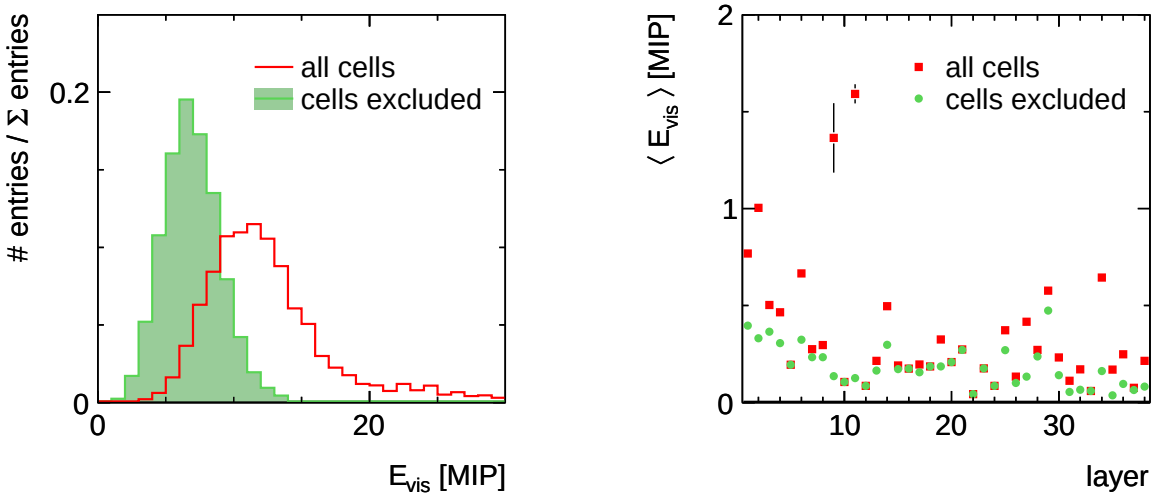

(a) (b)

Figure 4.10: (a) Noise signal E_{vis} (above threshold) in the complete AHCAL and (b) mean noise signal $\langle E_{\text{vis}} \rangle$ for the single AHCAL layers from random trigger events. The open histogram in (a) and circles in (b) represent the respective measurements including all cells, whereas the filled histogram in (a) and the squares in (b) show the result after excluding all dead, noisy and unstable cells. This noise measurement is not included in the set of measurements used for identifying the cells to suppress.

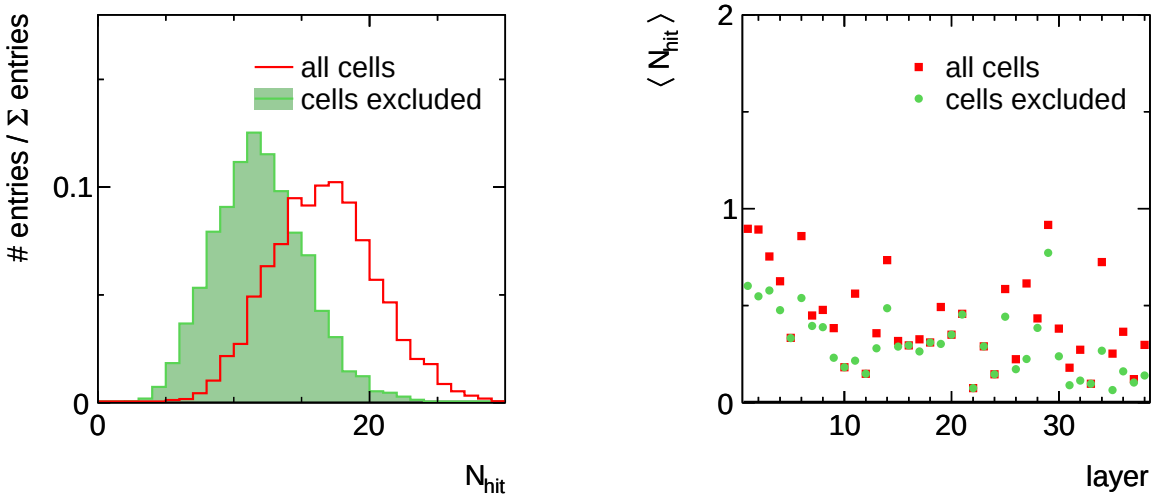

(a) (b)

Figure 4.11: (a) Number of hits N_{hit} (above threshold) in the complete AHCAL and (b) mean number of hits $\langle N_{\text{hit}} \rangle$ for the single AHCAL layers from random trigger events. The open histogram in (a) and circles in (b) represent the respective measurements including all cells, whereas the filled histogram in (a) and the squares in (b) show the result after excluding all dead, noisy and unstable cells. This noise measurement is not included in the set of measurements used for identifying the cells to suppress.

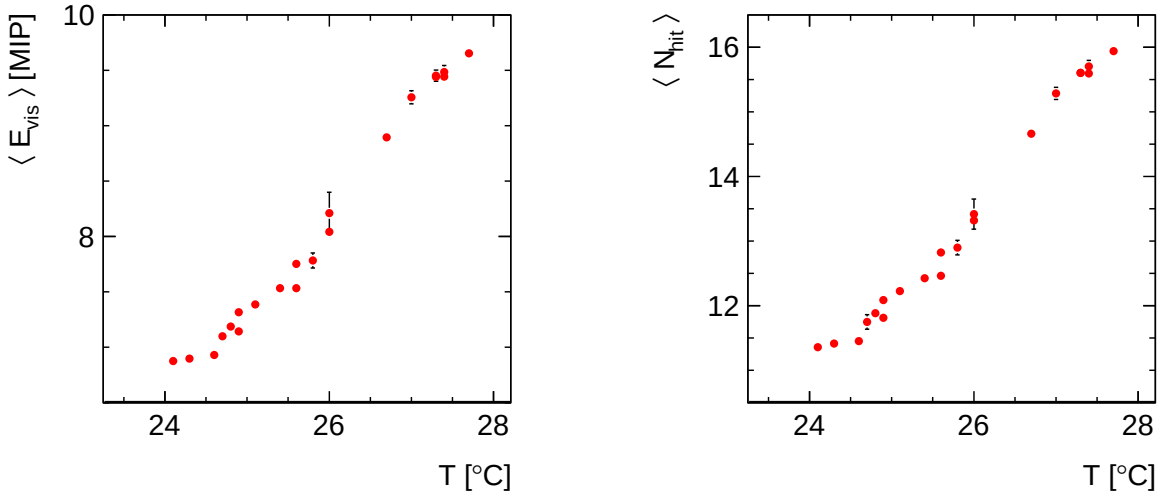

(a) (b)

Figure 4.12: (a) Mean noise signal $\langle E_{\text{vis}} \rangle$ and (b) number of hits $\langle N_{\text{hit}} \rangle$ (above 0.5 MIP threshold) from random trigger events as a function of the mean AHCAL temperature after correcting the muon calibration factors for the effects of temperature changes.

4.5 Uncertainties Induced by Varying Signal Thresholds

The minimum energy deposition in a single cell considered during analysis is 0.5 MIP. This threshold ensures a noise occupancy of about 0.16% at a MIP detection efficiency of 94%. A higher threshold reduces both the noise occupancy and the MIP detection efficiency. Furthermore, a higher threshold reduces the AHCAL response to particles of fixed energy. Uncertainties on the muon calibration of the AHCAL cells have the same effect, because they effectively shift the threshold. The MIP calibration uncertainty of a single AHCAL cell is of the order 8 which corresponds to a threshold uncertainty of 0.04 MIP.

Figure 4.13(a) presents the AHCAL response to pions of different energies (from test-beam measurements) after subtracting the mean signal from random trigger events and using a MIP threshold increased (c^+) and lowered (c^-) by 8% divided by the response for the default threshold. The black lines show these ratios for random-trigger events. Figure 4.13(b) shows the same ratio for the number of cells above threshold. These figures show that the noise level in the AHCAL is very sensitive to changes of the threshold, while the response to pions is much more stable. This is an upper limit for the response uncertainties due to uncertainties of the MIP threshold, because a common threshold shift for all cells in the same direction is assumed.

4.6 Uncertainties Due to the Non-linear SiPM Response

The uncertainty of the AHCAL response introduced by correcting for the non-linear SiPM response increases for higher energy densities and contributes 0.5% to the calibration uncertainty for 10 GeV electrons and 1.4% to the calibration of 20 GeV electrons [33]. The electron analysis presented in this thesis uses the value for 10 GeV also for lower beam

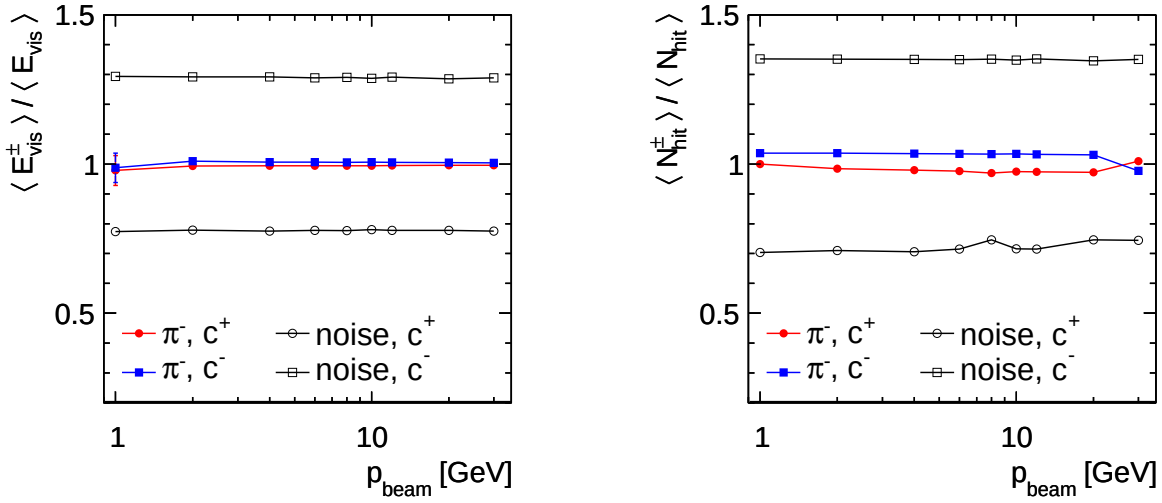

(a) (b)

Figure 4.13: Ratio between the measured (a) AHCAL response $\langle E^{\pm}_{\mathrm{vis}} \rangle$ and (b) number of hits $\langle N^{\pm}_{\mathrm{hit}} \rangle$ for increased (lowered) signal thresholds and the threshold applied for analysis ($\langle E_{\mathrm{vis}} \rangle$, $\langle N_{\mathrm{hit}} \rangle$) for pion measurements and random-trigger events (noise) at different beam momenta.

momenta. This is a conservative error assumption, because the saturation-induced errors are expected to decrease further with decreasing electron momentum.

The impact of uncertainties of the correction for the non-linear SiPM response is smaller for pions than for electrons because the average energy density in pion cascades is much smaller than the average energy density in purely electromagnetic cascades of the same energy. For pions of 40 GeV and below, the error from the saturation correction is below 0.5% and decreases with decreasing pion energy [30]. The value of 0.5% is used as upper estimate for the saturation uncertainty for calibrating the pion data presented in this analysis. More detailed studies to establish the uncertainties introduced by the saturation correction are ongoing [62].

The 1.6% uncertainty of the muon calibration is the dominant source of uncertainty for electron measurements below 10 GeV and pion measurements below 40 GeV. Extensive studies to refine the uncertainties induced by the saturation correction are ongoing [62].

Chapter V

Simulation

Simulations play a key role in research and development of new technologies like detectors in particle physics. They can predict the performance of different technology options and allow for optimizing design parameters. However, the predictive power of simulations requires the prior validation of the simulations with measurements.

The ILD detector concept follows the Particle Flow approach to obtain the aspired jet energy resolution. As explained in Chapter 1, this approach requires reliable clustering algorithms which exploit the information from highly granular calorimeters. Accurately predicting the performance of these algorithms demands a realistic simulation of the spatial development of electromagnetic and hadron cascades in matter.

The physics of electromagnetic cascades is well understood. The simulation of these cascades is reliable in the energy range relevant for most particle physics applications. Simulating hadron interactions with matter is more challenging. There are different competing models trying to describe these interactions in different energy ranges. Extensive validation studies are necessary to assess the accurateness of these models. Section 5.1 gives an overview of several models for hadron interactions with matter provided by the simulation toolkit Geant4.

Apart from correct predictions for the physics processes involved, a good description of the detector geometry and material is crucial for reliable simulations. The modeling of the AHCAL with the Geant4 based Monte Carlo application Mokka is discussed in Section 5.2, while Section 5.3 covers the digitization procedure, which incorporates detector effects like inter-tile crosstalk and noise in the simulation.

5.1 Simulating Particle Interactions with Matter

Geant4 (Geometry and Tracking) is a versatile software toolkit for the simulation of particle interactions with matter. This toolkit is used for a wide range of applications in different fields from particle physics to radiation protection, medicine, and space sciences. Geant4 allows the user to choose the physics processes that are considered in the simulation and the models applied for these processes. Unless stated otherwise, Geant4 version 9.4 (with patch 01) is used for all simulations presented in this thesis.

The physics of electromagnetic cascades is described in Section 1.1.1. The processes that are involved are well understood. Only electrons, positrons, and photons are produced in the interactions. GEANT4 provides a standard model for the simulation of electromagnetic processes [63]. The accuracy of GEANT4 predictions for the electromagnetic response of sampling calorimeters in high-energy physics experiments is better than 1% [64].

As discussed in Section 1.1.3, the physics of hadron cascades is more complex than the physics of purely electromagnetic cascades. Hadron cascades involve a large variety of different processes. The individual processes involve interactions between composite objects mediated by the strong force and cannot be calculated analytically. Furthermore, each process can generate a large variety of secondary particles. GEANT4 provides implementations of several models for the description of hadron interactions with matter. Most models uses certain approximations and assumptions that are only valid in limited energy ranges. To extend the covered energy range, different models (each valid at different energies) are combined to so-called physics lists. Sections 5.1.1 and 5.1.2 give an overview of the models and physics lists that are used for the validation studies presented in Chapter 8.

GEANT4 uses a range cut to limit the tracking of secondary particles produced in interactions. Particles with energies so low that they cannot travel a distance larger than the range cut in the current medium are not tracked further and their energy is deposited immediately. Larger range cuts yield more precise predictions at the cost of longer computing times and larger disc space usage. Usually, a range cut in the order of the typical dimensions of the simulated geometry is used.

5.1.1 Models for Hadron Cascade Physics

GEANT4 provides implementations of different models for describing the inelastic scattering of single hadrons on atomic nuclei. Due to the composite nature of both the projectile and the target and the involvement of the strong force, these interactions cannot be calculated from first principles (e.g. using non-pertubative Quantum Chromodynamics).

The de Broglie wavelength $\lambda_{dB} = \frac{h}{p}$ of a projectile hadron with momentum p defines the scale of the substructures in the target nucleus that are relevant for the interaction, where h is Planck's constant. At low energies the individual nucleons inside a nucleus have to be considered, whereas at high energies the quark substructure of the projectile and a single target nucleon are the relevant structures.

There are two classes of models available in GEANT4, parametrized models and theory-driven models. The following paragraphs describe the basic assumptions and features of the most important models for hadron cascades.

GEANT4 provides a model extension for high precision treatment of low energy neutrons. This extension yields a more precise prediction for the energy depositions from late neutrons in a hadron cascade. High precision neutron models depend on an evaluated neutron library for cross sections, angular distributions, and final state information [65].

Cascade Models

Between energies of a few hundred MeV and a few GeV, the de Broglie wave length of the projectile is comparable or shorter than distance between nucleons inside a nucleus,

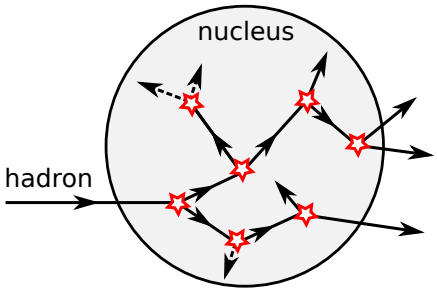

Figure 5.1: Sketched working principle of cascade models implemented in GEANT4. The projectile hadron and all secondary hadrons are tracked through the nucleus and interact with single nucleons until all secondaries are absorbed or leave the nucleus. See text for a more detailed description of these models.

but still large enough so that the quark-substructure of individual nuclei can be neglected. This energy range is the regime of cascade models. Cascade models consider all nucleons in a nucleus. A projectile hadron is tracked through the nucleus and interacts with nucleons without taking the quark-substructure into account. The path length between individual interactions inside the nucleus is calculated from the modeled nucleon densities and parametrized cross-sections. Secondary particles are tracked through the nucleus in a similar way as the initial projectile and may interact again, be absorbed, or leave nucleus. Figure 5.1 illustrates the basic concept of cascade models.

Cascade models treat the nucleus as a Fermi gas, i.e. the nucleons occupy all states of the system up to the Fermi energy. The Pauli exclusion principle imposes a minimum energy larger than the Fermi energy for secondary particles created in the interactions.

Collisions between projectiles and nucleons excite the nucleus. GEANT4 characterizes this excitation by excitons, i.e. the number of excited particles and holes. After all secondary particles have left the nucleus or got absobed, the remaining nuclear fragments are transferred to an equilibrium state and de-excited.

GEANT4 provides implementations for the Bertini cascade model [66] and the binary cascade model [67]. The models differ in the modeling of the nucleon densities inside a nucleus and the treatment of the individual hadron-nucleon interactions.

The Bertini cascade model describes a nucleus as spherical shells of constant nucleon density. The nucleons inside a shell are assumed to have a Fermi-gas momentum distribution. At each collision, the model directly calculates the momentum of the struck nucleon, the type of the reaction, and the reaction products and their four momenta. The Bertini cascade model includes a pre-equilibrium model to describe evaporation using the exciton configuration. The model also describes the de-excitation of the nucleus via Fermi-breakup, a simple explosion model, a phenomenological fission model, and an evaporation model at equilibrium.

The binary cascade model describes the nucleus with discrete nucleons (with defined position and momentum). The positions of the nucleons are sampled from a Wood-Saxon distribution (for heavy nuclei) or a harmonic oscillator shell model (for light nuclei). The nucleon momenta are randomly selected between zero and the Fermi momentum. In this model, the initial state of scatterings between a hadron and a nucleus is transfered to the interaction products via an intermediate step. The collisions generate hadronic resonances

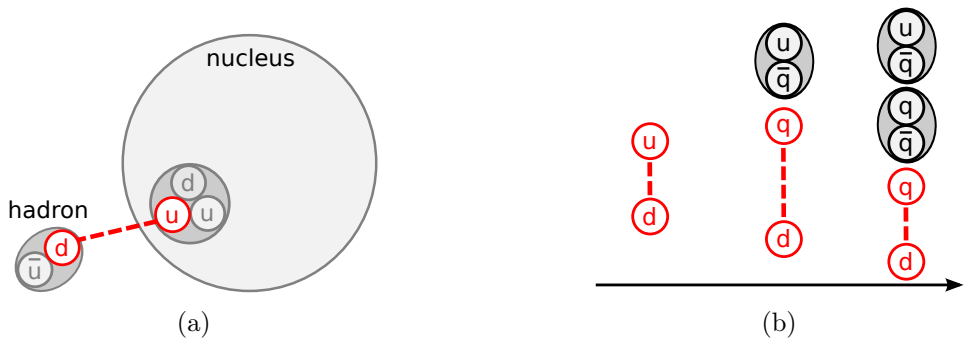

Figure 5.2: Sketched working principle of string models implemented in GEANT4. (a) String formation between one quark from the projectile hadron and one quark from the target nucleon. (b) String fragmentation via the generation of quark-antiquark pairs and hadronization. See text for a more detailed description of these models.

(e.g. Δ or N). The decay of these resonances is treated based on experimental branching ratios (provided by the Particle Data Group [10]) and produces secondary particles. The binary cascade model features no built-in pre-equilibrium or de-excitation models. At the end of the cascade, the exciton configuration is transfered to external models to handle the corresponding processes.

Parton String Models

Parton string models describe the scattering of high-energy hadrons on nuclei at high energies (usually above 5 GeV). At these energies, interactions between individual quarks of the projectile and the nucleons in the target nucleus govern the scattering process. The struck nucleus is modeled with protons and neutrons using the potential of a harmonic oscillator for light nuclei (with $A < 16$) or the Wood-Saxon potential for heavier nuclei. A randomly chosen momentum between zero and the Fermi momentum is assigned to each nucleon. The projectile interacts with a single nucleon. The interaction is predicted based on the impact parameter of the incoming hadron, the center of mass energy of the interaction, and inelastic and diffractive cross sections. A string is formed between two quarks (one from the projectile and one from the target nucleus). The string is described by its four-momentum and the two quarks on its ends. The string stretches due to constituent movement. Interactions with other nuclei excite the string. The model splits the string into quark-antiquark pairs (or diquark-antidiquark pairs) and new strings. The quarks form hadrons (hadronization). The fragmentation continues as long as the string energy is high enough for further splitting. Figures 5.2(a) and 5.2(b) illustrate the string formation and fragmentation.

GEANT4 provides two implementation of string-parton models, the Fritiof model and the quark-gluon string model. The models differ in the string formation and the string fragmentation. The Fritiof approach describes diffractive hadronic interactions of the projectile with a nucleon via momentum exchange. The quark-gluon string model uses Pomerons to mediate this scattering process. The models use different fragmentation function for the string fragmentation. More details are given in [68, 69, 70, 71].

At the end of the string fragmentation, an excited nucleus in a non-equilibrium state and

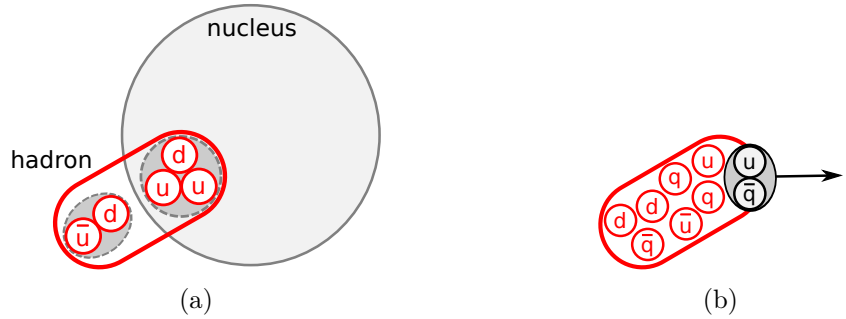

Figure 5.3: Sketched working principle of the chiral invariant phase-space model implemented in GEANT4. (a) A Quasmon is formed from the quarks of the projectile and a target nucleus. (b) The Quasmon decays via quark fusion (or quark exchange with neighbor nucleons). See text for a more detailed description of this model.

several secondary particles are left. The secondaries are propagated through the nucleus using one of the cascade models or the precompound model. The transition to equilibrium and the de-excitation of the nucleus uses the precompound model and de-excitation models [65]. Alternatively, the fragmentation of an excited nucleus can be handled by the chiral-invariant phase-space model.

Precompound and De-excitation Models

The native precompound and de-excitation models in GEANT4 handle the fragmentation of residual nuclei left behind by the quarks-gluon string model, the Fritiof model, or the binary cascade. The precompound model describes emission of protons, neutrons, and light ions in the precompound stage (before a nuclear system reaches equilibrium). The de-excitation model takes care of evaporation (of neutrons, protons, or light fragments), Fermi-breakup, fragmentation, fission, and photon emission at equilibrium [72].

Chiral Invariant Phase-space Model

The chiral invariant phase space model is a quark-level nuclear fragmentation model. The model uses the concept of Quasmons to model excited nuclear matter. A Quasmon is an excited intermediate state of massless quarks (only up-, down-, and strange-quarks are considered) that are asymptotically free. The quark partons are homogeneously distributed over an invariant phase space. A Quasmon is initially formed from the quarks of the projectile hadron and the quarks of a single target nucleon. The calculations assume a maximum (or critical) temperature of the system. An increase of the Quasmon energy that would rise the temperature above the critical temperature results in the generation of new quark-antiquark pairs rather than an increase of the heat of the system. Quasmons decay gradually via quark fusion and emission of hadrons and by double quark exchange with neighbor nucleons. Figures 5.3(a) and 5.3(b) illustrate the Quasmon formation and decay.

The chiral invariant phase-space model describes hadron-nucleon interactions both at the quark level and the nucleon scale. Thus, in contrast to the string and cascade models,

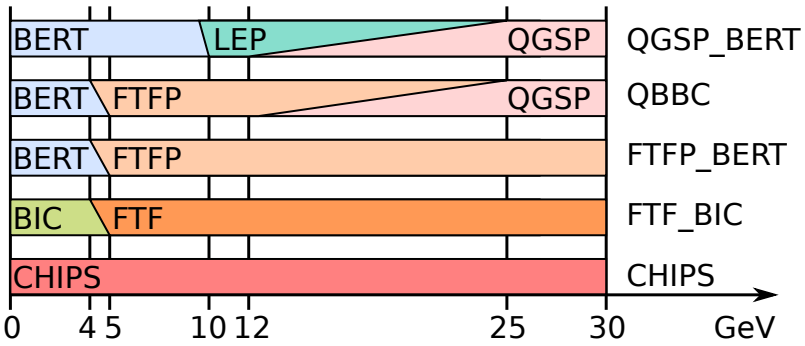

Figure 5.4: Model content of the GEANT4 physics lists used for the simulations presented in this thesis (all physics lists use the respective models applied at 30 GeV for higher energies as well).

it is applicable at all center of mass energies. However, the modeling of Quasmons has to be implemented for each projectile type separately.

The chiral invariant phase-space model is widely used in combination with other models to treat photonuclear reactions and is capable of handling the de-excitation of nuclei resulting from string model calculations. More information about this model are given in [49].

Parametrized Models

Parametrized models are based on fits to experimental data to predict the production of secondary particles in hadronic cascades. No detailed modeling of the interactions is done. Energy is only conserved on average by these models, but not on an event-by-event basis. GEANT4 provides parametrized models for low (LEP) and high (HEP) energies adapted from the GHEISHA hadronic package [73]. Because of several known deficiencies in the description of hadronic cascades, these models are not considered state-of-the-art any more. However, they still serve as stop-gaps for energy ranges not covered by other models or for the simulation of particle types for which no valid models are available.

5.1.2 GEANT4 Physics Lists

Several GEANT4 physics lists for the simulation of hadron interactions with matter exist. A physics list combines different models that are valid for different energy ranges. The transition between models is done smoothly in a range of energy overlap. In this range, one model is randomly chosen for each incoming particle. The probability for choosing one of the models changes linearly in this region. Some models only describe certain types of hadron projectiles. Thus, some physics lists use different models for different hadrons. Independent of the initial projectile, the majority of secondaries created in a hadron cascade are pions. Thus, the models used for pions dominate the cascade for all kinds of primary hadrons.

The analysis presented in this thesis focuses on six physics lists considered to give the best performance in describing hadron cascades: QGSP_BERT, QGSP_BERT_HP, FTFP_BERT, FTF_BIC, QBBC, and CHIPS. Table I and Fig. 5.4 summarize the models used by these physics lists for simulating pions of different energies. All these physics

lists use common code for describing electromagnetic cascades, i.e. no differences in the prediction of electromagnetic physics is expected from the different physics lists. The following paragraphs describe the most important features of these physics lists and results from several validation efforts. A more detailed description of the physics lists is given in [74, 75].

QGSP_BERT and QGSP_BERT_HP

At high energies, the QGSP_BERT physics list employs the quark-gluon string model to describe inelastic pion-nucleon scattering, followed by the external precompound and de-excitation models. At low energies, this physics list uses the Bertini cascade model with its built-in precompound and de-excitation algorithms. The gap at intermediate energies is filled with the LEP model.

According to validation studies done by LHC experiments using pion test-beam data between 3 GeV and 300 GeV [76, 77], the QGSP_BERT physics list from GEANT4 version 9.2 gives better agreements with data than the FTF-based physics lists or CHIPS. QGSP_BERT overestimates the pion response by 2-3% and shows discontinuities in the energy dependence of the response at the transition regions between the individual models. This physics lists underestimates the pion resolution by less than 10%. The analysis of CALICE AHCAL and Si-W ECAL data at beam energies between 8 GeV and 80 GeV [49] confirm an overestimation of the response by QGSP_BERT in GEANT4 9.3 (AHCAL: 4-7%, Si-W ECAL: 10%) at 50 Gev-80 GeV and an underestimation by up to 5% at low energies. Analyses of ATLAS test-beam data show that QGSP_BERT in GEANT4 9.3 underestimates the longitudinal pion shower length by 10% and the lateral shower extension by 15% [78].

The QGSP_BERT_HP physics list is an extension of QGSP_BERT using the high precision neutron treatment. Measurements of the time structure of 10 GeV pion cascades in tungsten show that using the high-precision neutron tracking considerably reduces the number of late energy depositions in the cascade which brings the simulation of the timing in agreement with measurements, while large discrepancies are observed for QGSP_BERT [79].

FTFP_BERT and FTF_BIC

The FTFP_BERT physics list describes high-energetic inelastic pion-nucleon scattering with the Fritiof model. In this physics list, the Fritiof model is used in combination with external precompound and de-excitation models. Secondaries created inside the nucleus are treated by the precompound model as well. At low energies, the Bertini cascade in combination with the external precompound and de-excitation models is used.

At high energies, the FTF_BIC physics list uses the Fritiof model in combination with a specialized cascade model for the handling of secondaries and followed by the external precompound and de-excitation models. At low energies, the binary cascade followed by the stand-alone precompound and de-excitation models is used.

Thanks to recent tuning efforts, both the FTFP_BERT and FTF_BIC physics lists are emerging alternatives for QGSP_BERT. LHC experiments found the longitudinal and

lateral shape agreements for FTFP_BERT in GEANT4 version 9.3 similar to the agreements for QGSP_BERT [49]. Both FTFP_BERT and FTF_BIC agree within 5% with data colleted by the CALICE AHCAL and Si-W ECAL between 8 GeV and 80 GeV. The agreement is achieved for all observables investigated [49]. The AHCAL and Si-W ECAL responses are overestimated by the simulations above 30 GeV and underestimated at lower energies. Shower depth and radius are underestimated in the simulations. The performance of these physics lists is found better than the performance of QGS-based physics lists. These studies could not show a significant difference between the two cascade model (Bertini or binary) due to the energy range covered (data above 8 GeV, cascade models only become dominant below 5 GeV).

QBBC

The QBBC physics lists uses the quark-gluon string model to describe pion interactions at high energies and the Bertini cascade model at low energies. For intermediate energies, the Fritiof model is applied. For protons and neutrons below 1.5 GeV, this physics list applies the binary cascade model, whereas for protons and neutrons of higher energies it uses the same models as for pions. Due to secondary protons and neutrons in pion cascades, this model may give different predictions than FTFP_BERT, although FTFP_BERT uses the same pion models as QBBC below 12.5 GeV. No results from extensive validation studies for this physics list are available yet.

CHIPS

The Chiral-invariant phase space model is applicable at all pion energies. Thus, the CHIPS physics list uses only one model. This list is particularly interesting because it uses only one model for all hadron energies and avoids effects from the transition from one model to another. The CHIPS physics list is still in an experimental stage. CHIPS is available since GEANT4 9.3.

The analysis of the CALICE AHCAL pion data [49] at beam energies between 8 GeV and 80 GeV shows an energy independent overestimate of the response and the shower length by 10% for the CHIPS physics list in GEANT4 version 9.3.p01. This overestimate is attributed to an improper implementation of low-energy neutron cross sections. The shower radius is described better than 5%. GEANT4 version 9.4 provides a significantly advanced version of CHIPS.

Comparison of Different GEANT4 Versions

Some models are still under development and the predictions from different versions of GEANT4 may vary. Simulation studies using the AHCAL detector model described in Section 5.2 (without applying the digitization procedure described in Section 5.3) show that the predictions for the detector response to electrons between 1 GeV and 20 GeV agrees between GEANT4 9.4 and GEANT4 9.3. better than 1%.

Figures 5.5 shows the ratio of the predictions from GEANT4 9.4 and GEANT4 9.3 for the mean AHCAL response to pions at different energies using different physics lists. The mean response decreases from version 9.3 to 9.4 by up to 10% for the Fritiof-based models

TABLE I
COMPOSITION OF GEANT4 PHYSICS LISTS.

Physics list	Model (for $\pi^{\pm}$)	Energy range
QGSP_BERT	Bertini cascade (BERT)	$\leq 9.9\,\mathrm{GeV}$
	Low-energy parametrization (LEP)	9.5 GeV - 25 GeV
	Quark-gluon string model (QGSP)	$\geq 12\,\mathrm{GeV}$
QBBC	Bertini cascade (BERT)	$\leq 5\,\mathrm{GeV}$
	Fritiof string model (FTFP)	4 GeV - 25 GeV
	Quark-gluon string model (QGSP)	$\geq 12.5\,\mathrm{GeV}$
FTFP_BERT	Bertini cascade (BERT)	$\leq 5\,\mathrm{GeV}$
	Fritiof string model (FTFP)	$\geq 4\,\mathrm{GeV}$
FTF_BIC	Binary cascade (BIC)	$\leq 5\,\mathrm{GeV}$
	Fritiof string model (FTF)	$\geq 4\,\mathrm{GeV}$
CHIPS	Chiral-invariant phase space model	$\geq 0\,\mathrm{GeV}$

at high energies, whereas the response predicted by the quark-gluon string model remains unchanged within 2% in this energy range. At low energies, the response from all three physics lists decreases by about 3%.

5.2 Detector Modeling

MOKKA is a GEANT4 based Monte Carlo application capable of simulating detectors in test-beam setups and full detector geometries for collider experiments [80]. This application provides the detector geometries, while GEANT4 simulates the interactions of particles with matter to predict the energy deposited in sensitive detector volumes. A detailed model of the AHCAL physics prototype is implemented in MOKKA and described in [81]. Models for other CALICE detectors and beam line instrumentation are also available. The beam line material, the beam position, and the beam spread are simulated with adequate accuracy (see Appendix A).

Simulations of energy depositions in scintillators have to account for shielding (or quenching) effects giving rise to a non-linear light yield per unit length ($\frac{\mathrm{d}L}{\mathrm{d}x}$) at high ionization densities ($\frac{\mathrm{d}E}{\mathrm{d}x}$). Birks' law [82] describes this effect with

$$\frac{\mathrm{d}L}{\mathrm{d}x} \propto \frac{\mathrm{d}E}{\mathrm{d}x} \cdot \frac{1}{1 + k_{\mathrm{B}} \cdot \frac{\mathrm{d}E}{\mathrm{d}x}}. \tag{5.1}$$

The AHCAL simulations presented in this thesis use the GEANT4 implementation of Birks' law with a Birks factor of $k_{\mathrm{B}} = 0.007943\,\frac{\mathrm{cm}}{\mathrm{MeV}}$ [83].

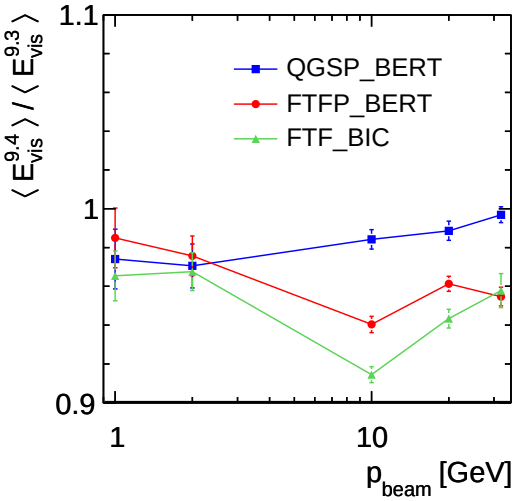

Figure 5.5: Ratio between the AHCAL response to pions predicted by different GEANT4 physics lists in version 9.4 ($\langle E_{\text{vis}}^{9.4} \rangle$) and version 9.3. ($\langle E_{\text{vis}}^{9.3} \rangle$).

The signal shaping time of the AHCAL physics prototype is 150 ns. This parameter limits the time for detecting energy depositions, i.e. signals arriving later than 150 ns are not recorded. The AHCAL simulation takes this time cut into account by considering only energy depositions up to 150 ns after the beginning of an event. The time cut affects the AHCAL response to hadrons because late energy depositions in hadronic cascades (e.g. from low-energetic neutrons) are not measured.

As mentioned in Section 5.1, GEANT4 uses a range-cut to limit the tracking of secondary particles. The default range-cut for simulating CALICE detectors is 0.05 mm. This value is two orders of magnitude smaller than the relevant dimensions in the CALICE detectors (the scintillator layers are 5 mm thick). Studying the range-cut dependence of the simulated AHCAL response to muons, electrons, and pions shows a plateau of the response around the range cut of 0.05 mm, which ensures the stability of the simulation.

5.3 Digitization of Detector Effects

Detector characteristics like signal generation processes, readout electronics, noise, and calibration procedures affect all measurements. Comparing measurements to theoretical predictions or simulations requires to either unfold physics signals and detector effects or to include these effects in the simulation. The second procedure is called digitization of the simulation and is used in this thesis. Both approaches require detailed knowledge about all detector characteristics that can affect a measurement. This section describes the digitization procedure for the AHCAL. The digitization is implemented within the MARLIN framework (Modular Analysis and Reconstruction for the Linear Collider, [84]). After digitization, simulations are treated the same way as data for calibration and analysis.

The AHCAL digitization procedure includes several steps and accounts for the real cell dimensions, inter-tile light cross talk, the conversion from the GeV to the MIP scale, effects of the non-linear SiPM response, and noise. The inter-tile light crosstalk is simulated by

distributing a fraction of the energy deposited in each cell to all neighboring cells. This distribution assumes a light leakage of 2.5% per 3 cm tile edge. The simulated energy depositions in the scintillator material are converted to the MIP scale using the a most probable energy deposition of 816 $\frac{\text{keV}}{\text{MIP}}$ from simulated muons in single scintillator tiles as scaling factor.

For simulating the SiPM response, the energy depositions in all tiles are converted from the MIP scale to the corresponding number of SiPM pixels using measurements of the light yield of the SiPM-tile systems. For each cell, the number of corresponding pixels is corrected for the non-linearity of the SiPM response using measured response functions. The resulting number of firing pixes is smeared with a Poisson distribution to account for statistical fluctuations of the pixel statistics. The numbers of pixels are converted to signals in ADC levels, i.e. the native scale of measurements with the real AHCAL physics prototype.

The final digitization step is the addition of pedestal measurements to each cell. At this level, the same calibration procedures and analysis algorithms can be applied to both data and digitized simulations. Cells that are dead in the real detector or excluded from the analysis for other reasons (e.g. high noise) are removed from the digitized simulations. More details about the AHCAL digitization procedure is given in [85].

In order to bring the simulations as close to the measured data as possible, the pedestal is extracted for each measurement separately. In addition, the calibration factors used in the digitization procedure are shifted to the respective temperatures of the measurements.

Chapter VI

Event Selection

The analysis presented in this thesis uses muon, electron, and pion data collected without the Si-W ECAL or the Sci-ECAL being installed. This chapter presents basic beam quality criteria and offline selection procedures enhancing the purity of tagged electron, pion, and muon samples. Section 6.1 describes tower-based tracking algorithms applied for the identification of muons with the AHCAL and the TCMT and an algorithm for clustering AHCAL hits and locating the first inelastic hadron-nucleus interaction in a hadronic cascade. Section 6.2 summarizes basic beam quality criteria applied for all particle types, while Sections 6.3, 6.4, and 6.5 present dedicated selection criteria for electrons, pions, and muons. To optimize the purity of the data sets while keeping a maximum of the available statistics, different selection criteria are used at different beam momenta. Some of the event selection criteria use information from the AHCAL itself. Therefore, Section 6.6 studies the bias introduced by these criteria to the mean visible energy in the detector using digitized Monte Carlo simulations. Section 6.7 discusses the purity of the collected electron and pion data after applying the event selection criteria described in the corresponding sections.

6.1 Algorithms Applied for Event Selection

This section briefly describes the AHCAL and TCMT based tracking algorithms and the clustering algorithm for the AHCAL which are used in the following sections. The performance of these algorithms is evaluated in Appendix B.

AHCAL and TCMT Tracking

The fine granularity of imaging calorimeters allows for finding ionization tracks from muons or charged hadrons. Muons traversing the AHCAL or TCMT physics prototype are identified by counting the hits (above 0.5 MIP) in single calorimeter towers. If the number of hits reaches a predefined threshold, the corresponding tower is considered to encompass an ionization track. The cells at the same position in each AHCAL layer belong to the same tower. Therefore, the AHCAL cell sizes define the tower dimensions. The lateral extensions of the TCMT towers ($5 \times 5\,\mathrm{cm}^2$) are marked-off by the overlap between scintillator strips with different orientation. The track position inside an AHCAL or TCMT tower cannot

be measured, because the exact location of an energy deposition inside a single scintillator tile or strip is not known.

Clustering and First Inelastic Hadron Interaction

The high granularity of the AHCAL allows to apply cluster-based patter recognition algorithms to locate the first hard interaction of hadrons traversing the AHCAL with absorber atoms. This interaction is regarded as the starting point of the hadronic cascade, whereas before this point charged hadrons behave like MIPs. Some of the event selection criteria presented in this chapter use a clustering algorithm as well.

The clustering algorithm applied in this analysis looks for seed hits with visible energies of more than 1.65 MIP and sorts these hits by their z-positions in ascending order. Starting with the seed hit closest to the origin of the incoming particle, each seed hit and all neighboring hits are assigned to a cluster. As long as one or more of the cells added to a cluster meet the seed hit requirement, the clustering continues and all hits adjacent to these cells are assigned to the same cluster.

The cluster closest to the point a hadron enters the calorimeter with at least 4 hits and more than 16 MIP energy deposition is identified as the beginning of the cascade. The end of the principal cluster axis pointing in the direction of the incoming hadron is used as location of the first inelastic scattering [29].

6.2 Beam Quality Criteria

The experimental setup of the CALICE detector prototypes and auxiliary beam line instrumentation is presented in Section 3.2. The main trigger for measuring electrons, pions, and protons is the coincidence between the signals from two $10 \times 10\,\mathrm{cm}^2$ scintillators. Events in which particles generate a beam trigger signal and are scattered away before reaching the AHCAL are rejected by requiring at least 4 MIP energy deposition in the $3 \times 3\,\mathrm{cm}^2$ cells of the first five layers of the AHCAL. About 96% of pure pedestal events have less energy in this region. Assuming pure pedestal events and spurious trigger events have the same topology (i.e. only noise in the AHCAL), 96% of the latter events are rejected by this cut. According to digitized Monte Carlo simulations, the pion selection efficiency of this cut is 96.5% at 1 GeV and above 99.2% at higher beam momenta. The electron selection efficiency is above 99.9% at all beam momenta.

Some events contain additional particles in the beam halo or particles that initiate a shower before reaching the AHCAL. These events are excluded by requiring no signal in the veto wall. Figure 6.1(a) presents a map of the veto wall efficiency for detecting muons (see Fig. 3.3 for the convention of x- and y-direction). The efficiency is the fraction of muons found by the TCMT tracking algorithm in a $5 \times 5\,\mathrm{cm}^2$ tower that give rise to a signal in the veto wall. A muon beam centered at $x = 0\,\mathrm{mm}$ and $y = 0\,\mathrm{mm}$ and covering the full TCMT front face is used for this estimate. The dotted lines in Fig. 6.1(a) indicate the four separate scintillator planes of the veto wall. The MIP detection efficiency is not homogeneous and is below 40% in two of the scintillator plates. Further investigations indicate problems with the readout of the respective PMTs during data acquisition. Thus, an additional cut is used to compensate for the missing coverage of the veto wall. Less

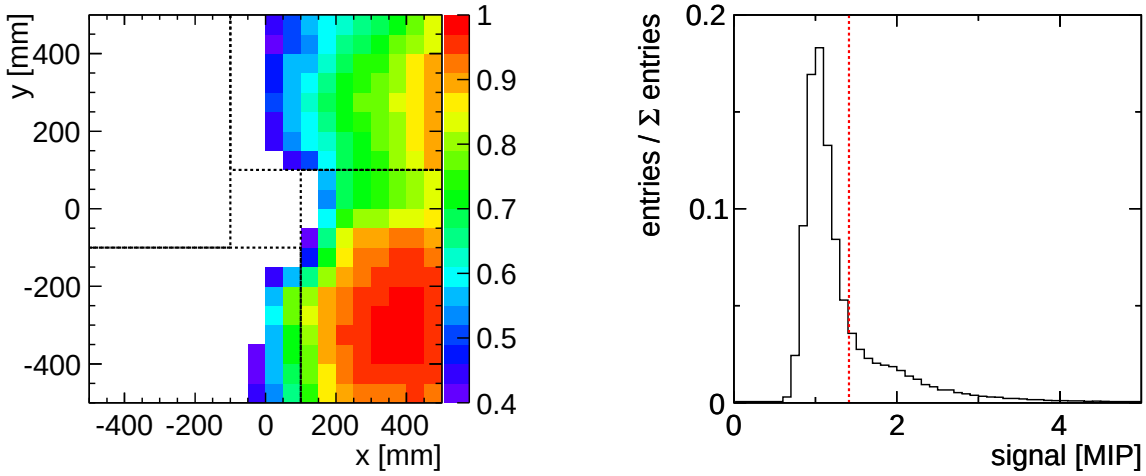

(a) (b)

Figure 6.1: (a) Map of the veto wall efficiency for detecting muons (see Fig. 3.3 for the convention of x- and y-direction). (b) Multiplicity counter signal. The x-axis is calibrated to multiples of MIP-like energy depositions. The dashed line indicates the threshold at 1.4 MIP.

than 15 hits are required in the $6 \times 6\,\mathrm{cm}^2$ and the $12 \times 12\,\mathrm{cm}^2$ cells of the first five AHCAL layers. The pion selection efficiency of this cut is larger than 99.8% at all energies, the electron selection efficiency is above 99.9%.

In order to exclude events with more than one particle depositing energy in the AHCAL at the same time, only events with a multiplicity counter signal of less than 1.4 MIP are kept for analysis. This selection corresponds to a multi-particle contamination of less than 0.1%. Figure 6.1(b) shows the signal from the multiplicity counter calibrated to multiples of MIP-like energy depositions for a set of measurements. The dashed line indicates the cut at 1.4 MIP. The procedure for quantifying the multi-particle contamination is described in [29].

6.3 Electron Selection

Requiring a signal in the outer Čerenkov PMT and no signal in the inner Čerenkov PMT improves the purity of the recorded electron data. In addition, the center of gravity in beam direction has to be in the first half of the AHCAL (less than 360 mm beyond the start of the AHCAL). For 1 GeV data, only events with at least one cluster with an energy of 6 MIP or higher and less than 8 MIP energy deposited in the last 20 AHCAL layers are kept for analysis. The clusters are identified applying the algorithm described in Section 6.1. From 2 GeV to 20 GeV, at least one cluster of 18 MIP energy or higher and less than 5 MIP energy deposited in the last 10 AHCAL layers are required. The cuts are chosen to yield the lowest muon efficiency at an electron efficiency of more than 99.9%. A possible bias introduced by the AHCAL based selection to the electron response is discussed in Section 6.6. The electron and muon selection efficiencies of all studied event selection criteria as a function of the beam momentum are presented in Appendix C.

TABLE I
ELECTRON DATA USED FOR THIS ANALYSIS.

p_{beam}	Events (selected)	Events (all)
1	50991	80275
2	112982	187243
4	64333	99072
6	124289	183409
10	89563	138469
20	63682	95921

Table I gives an overview of all electron data used for this analysis. For all these measurements, the average beam position is near the center of the AHCAL and close to the center of a tile. Because the Čerenkov detector is used for the online trigger decision, part of the Čerenkov based selection is already applied to the data before the offline selection.

Figures 6.2(a) and 6.2(b) present the visible energy for data collected at 1 GeV and 10 GeV beam momentum before (open histograms) and after (filled histograms) applying the event selection for electrons. The main peaks in both figures are the AHCAL response to single electrons. The prominent tails of the distributions to the left removed by the offline event selection are attributed to spurious trigger and pre-showering events. The additional peaks and tails to the right, which are visible before applying the offline event selection, correspond to the AHCAL response to multi-particle events with two or more electrons, pions, or muons in various combinations. The residual second peak at higher energies visible for 10 GeV data after applying the offline event selection originates from events with an additional pion in the detector. The tail contains about 0.9% of the events and is larger than the 0.1% multi-particle contamination expected from the efficiency of the multiplicity counter. Lowering the threshold for the multiplicity counter reduces the overall statistics, but does not reduce the event fraction in the tail. Therefore, the events in the tail are considered multi-particle events in which the additional particles are part of the beam halo and do not traverse the multiplicity counter. The residual left-handed tail at 10 GeV is consistent with a small contribution from single-pion events.

6.4 Pion Selection

For minimizing the electron contamination in pion data, events with a signal in the outer Čerenkov PMT are excluded (see Section 3.3). From 1 GeV to 6 GeV, no signal in the inner Čerenkov PMT is required in addition, while for higher beam momenta the inner PMT has to give a signal. The pion-enhanced data at all beam momenta contain a significant fraction of muon events. The efficiency of the single $1 \times 1\,\text{m}^2$ scintillator behind the TCMT as a muon veto does not suffice to reduce the muon contamination. The muon identification efficiency of this scintillator is approximately 20% and is calculated as the fraction of muon

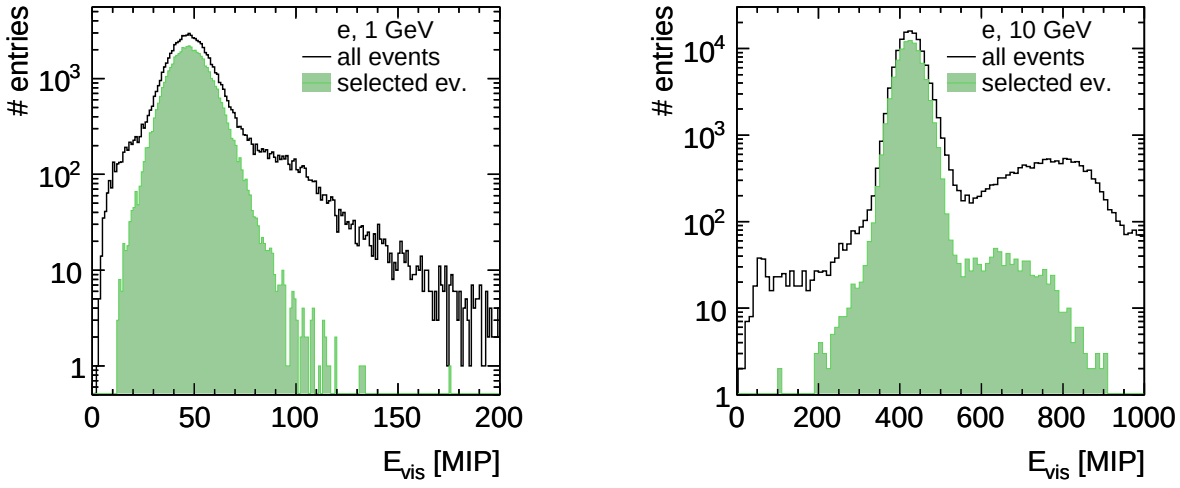

(a) (b)

Figure 6.2: Visible energy E_{vis} for electron measurements at 1 GeV (a) and 10 GeV (b) before (open histograms) and after (filled histograms) applying beam quality and electron selection criteria.

events triggered by the $20\times20\,\text{cm}^2$ scintillator and giving a signal in the $1\times1\,\text{m}^2$ scintillator. Furthermore, low-energetic muons below 3 GeV do not reach the end of the tail catcher but are stopped in the TCMT (≤ 2 GeV) or even in the AHCAL (≤ 1 GeV). Thus, additional algorithms for identifying muon events are needed. The thresholds presented in this section are optimized based on Monte Carlo studies. The cuts at different energies are chosen to yield the smallest muon selection efficiency at a pion efficiency of 95% or more. The pion and muon selection efficiencies of all studied event selection criteria as a function of the beam momentum are presented in Appendix C.

For 4 GeV and above, the algorithm for identifying the position of the first hard interaction in the AHCAL is used to separate muon from pion events. For muon events, no such interaction occurs. The algorithm described in Section 6.1 and [29] is applied to identify the clusters encompassing the first hard interactions. More than 4 hits and a minimum energy of 16 MIP in a single cluster are required. The muon contamination is reduced further by requiring more than 60 hits in the AHCAL for pion data from 8 GeV to 30 GeV. Below 4 GeV, the energy in the last AHCAL layers is suited to separate pion from muon events because the pion cascades do not extend over the full AHCAL depth. At 1 GeV, the energy in the last 10 layers has to be below 4 MIP and at 2 GeV the energy in the last 6 layers has to be below 3 MIP. The numbers of layers yielding the best separation between pions and muons at different beam momenta are extracted from digitized Monte Carlo simulations. Section 6.6 quantifies the bias of the AHCAL response to pions due to the event selection criteria based on the same detector.

Table II summarizes all negative pion data used for the analysis presented in this thesis. Figures 6.3(a) and 6.3(b) present the visible energy for 1 GeV and 10 GeV beam data before (open histograms) and after (filled histograms) applying the pion event selection criteria. Without applying the offline event selection, the highest peak at 1 GeV corresponds to muon events. The tail to higher energies originates from multi-particle events with one or

Table II
Pion data used for this analysis.

p_{beam} [GeV]	Events (selected)	Events (all)
1	2472	34289
2	39830	155217
4	74753	124794
6	92424	162705
8	55070	83457
10	65797	100942
12	112976	160753
20	64661	94366
30	51199	75302

more muons and pions reaching the AHCAL simultaneously. Applying the offline event selection for pions at this energy removes the muon peak and the tail due to multi-particle events. The remaining distribution is considered the AHCAL response to pions. At 10 GeV, the main peak before applying the offline event selection originates from pions and the additional peak at lower energies originates from single-muon events. As for the 1 GeV data, the additional peak and tail at higher energies is attributed to multi-particle events. The tail to low energies for 10 GeV data after applying the offline event selection for pions is caused by longitudinal leakage of a fraction of the pions.

6.5 Muon Selection

For collecting muon data, the coincidence between two $1 \times 1\,\text{m}^2$ scintillators is used as main trigger. A clean muon beam is generated by closing the beam dump so that only muons reach the CALICE calorimeters (see Section 3.1). In addition, muon events are collected with the $10 \times 10\,\text{cm}^2$ scintillator coincidence in-between pion data. For selecting single muon events, a track with 34-36 hits (i.e. 34-36 hits in a tower of 38 successive tiles), no hard interaction in the AHCAL, and less than 60 hits in total in the AHCAL are required. Because of the MIP detection efficiency of 94% and the AHCAL depth of 38 layers, muons yield a track with 35 hits on average. The tight cut on the track length with a lower and an upper limit reduces the fluctuations of the total AHCAL response to muons caused by different numbers of hits contributing (1 hit difference in track length changes the response by 3%). The upper limit on the total number of AHCAL hits excludes events with additional muons.

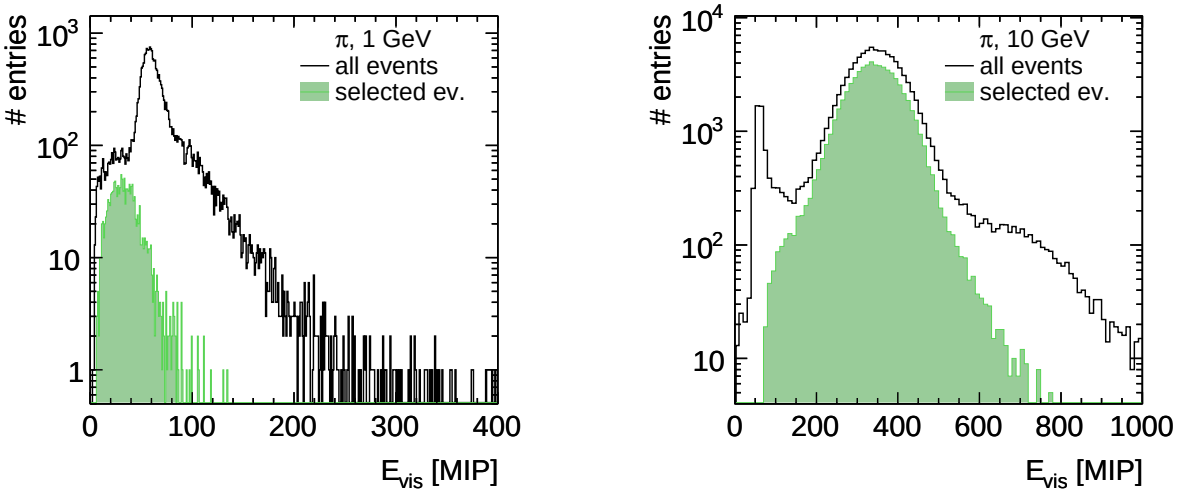

(a) (b)

Figure 6.3: Visible energy E_{vis} for pion measurements at 1 GeV (a) and 10 GeV (b) before (open histograms) and after (filled histograms) applying beam quality and pion selection criteria.

6.6 Event Selection Induced Systematic Uncertainties

Figure 6.4(a) shows the ratio of the mean visible energy from digitized Monte Carlo simulations after and before applying the AHCAL based event selection for electrons described in Section 6.3. The mean visible energy does not change after applying the cuts. Figure 6.4(b) shows the ratio for the mean visible pion energy from digitized Monte Carlo simulations (using the FTFP_BERT physics list) after and before applying the AHCAL based event selection for pions described in Section 6.4. At 2 GeV, the AHCAL based cuts reduce the mean visible energy by less than 1%, at 4 GeV the cuts shift the visible energy up by less than 1%. These shifts are accounted for by increasing the systematic uncertainty for the AHCAL response measured at these energies by 1%. At all other energies applying the cuts to does not introduce any bias to the observed detector response.

6.7 Data Purity

The differential Čerenkov detector is used during data collection to select only electron or pion events for recording. Because the purities of these selections are unknown, the pion contamination of the electron data and the electron contamination of the pion data need to be estimated with the AHCAL itself (no ECAL is installed during the measurements used for the analyses presented in this thesis).

At beam momenta above 10 GeV, electrons can be separated from pions via the correlation between the visible energy and the number of hits in the AHCAL. At lower beam momenta, the overlap of these distributions for the different particles increases significantly. Figure 6.5(a) shows this correlation for 20 GeV Monte Carlo simulations (using the FTFP_BERT physics list). The separability (one minus the overlap between two distributions which are normalized to an integral of one) of electrons from pions using these

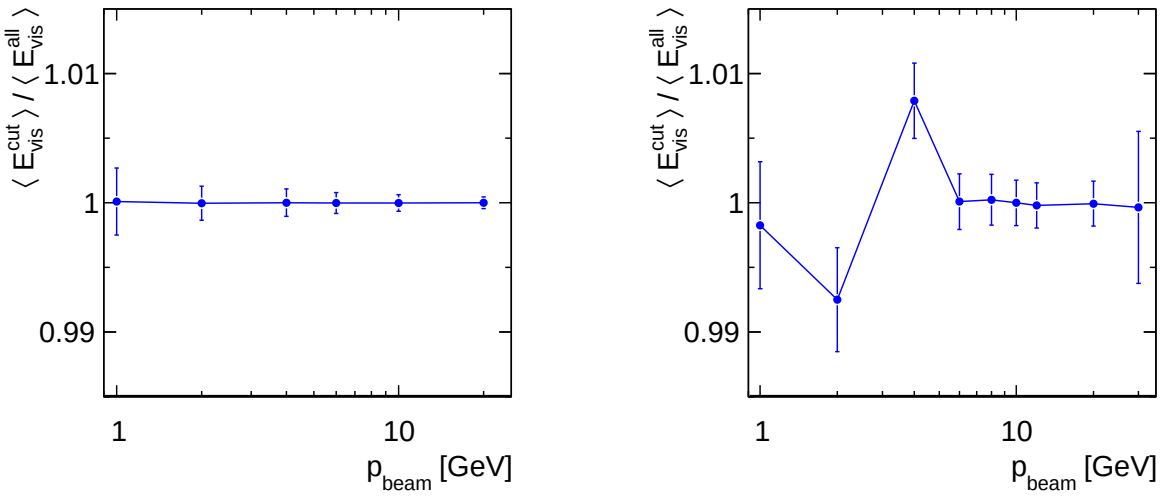

Figure 6.4: Ratio between the mean AHCAL response to simulated (a) electrons and (b) pions (using the FTFP_BERT physics list) after ($\langle E_{vis}^{cut} \rangle$) and before ($\langle E_{vis}^{all} \rangle$) applying the AHCAL based event selection criteria for the respective particle types presented in Sections 6.2, 6.3, and 6.4.

variables is better than 90%. At lower energies, the separation gets worse. Figure 6.5(b) shows the correlation between the visible energy and the number of hits for 4 GeV simulations. The separation of electrons from pions is less than 70%. At 1 GeV, the separation drops below 30%. An observable taking into account the different longitudinal shower shapes of electrons and pions (on average, electron cascades start earlier and are much shorter than pion cascades of the same energy) improves the separation of these particles at all beam momenta. Monte Carlo studies show that the energy fraction deposited in the first five layers of the AHCAL yields the best electron-pion separation at 1 GeV, i.e. the minimum overlap between the normalized distributions for electrons and pions. For higher beam momenta, the separation increases.

Figures 6.6(a) and 6.6(b) show the ratio of the energy deposited in the first five AHCAL layers divided by the total visible energy for electrons (blue) and pions (green) at 1 GeV for digitized Monte Carlo simulations. Points in Fig. 6.6(a) present electron data and points in Fig. 6.6(b) present pion data after applying the respective event selection criteria for electrons and pions. The red curves in both figures show the results of performing a fit of the weighted sum of the Monte Carlo distributions for both particle types to the data [86, 87]. The fit yields the best estimate for the relative contributions of the electron and pion Monte Carlo histograms to the data histogram. The weights extracted from the fit correspond to the electron and pion content of the data, assuming that residual contaminations with muons or multi-particle events are negligible. Figures 6.7(a) and 6.7(b) show the same distributions and the fit results at 4 GeV beam momentum. Due to differences in the predictions from different GEANT4 physics lists, the fits are performed with all physics lists used in this thesis (see Section 5.1.2). The center value of all resulting contaminations at a given beam momentum is used as best estimate for this contamination. Half the distance between the minimum and maximum predicted contamination is used as uncertainty on this estimate. According to the fits, the pion contamination of the electron data is less than

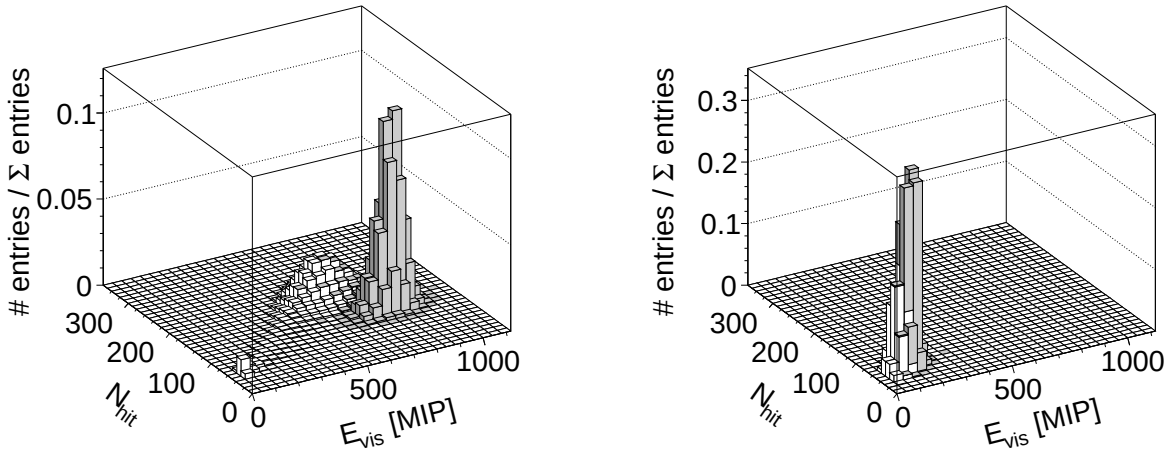

(a) (b)

Figure 6.5: Correlation between the visible energy E_{vis} and the number of hits N_{hit} for digitized electron (shaded histograms) and pion (open histograms) simulations at (a) 20 GeV and (b) 4 GeV beam momentum.

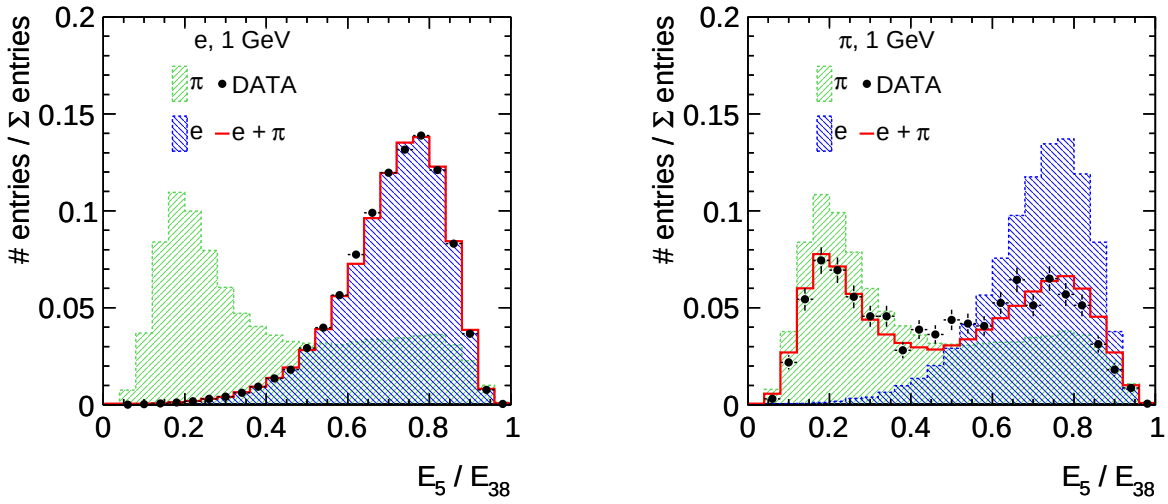

(a) (b)

Figure 6.6: Ratio between the visible energy in the first five AHCAL layers (E_5) and all 38 AHCAL layers (E_{38}) at 1 GeV beam momentum for pion (green) and electron (blue) simulations. Points represent (a) electron and (b) pion data. The red lines show the result of performing a fit of the weighted sum of the simulated electron and pion histograms on the data distributions.

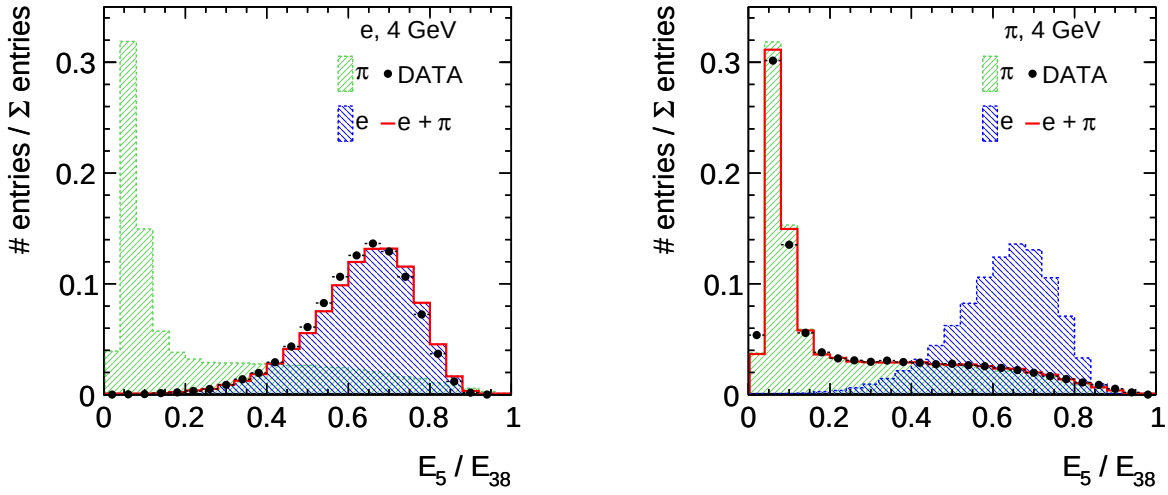

(a) (b)

Figure 6.7: Ratio between the visible energy in the first five AHCAL layers (E_5) and all 38 AHCAL layers (E_{38}) at 4 GeV beam momentum for pion (green) and electron (blue) simulations. Points represent (a) electron and (b) pion data. The red lines show the result of performing a fit of the weighted sum of the simulated electron and pion histograms on the data distributions.

TABLE III
ELECTRON CONTAMINATION OF PION DATA.

p_{beam} [GeV]	1	2	4	6	8 - 30
f_e [%]	28 ± 3	8 ± 3	5 ± 3	2 ± 2	1 ± 1

0.05% at all energies. Table III summarizes the electron contamination of the pion data. For beam momenta of 8 GeV and above, this contamination agrees with no contamination within uncertainties and is considered negligible. At 1 GeV, 2 GeV, 4 GeV, and 6 GeV, the electron contamination increases and needs to be accounted for.

The increase in electron contamination for lower beam momenta is attributed to two effects. First, the pion content in the beam drops for low beam momenta, while the electron and muon content increases. Second, the strategy for separating electrons from pions with the Čerenkov detector is different for low momenta than for high momenta. Between 8 GeV and 30 GeV pions are tagged, i.e. inefficiencies of the Čerenkov detector only affect the data acquisition rate for pions, but not the purity. Between 1 GeV and 6 GeV the Čerenkov generates a veto signal if light from electrons is detected. Therefore, inefficiencies of the Čerenkov detection efficiency add an electron contamination to the collected data. The strong increase in electron contamination at 1 GeV is attributed to a reduced electron detection efficiency of the Čerenkov detector due to the lower gas pressure used at this energy.

The fraction of energy deposited in the first five AHCAL layers cannot be applied to separate electrons from pions on an event by event basis. Cutting on this variable introduces a strong bias and distorts the visible energy distribution because all pions depositing their energy along a specific profile in the detector are rejected. Using more sophisticated

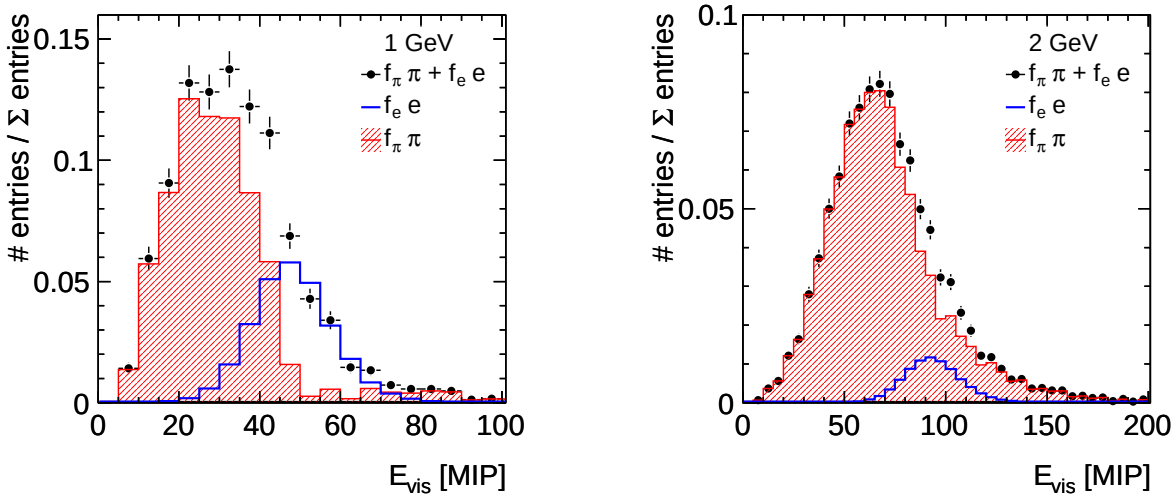

(a) (b)

Figure 6.8: Statistical subtraction of the contribution of the electron contamination to the visible pion energy E_{vis} for pion data collected at (a) 1 GeV and (b) 2 GeV beam momentum. Points represent pion data with electron contamination, the open histograms show electron data normalized to the contamination fractions from Table III, and the shaded histograms present the differences between these distributions.

event selection algorithms like multivariate analysis techniques could provide a way to separate electrons from pions on an event-by-event basis. However, knowing the amount of electron contamination of the pion data allows for statistically subtracting the electron contribution from all analyzed distributions.

Statistical Subtraction of Electron Contaminations

Figure 6.8(a) presents the visible energy for the full pion data sample at 1 GeV (points) and the visible energy for electrons (open histogram) weighted by the relative electron contamination from Table III. The shaded histogram ishows the difference between the other two histograms, which is the distribution for pions after subtracting the electron contribution and is used for further analysis. Figure 6.8(b) illustrates the same for 2 GeV data. This procedure is applied to the 4 GeV and 6 GeV pion data as well. The uncertainty of the electron fraction introduces a 1% uncertainty to the mean response at 1 GeV, 2 GeV, 4 GeV, and 6 GeV.

The AHCAL response to 2 GeV pions after contamination subtraction is asymmetric and shows a tail to higher responses. This tail is also visible for pions at higher beam momenta, but its contribution to the response distribution increases with decreasing beam momentum. Therefore, the AHCAL response to 1 GeV pions is expected to be asymmetric as well. The measured distribution of the 1 GeV response agrees with this expectation, but the tail disappears after subtracting the electron contamination. This hints to an overestimation of the electron content of the 1 GeV pion sample. The tail is attributed to the reduced number of energy depositions adding up to the total response at lower energies, which results in a clearer visibility of the Landau distribution of MIP-like energy

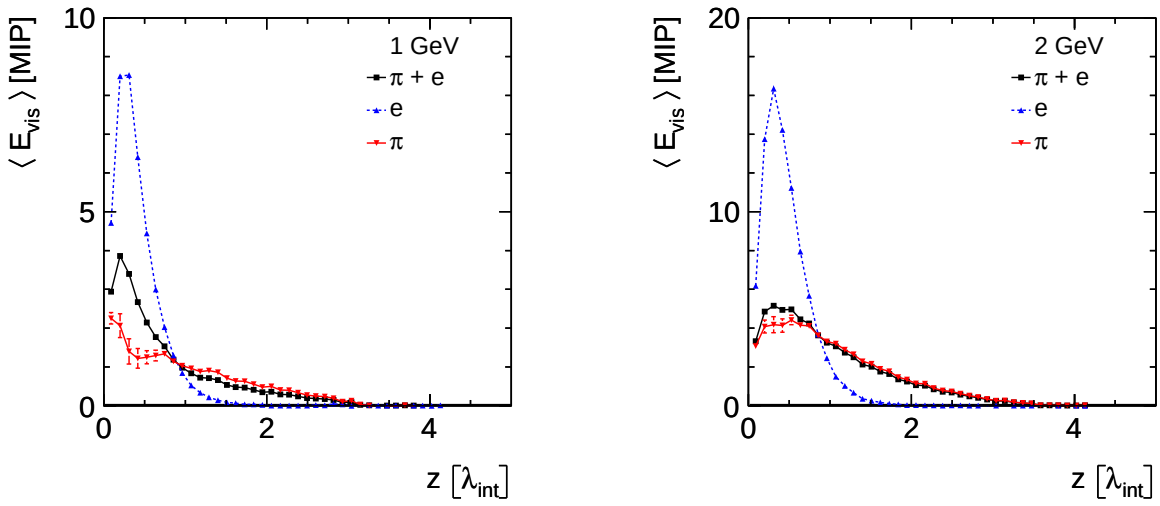

(a) (b)

Figure 6.9: Statistical subtraction of the contribution of the electron contamination to the longitudinal pion profiles, i.e. the mean AHCAL response $\langle E_{\text{vis}} \rangle$ to pions as a function of the calorimeter depth z, for pion data collected at (a) 1 GeV and (b) 2 GeV beam momentum. Squares represent the profiles for pion data with electron contamination, downwards-pointing triangles show the longitudinal profiles for electrons, and upwards-pointing triangles present the pion profiles after subtracting the electron contribution from each bin using Eq. (6.1).

depositions.

The pion analysis presented in this thesis covers several integral observables that are means of distributions, for example the mean energy per layer, the mean shower depth, or the mean shower radius. The statistical subtraction of the electron contamination for these observables is simplified using

$$\begin{aligned} \langle x^{\mathrm{e}+\pi} \rangle &= \frac{\Sigma_{\mathrm{i}} x_{\mathrm{i}}^{\mathrm{e}} + \Sigma_{\mathrm{j}} x_{\mathrm{j}}^{\pi}}{n_{\mathrm{e}} + n_{\pi}} \\ \langle x^{\pi} \rangle &= \frac{n_{\mathrm{e}} + n_{\pi}}{n_{\pi}} \cdot \left(\langle x^{\mathrm{e}+\pi} \rangle - \frac{n_{\mathrm{e}}}{n_{\mathrm{e}} + n_{\pi}} \cdot \langle x^{\mathrm{e}} \rangle \right), \end{aligned} \tag{6.1}$$

where $\langle x^{\pi+\mathrm{e}} \rangle$ is the mean of the distribution with n_{π} pion and n_{e} electron events, $\langle x^{\mathrm{e}} \rangle$ is the mean of the distribution for a pure electron sample, and $\langle x^{\pi} \rangle$ is the mean of the distribution for a pure pion sample. The uncertainty of $\langle x^{\pi} \rangle$ introduced by the error of determining n_{e} is estimated as half of the difference between the minimum and maximum resulting $\langle x^{\pi} \rangle$ when varying n_{e} within the error.

Points in Fig. 6.9(a) show the longitudinal shower profile in the AHCAL for 1 GeV pion data, i.e. the relation between the mean visible energy in a single depth bin (layer) and the longitudinal position of this bin in the AHCAL. The mean noise above threshold in each layer is subtracted from the mean visible energy in each layer. The blue markers show the measured electron profile. The red markers show the pion profile after subtracting the electron contamination from each bin using Eq. (6.9). The error bars take into account the uncertainty of the electron contamination. Figure 6.9(a) presents the same for 2 GeV

pions. The statistical subtraction of the contributions from the electron contamination is also applied for 4 GeV and 6 GeV data.

The 1 GeV pion profile after subtraction of the electron contamination shows a dip between 100 mm and 200 mm, whereas a smooth profile like for the 2 GeV pions is expected. This dip is attributed to a significant overestimation of the electron contamination. The reason for the overestimate of the electron contamination at 1 GeV is not utterly understood yet. Given the low statistics and the uncertainty of the purity, the 1 GeV pion data are dropped from the subsequent analysis. However, this section suggests that measuring the response and cascade profiles for 1 GeV pions with the AHCAL is possible if a clean pion sample is available or if the contaminations are better understood.

Chapter VII

Electron Analysis and Calibration Validation

The physics of electromagnetic cascades is less complex and better described by theory and Monte Carlo simulations than the physics of hadronic cascades. Thus, electron data provide a valuable basis for checking the understanding of a hadron calorimeter. The analysis of these data allows to test the reconstruction chain and the applied calibration factors. In addition, electron data are suitable for verifying the detector description in simulations and the implementation of detector features in the digitization.

A previous analysis of high-energy positron data collected with the AHCAL physics prototype (at CERN in 2007, positrons impinging directly on the AHCAL) covers the range from 10 GeV to 50 GeV beam momentum and is presented in [33] (beam energy and momentum are used interchangeably throughout this text). The analysis verifies the calibration procedure and establishes systematic calibration uncertainties. In addition, the electromagnetic scale (MIP/GeV scaling factor) and the detector performance in terms of response linearity and resolution are determined. Furthermore, the description of the AHCAL in simulations and the accurcy of the digitization are validated.

This chapter presents the analysis of low-energy electron data collected with the AHCAL physics prototype between 1 GeV and 20 GeV beam momentum (at the Fermilab Test Beam Facility in 2009, electrons impinging directly on the AHCAL). The experimental setup and the operating conditions are different than for the high-energy positron data and different calibration factors are applied to the two independent data sets. Nevertheless, the data allow for extending the previous studies to lower energies. Repeating part of the positron studies with the electron data is a crosscheck of the calibration factors obtained for the electron measurements and a verification of the understanding of both the detector and the simulations in this energy range. These steps are prerequisites for the analysis of pion data and the validation of pion simulations.

Section 7.1 establishes the electromagnetic scale and validates the linearity of the AHCAL response to electrons between 1 GeV and 20 GeV, while Section 7.2 presents the AHCAL resolution for single electrons and Section 7.3 evaluates the impact of using a non-native set of muon calibration factors for calibrating the data. Finally, Section 7.4 shows comparisons of the longitudinal shower profile for electrons in data and in simulations.

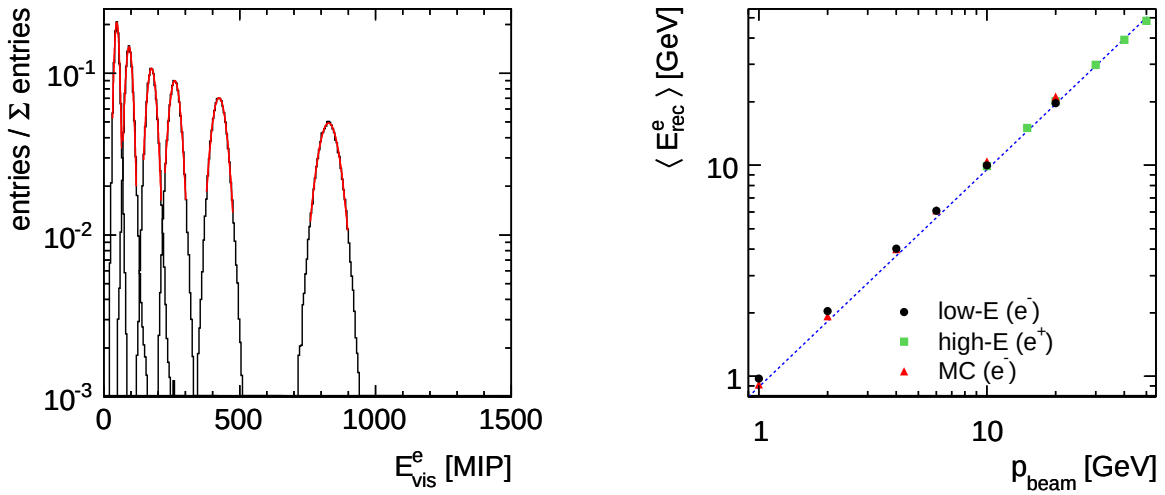

(a) (b)

Figure 7.1: (a) Measured visible energy E^e_{vis} for electron data at 1, 2, 4, 6, 10, and 20 GeV beam momentum (from left to right). The red lines are the results of Gaussian fits performed on the central 90% of the statistics at each beam momentum. (b) Mean reconstructed electron (positron) energy $\langle E^e_{\text{rec}} \rangle$ as a function of the beam momentum for low-energy data (circles), high-energy data (squares), and simulations (triangles). The error bars are smaller than the markers. The dashed line indicates a linear response ($\langle E^e_{\text{rec}} \rangle = p_{\text{beam}}$). See text for details about the conversion from the MIP scale to the GeV scale.

7.1 Linearity of the Electron Response

Figure 7.1(a) presents the measured visible energy E^e_{vis} (in units of MIP) for electrons at different beam momenta and Gaussian fits applied to the central 90% of the statistics. The restriction to a subrange of the statistics removes influences from tails of the visible energy distributions (see Section 6.3 for more details on these ditributions). The Gaussian functions describe the histograms well. From these fits, mean $\langle E^e_{\text{vis}} \rangle$ and sigma σ^e_{vis} of the visible energy for electrons are extracted.

The mean noise above threshold in the full AHCAL is about 7 MIP (at an average detector temperature of 24 °C) and corresponds to less than 1% of the signal at 20 GeV and 15% of the signal at 1 GeV. The noise contribution increases by 40% per 1 °C temperature increase (see Section 4.4). Thus, the noise introduces a temperature-dependent offset to the energy scale and has to be reduced in order to obtain a linear detector response. The approach followed by the previous analysis of high-energetic positron data is the definition of a fiducial volume which covers only part of the detector. Another option is to subtract the mean noise from the mean visible energy. The drawback of this second method is that the noise contribution to the signal width is not reduced. However, the advantage is that this method can be applied to pions as well where the definition of a fiducial volume covering all signal cells is more difficult than for electrons. For this analysis, the second option is chosen and $\langle E^e_{\text{vis}} \rangle_0$ is the mean visible energy extracted from the Gaussian fits in Fig. 7.1(a) after subtracting the mean noise. The noise is extracted from random trigger

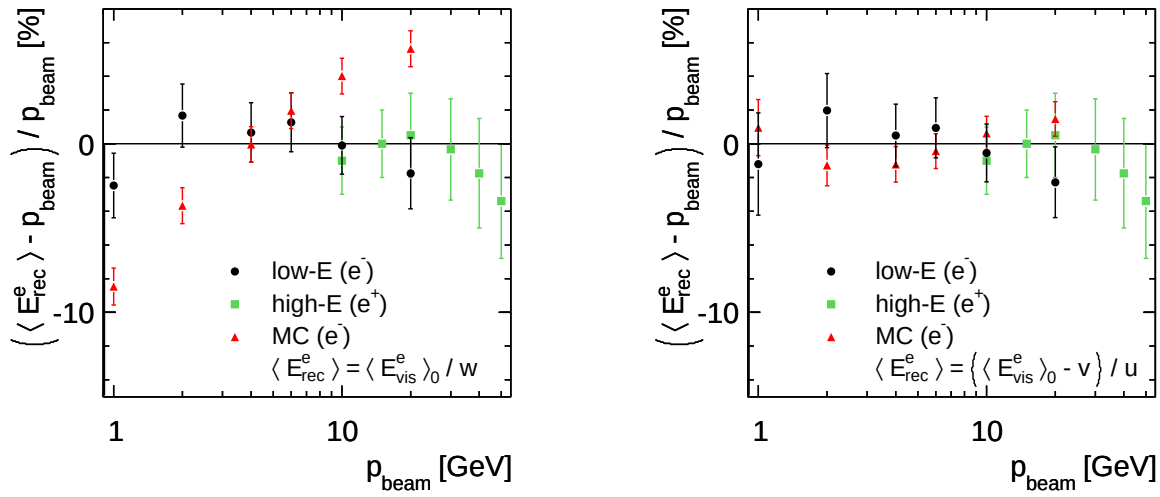

(a) (b)

Figure 7.2: Difference between the mean reconstructed energy $\langle E^e_{\text{rec}} \rangle$ and the true beam momentum p_{beam} as a function of p_{beam} using (a) a single weight w (according to Eq. (7.1)) or (b) a scaling factor u and an offset v (according to Eq. (7.2)) to convert visible energy to reconstructed energy for low-energy data (circles), high-energy data (squares), and simulations (triangles).

events collected in between beam events. A least-squares fit of

$$\langle E^e_{\text{vis}} \rangle_0 [\text{MIP}] = p_{\text{beam}} [\text{GeV}] \cdot w \left[\frac{\text{MIP}}{\text{GeV}} \right] \tag{7.1}$$

to the beam momentum dependence of $\langle E^e_{\text{vis}} \rangle_0$ from 1 GeV to 20 GeV yields a conversion factor w from MIP to GeV of $(41.7 \pm 0.3) \frac{\text{MIP}}{\text{GeV}}$. For the high-energy positron data, a factor of $(42.3 \pm 0.4) \frac{\text{MIP}}{\text{GeV}}$ is obtained. The results agree within errors. For simulations, a mean response uncertainty of 1% is assumed at all electron energies. A fit of Eq. (7.1) to the simulated electron response yields $w = (39.8 \pm 0.2) \frac{\text{MIP}}{\text{GeV}}$. The predictions from different GEANT4 physics lists (FTFP_BERT, FTFP_BIC, CHIPS and QBBC) agree within less than 1%. The agreement between these physics lists is expected because they all use the same model for electromagnetic physics. The small deviations are attributed to the different modelling of hadron physics which has a minor effect on the simulation of electromagnetic cascades via photo nuclear interactions like the giant dipole resonance mentioned in Section 1.1.1. The deviation of more than $3\,\sigma$ between the conversion factor from simulations and the value for electron data is discussed below.

Figure 7.1(b) presents the reconstructed energy ($\langle E^e_{\text{rec}} \rangle = \langle E^e_{\text{vis}} \rangle_0 / w$) from the low-energy electron measurements, from corresponding Monte Carlo simulations, and from high-energy positron measurements. The combined data sets cover the energy range from 1 GeV to 50 GeV. The dashed line indicates the equality between beam momentum and reconstructed energy. Figure 7.2(a) shows the deviation of the reconstructed energy from the beam momentum. The Fermilab data confirm the detector linearity for electrons down to 1 GeV. The simulations show a strong non-linear behavior of up to 10% at 1 GeV. The non-linearity of 1% for simulations between 10 GeV and 20 GeV is consistent with observations from previous measurements. The energies deposited by electromagnetic cascades

in the AHCAL scintillator layers extracted from raw Monte Carlo simulations (without any digitization steps applied) show a non-linear electron momentum dependence of up to 3% at 1 GeV. This non-linearity is attributed to the change in shower depth for electrons of different energies, i.e. the cascade reaches less scintillator layers and more energy is deposited in the first absorber layer at low energies. Thus, the non-linearity observed in the digitized simulations at low energies originates partially from the simulation itself and partially from the digitization procedure.

Using an alternative fit function

$$\langle E^{e}_{\mathrm{vis}} \rangle_0 = p_{\mathrm{beam}} \cdot u + v \tag{7.2}$$

for the relation between beam momentum and visible energy yields $u = (42.0 \pm 0.5)\,\frac{\mathrm{MIP}}{\mathrm{GeV}}$ and $v = (-0.8 \pm 1.0)\,\mathrm{MIP}$ for the electron data at low energies. Within uncertainties, the value for v is consistent with no offset. For simulations, $u = (41.7 \pm 0.3)\,\frac{\mathrm{MIP}}{\mathrm{GeV}}$ and $v = (-5.7 \pm 0.5)\,\mathrm{MIP}$ are obtained. The high-energetic positron results are $u = (42.4 \pm 0.6)\,\frac{\mathrm{MIP}}{\mathrm{GeV}}$ and $v = (-1.4 \pm 7.0)\,\mathrm{MIP}$. The negative offset is an effect of the 0.5 MIP threshold cut for the visible energy in each cell [33]. Uncertainties on the MIP scale definition or an inaccurate description of the inter-tile crosstalk in the digitization procedure would directly affect the cells that fall below this threshold and are removed from the detector response. Because in an electromagnetic cascades the signal cells below threshold are on the edge of the cascade, an inaccurate description of the lateral extension of electromagnetic cascades in the simulation would also contribute to this effect. Simulation studies show that the total visible energy in the AHCAL excluded by the 0.5 MIP threshold (for single energy depositions) increases with increasing beam momentum and therefore with increasing cascade extension. However, the fraction of visible energy below the 0.5 MIP thresold decreases with increasing electron energy.

Figure 7.2(a) shows the deviation from linearity of the reconstructed energy for the low-energy electron data, simulations, and the high-energy positron data taking the offset v into account. With this offset, the linearity for simulations improves considerably and is within 2% between 1 GeV and 20 GeV. Within uncertainties, the linearity for data does not change. The results for low-energy electron data agree with the results from simulations within uncertainties.

Figures 7.3(a) and 7.3(b) compare the reconstructed energy from electron measurements to Monte Carlo simulations (using the QGSP_BERT physics list from GEANT4, version 9.4) for 10 GeV and 2 GeV beam momentum and Gaussian fits applied to the histograms. At 10 GeV, the agreement between data and simulation is satisfactory. For lower energies, the simulations predict a systematically smaller width (which is reflected in an underestimation of the energy resolution, see Section 7.2). Figure 7.4(a) presents the ratio between the mean electron response for data and digitized simulations. Figure 7.4(b) presents the same ratio after subtracting the mean noise from each measurements and taking the offsets v in data and simulations into account. With these corrections, electron data and simulations agree at the 4% level between 1 GeV and 20 GeV at the MIP scale. This comparison for electrons at the MIP scale gives an estimate of the overall precision for comparisons between pion data and simulations at the MIP scale with the given status of calibration, simulation, and digitization procedures. Thus, only deviations between data and simulations of more than 4% are significant.

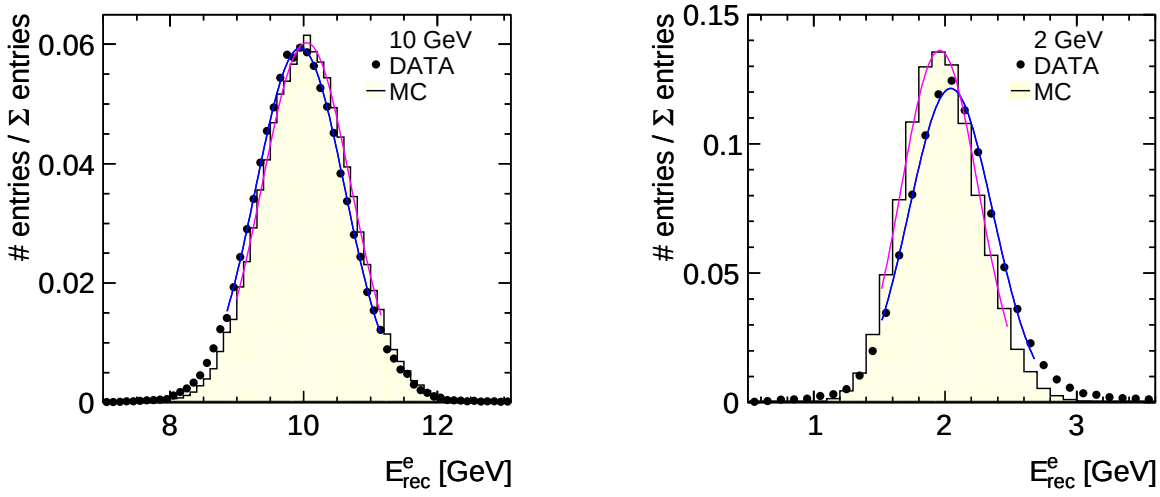

(a) (b)

Figure 7.3: Reconstructed energy E^e_{rec} for electrons from data (points) and simulations (histograms) at (a) 10 GeV and (b) 2 GeV beam momentum. See text for details about the conversion from the MIP scale to the GeV scale. The results of Gaussian fits performed no the central 90% of the statistics of the respective distributions are presented as lines.

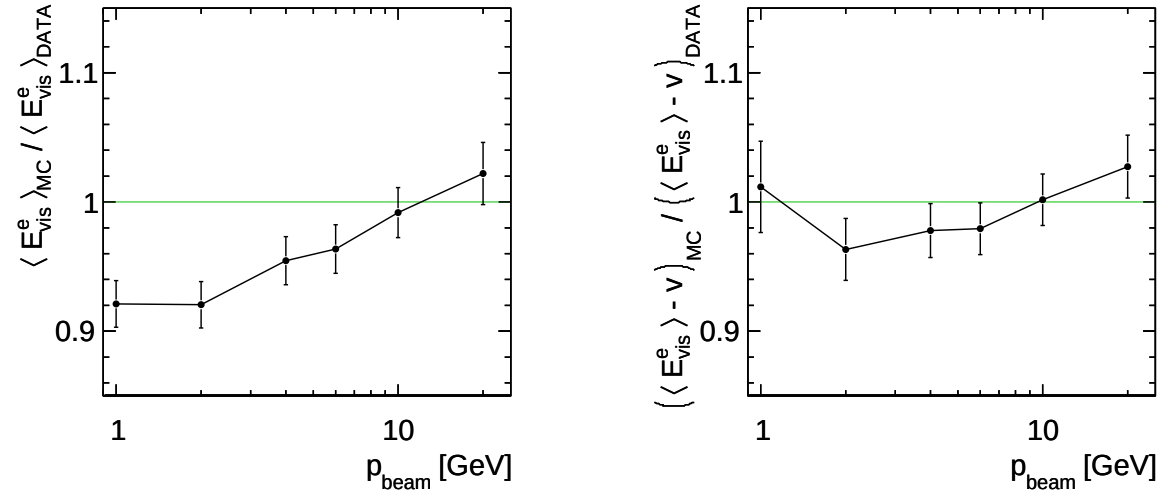

(a) (b)

Figure 7.4: Ratio between the mean visible energy $E^{\text{MC}}_{\text{vis}}$ (in MIP) from simulations (using the QGSP_BERT physics list) and $E^{\text{DATA}}_{\text{vis}}$ from data (a) before and (b) after subtracting the respective offsets v. The error bars take into account statistical uncertainties (negligible), calibration uncertainties for data (2-3%), and the systematic uncertainty of the response predicted by simulations (1%).

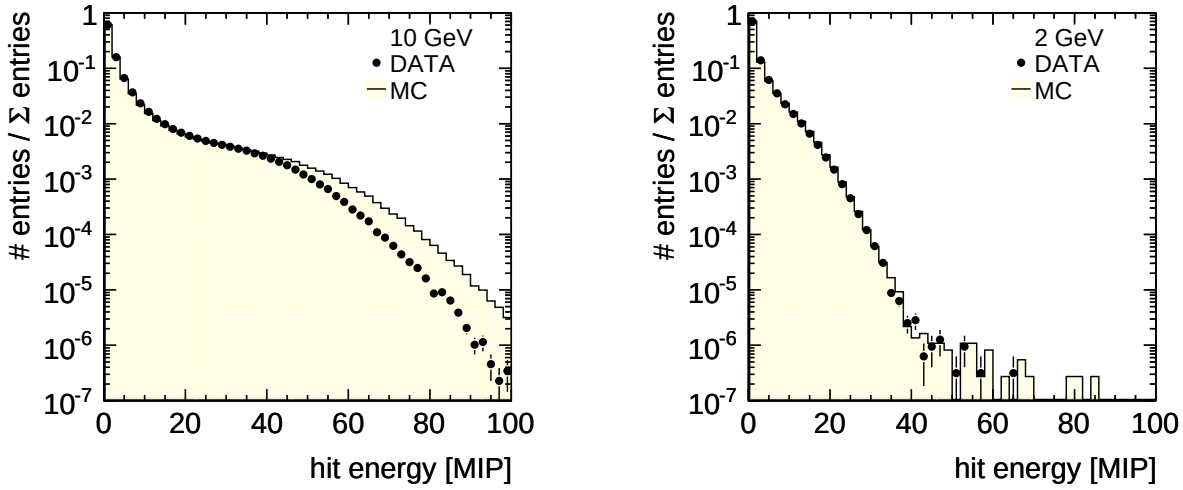

(a) (b)

Figure 7.5: Visible energy in single AHCAL cells for electrons from data (points) and simulations (histograms) at (a) 10 GeV and (b) 2 GeV beam momentum.

Figures 7.5(a) and 7.5(b) show the distributions of the visible energy detected in single AHCAL cells for 10 GeV and 2 GeV electron data (points) and the predictions from digitized simulations (filled histogram). At 10 GeV, the simulations predict more high energetic signals than observed in data. The deformation in the data distribution is a remaining effect of the SiPM saturation, whereas simulations are not affected by saturation because the same SiPM respone functions are used to simulate the non-linear SiPM response in the digitization procedure and to correct it during calibration. Since the energy density in a 10 GeV electron shower is higher than in a 2 GeV cascade, saturation effects play a higher role at the higher momentum. At 2 GeV, the hit energy spectra from data and simulations agree well. No remaining effect from the SiPM non-linearity is visible. The effect of an imperfect saturation correction affects pion energy measurements much less than energy measurements for electrons because the energy density in pion cascades is on average much lower than the density in electron cascades of the same energy.

7.2 Energy Resolution for Electrons

Figure 7.6 shows the detector resolution $\frac{\sigma_e}{E_e}$ for electrons at different beam momenta in data and in simulations. The resolution is the width of the visible energy divided by the visible energy after subtracting the mean detector noise and taking the offsets from the linearity fit in Section 7.1 into account $\left(\frac{\sigma_e}{E_e} = \frac{\sigma^e_{vis}}{\langle E^e_{\mathrm{vis}}\rangle_0 - v}\right)$. Results for positron measurements obtained at higher beam momenta are depicted as well. As discussed in Section 1.2, the energy resolution of a calorimeter can be described by Eq. (1.7). Estimating the noise term c from random trigger events yields $c = 40$ MeV. This estimate assumes an increase of the signal width due to noise with $\sqrt{N}$, where N is the number of cells contributing to the signal. Without threshold cut, the standard deviation of the visible energy in the full AHCAL (about 7400 cells) for random trigger events is about 12 MIP. For a single

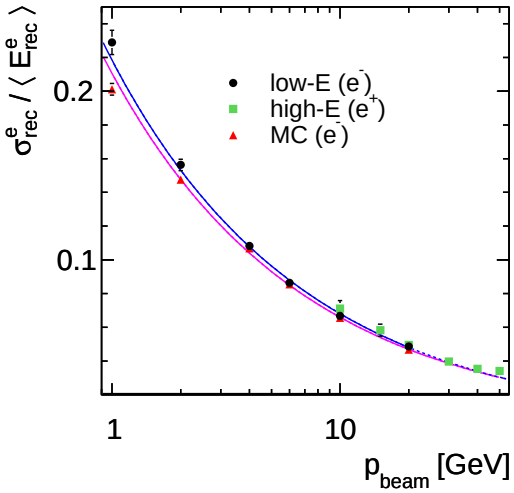

Figure 7.6: AHCAL resolution $\sigma^e_{\mathrm{rec}}/\langle E^e_{\mathrm{rec}}\rangle$ as a function of the beam momentum p_{beam} for low-energy electron data (circles), high-energy positron data (squares), and electron simulations (triangles). The solid lines present the results of performing fits of Eq. (1.7) on the resultions extracted for electron data and simulations and the dashed lines indicate the extensions of these fits results to higher beam momenta.

layer (about 200 cells), the standard deviation of this distribution is 2 MIP. These numbers support the assumption of a $\sqrt{N}$ dependence of the noise contribution to the AHCAL resolution. Roughly 150 cells contribute to the AHCAL response to a 20 GeV electron. Applying a 42.0 MIP/GeV scaling factor results in a noise term of about 40 MeV.

The solid lines in Fig. 7.6 present the results of performing a fit of Eq. (1.7) to the electron data and simulations (1 GeV to 20 GeV, fixing $c = 40$ MeV). The dashed lines are the extensions of the fit results to higher energies. Table I summarizes the fit parameters and their uncertainties for the low-energy electron data, the high-energy positron data [33], and simulations. Varying the fixed noise term from $c = 0$ MeV to $c = 70$ MeV only changes the results of the remaining fit parameters within their errors. A combined fit to the data from both energy ranges yields compatible values. The results agree within their uncertainties. Data and simulations yield calibration terms b that agree within 1σ. The stochastic term a obtained from simulations is smaller than a for data, but the deviation is less than 3σ. The fit result is shown in Fig. 7.6 as a dashed line. The electron simulation tends to underestimate the width of the electron response at low energies. This result is sensitive to the offset v needed to achieve a linear detector response. Matching the offsets in data and simulations by future advancements of the digitisation procedure is expected to improve the agreement of the resolution at low energies as well.

7.3 Applying Non-native Muon Calibration Factors

The AHCAL data can be calibrated using native or non-native sets of muon calibration factors. Non-native calibration factors are extracted with different experimental setups under different operating conditions than the data they are applied to. The portability of muon calibration factors is discussed in Section 4.2. Performing a fit of Eq. (7.1) to the

TABLE I
AHCAL ELECTRON / POSITRON RESOLUTION.

Parameter	Low-energy data (e^-)	High-energy data (e^+)	Simulations (e^-)
a	$(21.5 \pm 0.2)\%$	$(21.9 \pm 1.4)\%$	$(20.7 \pm 0.2)\%$
b	$(0.0 \pm 1.2)\%$	$(1.0 \pm 1.0)\%$	$(0.8 \pm 0.4)\%$
c	40 MeV	58 MeV	40 MeV

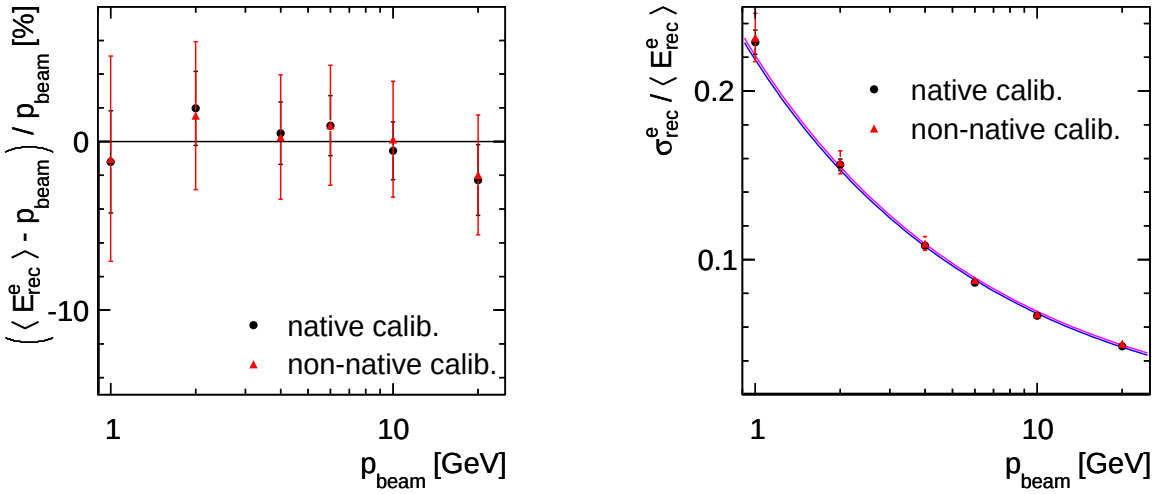

(a) (b)

Figure 7.7: (a) Difference between the mean reconstructed energy $\langle E^e_{\text{rec}} \rangle$ and the true beam momentum p_{beam} as a function of p_{beam} (using a scaling factor u and an offset v according to Eq. (7.2)) for electron data applying the native (points) or the non-native (triangles) set of muon calibration factors. (b) AHCAL resolution $\sigma^e_{\text{rec}}/\langle E^e_{\text{rec}} \rangle$ as a function of the beam momentum p_{beam} for electron data applying the native (points) or the non-native (triangles) set of muon calibration factors. The solid lines present the results of performing fits of Eq. (1.7) on the measured resultions.

electron response calibrated with a non-native calibration set yields a MIP/GeV conversion factor of $w = (40.3 \pm 0.6)\,\frac{\text{MIP}}{\text{GeV}}$. Using Eq. (7.2) for the fit yields $u = (40.5 \pm 0.8)\,\frac{\text{MIP}}{\text{GeV}}$ and $v = (-0.5 \pm 1.9)\,\text{MIP}$. Figure 7.7(a) compares the residuals to linearity with the native and the non-native muon calibration factors. Within errors, both calibration sets yield agreeing linearities. Figure 7.7(b) presents the comparison of the resolution with both calibration sets. The stochastic term for the non-native calibration is $(21.7 \pm 0.6)\%$, the constant term is $(0.9 \pm 1.5)\%$. Within errors, these numbers agree with the fit results for the low-energy electron data calibrated with the native calibration from table I. Both the linearity and the resolution of the AHCAL response to electrons agree within uncertainties when using a native or a non-native set of muon calibration factors.

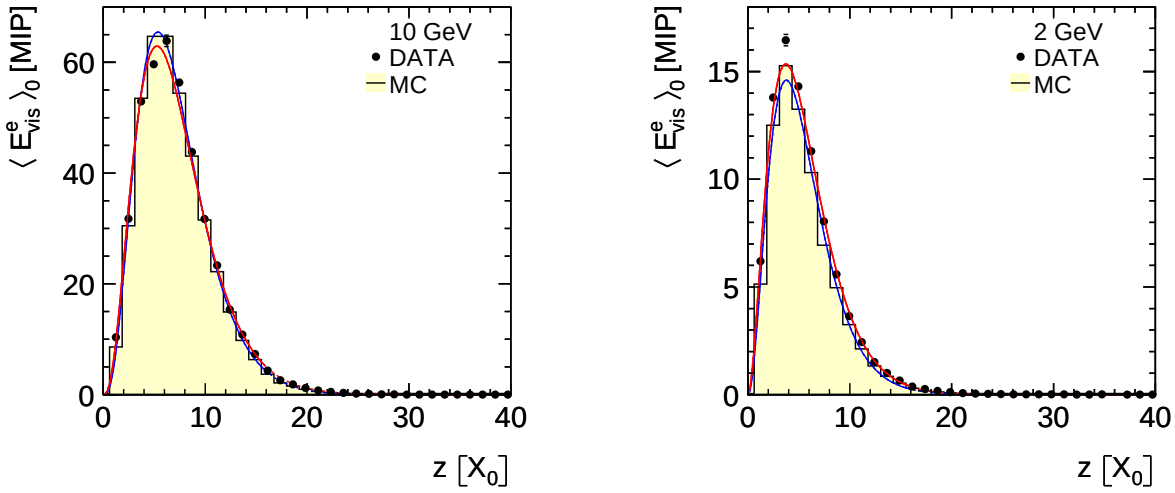

(a) (b)

Figure 7.8: Longitudinal shower profiles, i.e. the mean visible energy $\langle E^e_{\text{vis}} \rangle_0$ (after subtracting the mean noise for each layer) as a function of the AHCAL depth z, for (a) 10 GeV and (b) 2 GeV electrons. Points represent data and the filled histograms show the predictions from simulations. The solid lines present the results of performing fits of Eq. (7.3) to the profiles between zero and 16 X_0 (red for data, blue for simulations) and the dashed lines are the extensions of the fit results to the end of the calorimeter.

7.4 Longitudinal Electron Cascade Profiles

Figures 7.8(a) and 7.8(b) present the longitudinal shower profile for 10 GeV and 2 GeV electrons. The y-axis is the mean energy deposited in a given x-bin minus the mean noise for this bin, the x-axis is the shower depth in the AHCAL in units of radiation lengths. The AHCAL correspond to 47.16 X_0 and a common depth of 47.16/38 X_0 is assigned to each layer. The offset of 0.11 X_0 between the center of a scintillator layer and the end of a cassette is not taken into account. The variation of the thicknesses of the absorber plates (of up to 3% [31]) are not taken into account either. The points in Fig. 7.8(a) and 7.8(b) are data, the histogram shows the prediction from simulations. Data and simulations agree well. The function

$$f(t) = \frac{\mathrm{d}E}{\mathrm{d}t} = at^{\omega} \cdot e^{-bt} \tag{7.3}$$

parametrizes the longitudinal shower profiles for electrons, where E is the deposited energy, t is the calorimeter depth, a is a normalization factor, and ω and b describe the profile shape [9]. The fits of this function to the profiles in Fig. 7.8(a) and Fig. 7.8(b) result in the red (data) and blue (simulations) curves. The fit range covers only the first third of the AHCAL (from 0 to 16 X_0) because electrons deposit most of their energy in this volume.

From the fits, the position of the shower maximum is extracted via $t_{\max} = \omega/b$. Figure 7.9 shows the shower maxima for low-energetic electrons at different beam momenta (circles) and results from positron measurements at high energies (squares, values corrected for a a systematic upwards shift of 0.5 X_0 resulting from a wrong calculation of the AHCAL depth in X_0 in [33]). The material in the beam line in front of the AHCAL

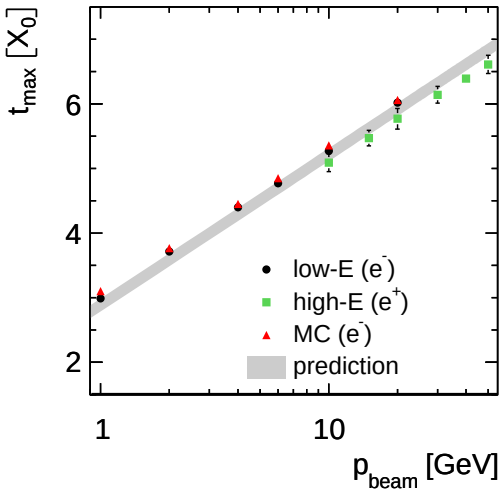

Figure 7.9: The depth $t_{\max}$ of the shower maximum as a function of the beam momentum p_{beam} for data (circles are electron measurements at low energies, squares are positron measurements at high energies) and simulations (triangles). The band illustrates the prediction from Eq. (7.4) with the band widths reflecting a 10% uncertainty of the used estimate for ϵ_c.

(about $0.14\,X_0$ for the low-energy electron data, see Sections 3.1 and 3.2, and $0.28\,X_0$ for the high-energy positron data, [47]) is not taken into account. Figure 7.9 presents the values after subtracting this offset. The low-energy electron results agree with the previous high-energy positron results within uncertainties. The shift of $0.1\,X_0$ between the low-energy data and the high-energy data in the overlap region is of the same order as the difference in the beam line material budget between the different experimental setups. The values extracted from electron simulations are presented as triangles and agree with data.

Different parametrizations of the position of the shower maximum for electrons exist. An empirical parametrization based on 'Approximation B' and validated with data [88] predicts

$$t_{\max} = \left[1.01 \cdot \ln \frac{E}{\epsilon_c} - 1.0\right], \tag{7.4}$$

where E is the electron energy and ϵ_c is the critical energy, which is about 21.04 MeV for iron [9]. The prediction from Eq. (7.4) is indicated in Fig. 7.9 as shaded area. The widths of this band reflect an uncertainty of about 10% on ϵ_c. The shower maxima $t_{\max}$ extracted from the AHCAL data and GEANT4 simulations follow this parametrization.

7.5 Summary

The electron data collected with the AHCAL physics prototype at low energies cover the range from 1 GeV to 20 GeV. The analysis of these data yields a MIP/GeV conversion factor of $w = (41.7 \pm 0.3)\,\frac{\text{MIP}}{\text{GeV}}$ (no offset allowed) or $u = (42.0 \pm 0.5)\,\frac{\text{MIP}}{\text{GeV}}$ and $v = (-0.8 \pm 1.0)$ MIP. Within uncertainties, the linearity of the AHCAL in the covered energy range is confirmed. The resolution extracted from these data has a stochastic term of $(21.5 \pm 0.2)\,\%/\sqrt{E[GeV]}$ and a constant term of $(0.0 \pm 1.2)\%$. All these results agree with the results obtained from the high-energy positron data recorded between 10 GeV and 50 GeV beam momentum.

The visible energies predicted by Monte Carlo simulations show a larger negative offset than observed in data. This offset with respect to data hints to an inaccurate description of detector effects in the simulation that needs further investigation. The results for the maximum longitudinal shower position for data and simulations in the range from 1 GeV to 20 GeV agree within uncertainties. The results obtained from low-energy electrons are consistent with the results from the high-energy positron data. The analysis presented in this chapter shows that the detector calibration and simulation are well enough under control to analyze pion data and to validate pion simulations.

Calibrating the low-energy electron data with a non-native set of muon calibration factors does not affect the detector linearity and resolution. This confirms the portability of the AHCAL muon calibration to different experimental setups and operating conditions discussed in Section 4.2.

Chapter VIII

Pion Analysis

Most GEANT4 models for hadron physics are either applicable at high energies (string models) or at low energies (cascade models) and GEANT4 provides physics lists combining two or more models valid at different energies. The transition between the use of different models occurs at energies between 4 GeV and 25 GeV, where the exact range of application of the respective models depends on the physics list. Furthermore, the electromagnetic component of hadron showers decreases with decreasing energy and the features of the hadronic component are more pronounced. Therefore, low energies are particularly interesting for validating GEANT4 simulations of hadron showers. Moreover, most hadrons in jets from hadronic decays of e.g. Z^0 bosons have energies below 10 GeV, which makes analyzing low-energetic hadrons also very important for the development of calorimeters for an ILD-like detector at the ILC and Particle Flow algorithms.

This chapter presents the analysis of low-energetic pion data collected with the AHCAL physics prototype at Fermilab (no ECAL installed) and the validation of several GEANT4 physics list between 2 GeV and 30 GeV. As discussed in Section 6.7, the pion measurements at 1 GeV are excluded because of the uncertainties about the electron contamination. Nevertheless, simulations of 1 GeV pions are included to illustrate the trends of the Monte Carlo predictions. The contributions from the electron contamination are subtracted statistically from all presented distributions and observables for 2, 4, and 6 GeV pion data. The comparisons between data and simulations cover the total deposited energy (Section 8.1) and the longitudinal (Section 8.2) and radial (Section 8.3) shapes of pion cascades. The measurements of the respective observables are compared to previous results in the range of momentum overlap. This previous analysis is based on high-energetic pion data collected at beam momenta from 8 GeV to 80 GeV (with a different experimental setup and under different operating conditions) and is presented in [30].

Calorimeters measure the total particle energy E. For measurements at test-beam facilities and for the simulations presented in this chapter, pion energies E^π are selected by choosing the beam momentum p_{beam}. The pion energy is the sum of kinetic energy and mass m, i.e. $E^\pi = \sqrt{p_{\text{beam}}^2 + m^2}$. With $m = 139\,\text{MeV}$, the difference between E^π and p_{beam} is below 1% for pions of 1 GeV momentum and above. This difference is only important when quantifying the energy dependences of observables like the $\frac{\pi}{e}$ ratio discussed in Section 8.1, whereas momentum and energy can be used interchangeably for direct comparisons of data and simulations.

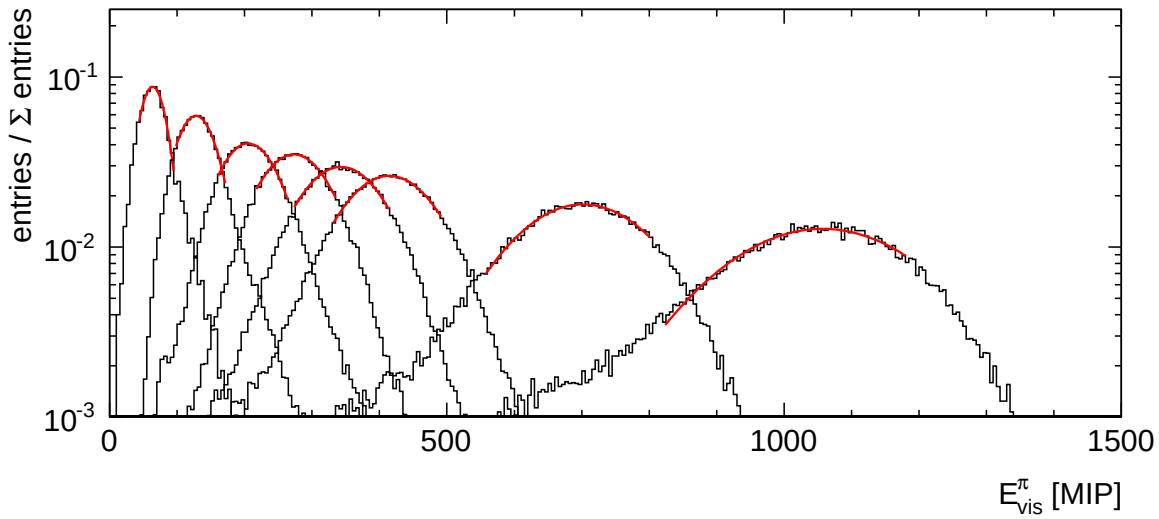

Figure 8.1: Measured visible energy E^{π}_{vis} for pion data at 2, 4, 6, 8, 10, 12, 20 and 30 GeV beam momentum (from left to right). The red lines are the results of Gaussian fits performed to the central 70% of the statistics at each beam momentum.

8.1 Energy Measurement

Figure 8.1 shows the visible energy E^{π}_{vis} for negative pion data recorded at beam momenta between 2 GeV and 30 GeV. The red lines indicate the results of performing Gaussian fits to the central 70% of the statistics to extract the most probable visible energy in the AHCAL, which is taken as the mean visible energy $\langle E^{\pi}_{\text{vis}} \rangle$ for pions fully contained in the detector. Restricting the fit range excludes the tails of the distributions (discussed in Section 6.4). The tails to the left increase with higher beam momenta due to an increased fraction of pion cascades extending beyond the end of the AHCAL in longitudinal direction. In the current analysis, no attempt to recover the leaking energy is made [89].

The mean noise above threshold is subtracted from $\langle E^{\pi}_{\text{vis}} \rangle$. The differences $\langle E^{\pi}_{\text{vis}} \rangle_0$ are converted from the MIP scale to the electromagnetic GeV scale via $\langle E^{\pi}_{\text{rec}} \rangle = (\langle E^{\pi}_{\text{vis}} \rangle_0 - v)\,/u$, where $v = (-0.8 \pm 1.0)$ MIP is the offset of the electromagnetic scale and $u = (42.0 \pm 0.5)\,\frac{\text{MIP}}{\text{GeV}}$ is the electromagnetic conversion factor (see Chapter 7). Figure 8.2 shows the reconstructed pion energy at the electromagnetic scale divided by the total available pion energy E^{π}_{tot} for different energies, i.e. the $\frac{\pi}{e}$ ratio. Due to the energy dependence of the electromagnetic fraction in hadron cascades and the non-compensating nature of the AHCAL, a non-linear detector response to pions is expected. Performing a fit of Eq. (1.6) to the measurements in Fig. 8.2 fixing $E_0 = 1.0$ GeV describes the energy dependence observed in data within uncertainties and yields $k = (0.72 \pm 0.03)$ and $\frac{e}{h} = (1.6 \pm 0.1)$. These values are of the same order of magnitude as results obtained with the ATLAS scintillator-steel tile calorimeter in test-beam measurements (at pion energies from 10 GeV to 300 GeV), which yield $\frac{e}{h} = (1.33 \pm 0.06 \pm 0.02)$ and $k = (0.85 \pm 0.03 \pm 0.01)$ [76]. The deviations between the numbers for the AHCAL physics prototype and the ATLAS tile calorimeter are attributed to the different sampling fractions of the detectors. Nevertheless, the AHCAL result illustrates the sensibleness of the measured pion responses and the assigned calibration uncertainties.

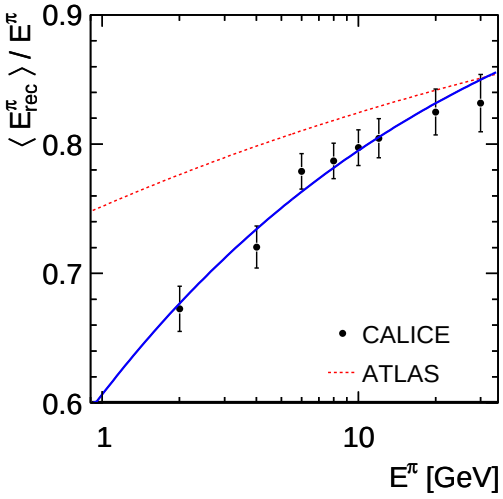

Figure 8.2: Ratio between the mean reconstructed pion energy $\langle E^{\pi}_{\mathrm{rec}} \rangle$ (calibrated to the electromagnetic scale) and the pion energy E^{π} as a function of the pion energy. The solid line shows the result of performing a fit of Eq. (1.6) to the AHCAL measurements and the dashed line indicates results from the ATLAS tile calorimeter [76]. The respective parameters are given in the text.

Applying Non-native Muon Calibration Factors

As discussed in Sections 4.2 and 7.3, the AHCAL data can be calibrated using native or non-native sets of muon calibration factors, where non-native calibration factors are extracted with different experimental setups under different operating conditions than the data they are applied to. Figure 8.3(a) presents the mean measured pion response applying native and non-native muon calibration factors as a function of the beam momentum. The MIP/GeV conversion factor for the non-native calibration is $u = (40.5 \pm 0.8)\,\frac{\mathrm{MIP}}{\mathrm{GeV}}$ with an offset of $v = (-0.5 \pm 1.9)\,\mathrm{MIP}$. The deviations of the two sets of muon calibration factors observed in Section 4.2 are absorbed by the MIP/GeV conversion factors, i.e. after absolute calibration to the GeV scale, the measured pion response is not affected by the use of non-native instead of native muon calibration factors.

Comparison to Previous Energy Measurements

Figure 8.3(b) shows the mean measured pion response (without performing any fit) and results from previous measurements as a function of the pion momentum. For comparability reasons, the containment cut used for the previous analysis of the high-energetic data, which requires the first inelastic pion-nucleus scattering to occur in the first five AHCAL layers, is applied to the low-energetic data as well. The previous results are calibrated to the electromagnetic scale using $v = (-1.4 \pm 7.0)\,\mathrm{MIP}$ and $u = (42.4 \pm 0.6)\,\frac{\mathrm{MIP}}{\mathrm{GeV}}$ from [33], which are measured at the same operating conditions as the pion responses. The previously measured pion energies are systematically shifted by about 5% to smaller values. The displayed errors include the calibration uncertainties of both data sets on the MIP scale, but not the uncertainties from the conversion to the GeV scale, which adds another 2% to the uncertainty of the ratios. Taking this additional uncertainty into account, the measurements from both periods agree within errors. Because of the uncertainty of the

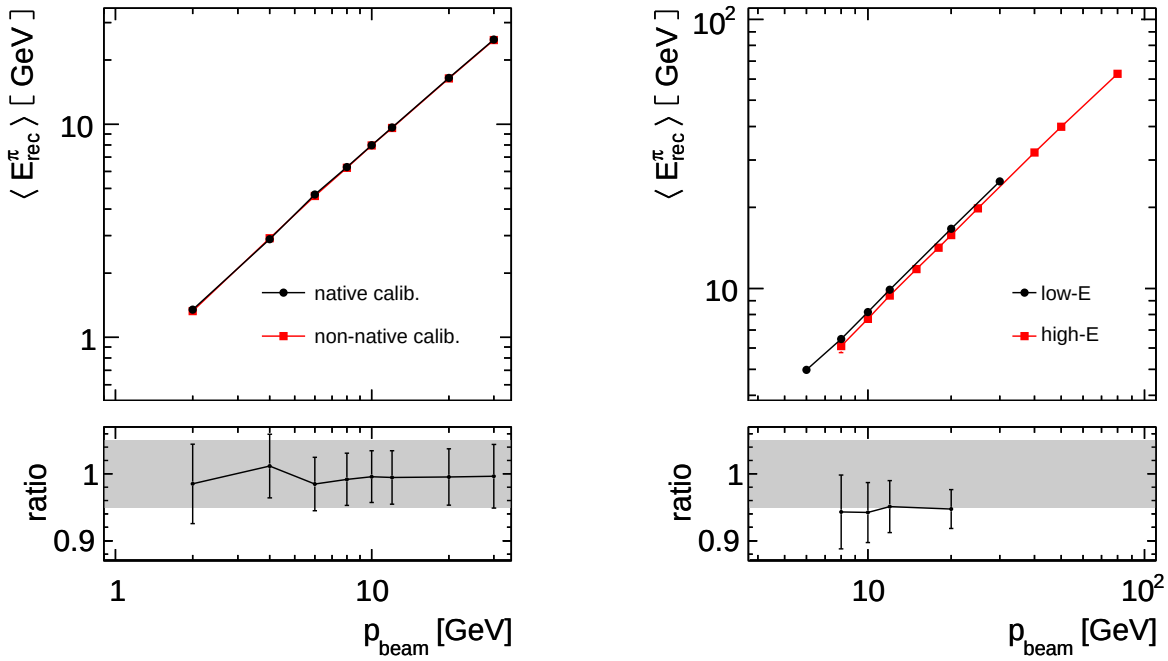

(a) (b)

Figure 8.3: (a) Mean reconstructed energy for low-energetic pion data calibrated using either native or the non-native muon calibration factors. See text for details about the conversion from the MIP scale to the (electromagnetic) GeV scale. (b) Mean reconstructed energy $\langle E^{\pi}_{\mathrm{rec}} \rangle$ for pion data collected at low pion momenta (low-E) and high pion momenta (high-E, from [30]) and the ratios between the results from the high-E and the low-E measurements at the beam momenta covered by both data sets. The gray band indicates the range of 5% agreement.

energy scale illustrated by this comparison, only detector response deviations between data and simulations of 5% or more are considered significant with the current knowledge about the absolute AHCAL calibration.

Validation of GEANT4 Simulations

Figures 8.4(a) and 8.4(b) present the AHCAL response to 2 GeV pions calibrated to the electromagnetic scale for data (points) and digitized Monte Carlo simulations using the Bertini cascade model (in FTFP_BERT) and the binary cascade model (in FTF_BIC). For simulations, the results from Chapter 7 for the offset of the electromagnetic scale of $v = (-5.0 \pm 0.5)$ MIP and the conversion factor of $u = (41.7 \pm 0.3)\,\frac{\mathrm{MIP}}{\mathrm{GeV}}$ in simulations are applied.

Figures 8.5(a) and 8.5(b) show the most probable AHCAL response (from the Gaussian fits) to pions of different momenta for data and Monte Carlo simulations using different GEANT4 physics lists. The ratios between simulation predictions and data are shown below the figures with a gray band indicating the range of 5% agreement. The visible energies predicted by the FTFP_BERT physics list agree best with data (within 5%) over the covered pion momentum range from 2 GeV to 30 GeV.

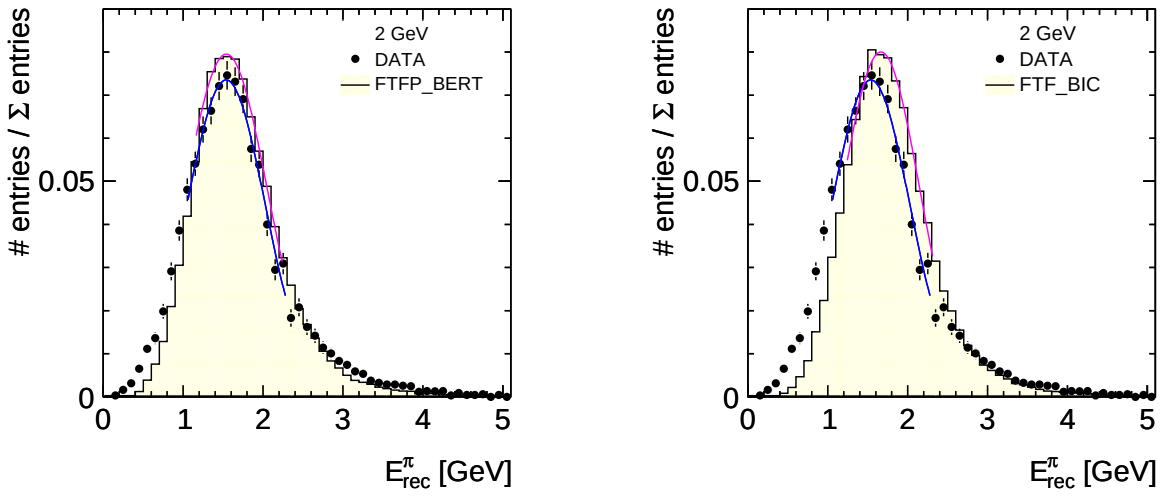

(a) (b)

Figure 8.4: Reconstructed energy E^{π}_{rec} for 2 GeV pions from data (points) and Monte Carlo simulations (histograms) using (a) the Bertini cascade model (FTFP_BERT physics list) and (b) the binary cascade model (FTF_BIC physics list). See text for details about the conversion from the MIP scale to the (electromagnetic) GeV scale. The results of Gaussian fits performed to the central 70% of the statistics of the respective distributions are presented as lines (red and blue).

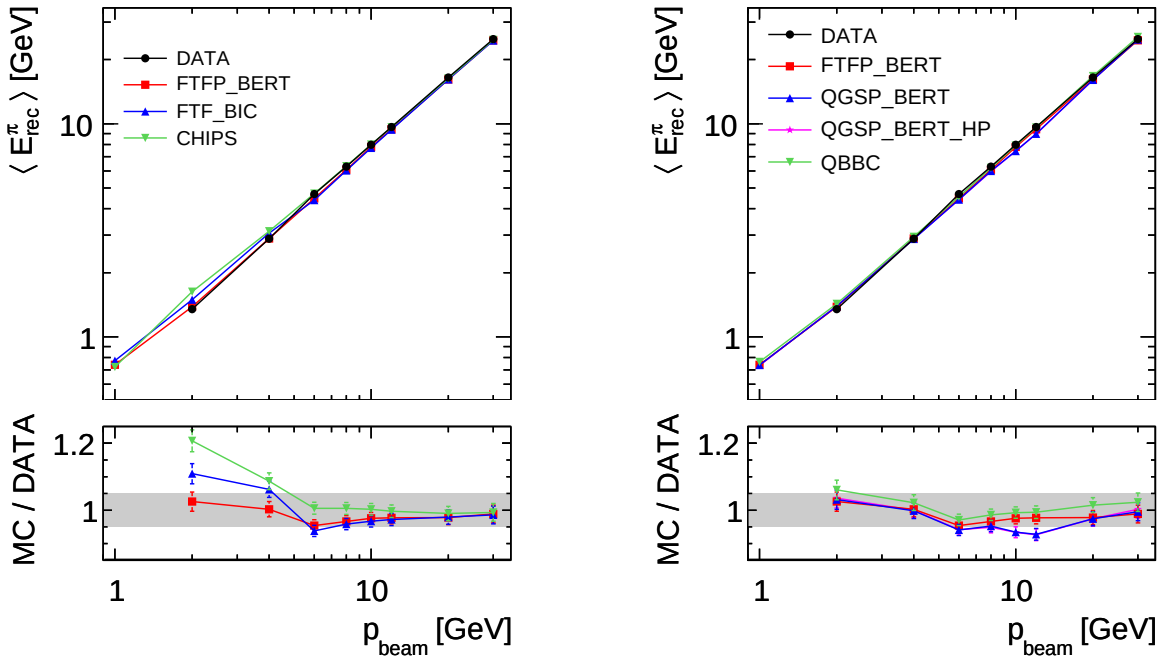

(a) (b)

Figure 8.5: (a-b) Mean reconstructed energy $\langle E^{\pi}_{\text{rec}} \rangle$ for pion data and Monte Carlo simulations using different GEANT4 physics lists as a function of the pion momentum. The ratios between the predictions from simulations and data are presented as well with gray bands indicating the range of 5% agreement.

The presented physics lists use either the Bertini cascade model, the binary cascade model, or the CHIPS model to predict the energy deposited by pions with a momentum of 4 GeV or less. In this energy range, the predictions made by the Bertini cascade model agree with data within 3%, which is the same order of magnitude as the uncertainties due to calibration and subtraction of electron contaminations. The binary cascade model tends to overestimate the AHCAL response by 5-10%, while the CHIPS model overestimates the AHCAL response by 10-20% in this energy range.

The Fritiof string model in combination with either the Bertini or the binary cascade model tends to underestimate the AHCAL response to pions between 6 GeV and 30 GeV. However, the agreement between data and simulations is still within 5% and improves with increasing pion energy. In this momentum range, the CHIPS model predicts the energies deposited by pions within 1% agreement with data (the deviation is smaller than the calibration uncertainties) and shows the smallest dependence of the agreement on the pion momentum.

The quark-gluon string model in combination with the Bertini cascade model shows the same agreement with data as the Fritiof-based physics lists at 20 GeV and 30 GeV. The QGSP_BERT physics list uses the low-energy parametrization in combination with the Bertini cascade model for pion momenta between 10 GeV and 12 GeV, which underestimates the visible energy by about 5%.

The QBBC physics list predicts roughly 2% higher visible energies than FTFP_BERT at all pion momenta, although both physics lists use the same models for pion-nucleus interactions (the Fritiof string model and the Bertini cascade model) below 12.5 GeV. However, the QBBC physics list describes the inelastic scattering of protons and neutrons below 1.5 GeV with the binary cascade model, whereas the FTFP_BERT physics list applies the Bertini cascade model for these interactions. Because the binary cascade model if found to overestimate the AHCAL response to pions, the differences between the QBBC and the FTFP_BERT physics list are attributed to higher visible energy depositions predicted by the binary cascade model for secondary protons and neutrons at low energies.

Using QGSP_BERT with the HP package gives the same predictions as QGSP_BERT without this extension. As discussed in Chapter 5, this agreement is expected because the HP package mainly affects late energy depositions beyond the integration time of the AHCAL electronics (and the corresponding time cut of 150 ns applied to simulations).

8.2 Longitudinal Pion Cascade Profiles

The digitized AHCAL simulations provide information about the types of the particles depositing energy in the sensitive detector material [30]. The energy fraction deposited by electrons and positrons within a hadronic cascade correlates with the electromagnetic fraction of these cascades (according to GEANT4 simulations, the correlation is about 70% for 1 GeV pions and larger than 90% for pions with energies between 6 GeV and 30 GeV). Since the electromagnetic fraction directly affects the shower shape, differences in the fraction of energy deposited by electrons and positrons give hints to different electromagnetic fractions in simulations causing certain cascade features.

Figures 8.6(a) and 8.6(b) show the longitudinal shower profiles from the start of the AHCAL for 4 GeV pion data and GEANT4 simulations using the Bertini cascade model (in

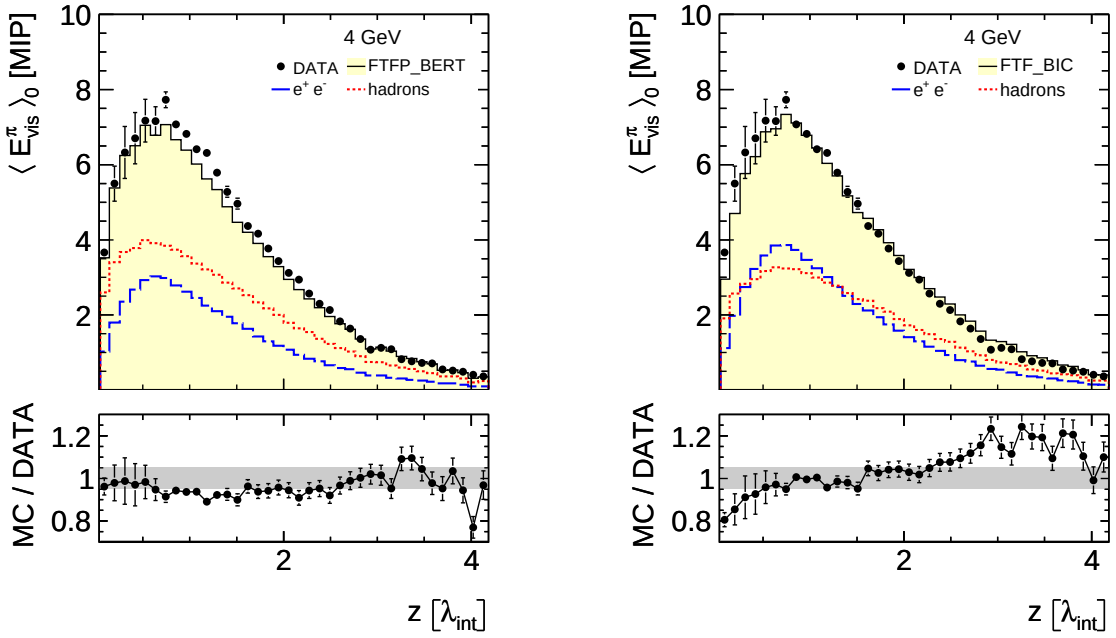

(a)

(b)

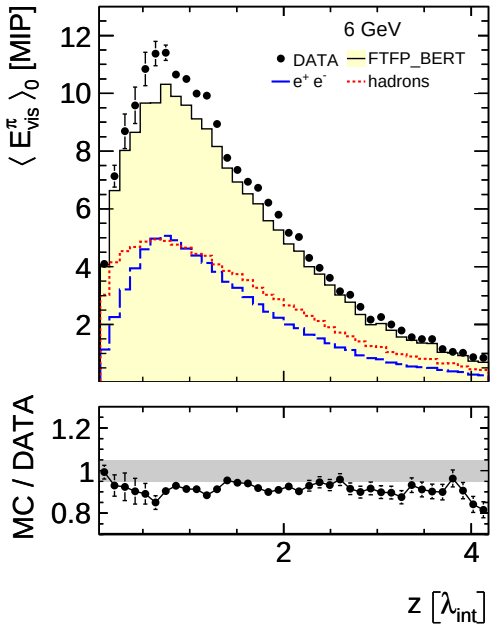

(c)

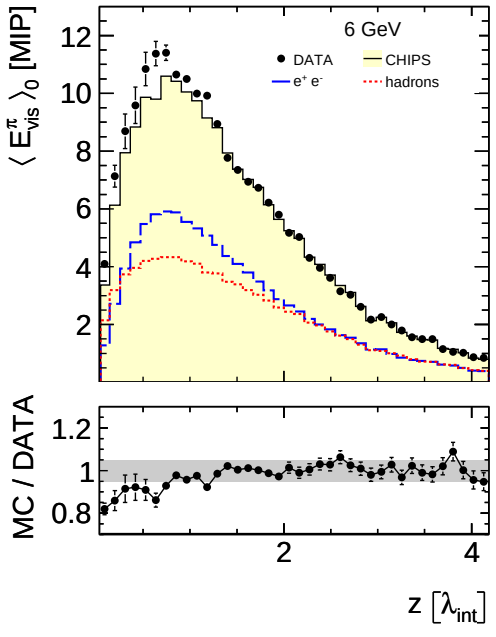

(d)

Figure 8.6: Longitudinal shower profiles, i.e. the mean visible energy $\langle E^{\pi}_{\mathrm{vis}} \rangle_0$ (after subtracting the mean noise for each layer) as a function of the AHCAL depth z, for (a) 4 GeV pion data and simulations using the Bertini cascade model (FTFP_BERT physics list), (b) 4 GeV pion data and simulations using the binary cascade model (FTF_BIC physics list), (c) 6 GeV pion data and simulations using the Fritiof string model and the Bertini cascade model (FTFP_BERT physics list), and (d) 6 GeV pion data and simulations using the CHIPS physics list. Points represent data and histograms (solid lines) the predictions from Monte Carlo simulations. Dashed histograms indicate the energy deposited by electrons and positrons, whereas dotted histograms show the energy deposited by hadrons.

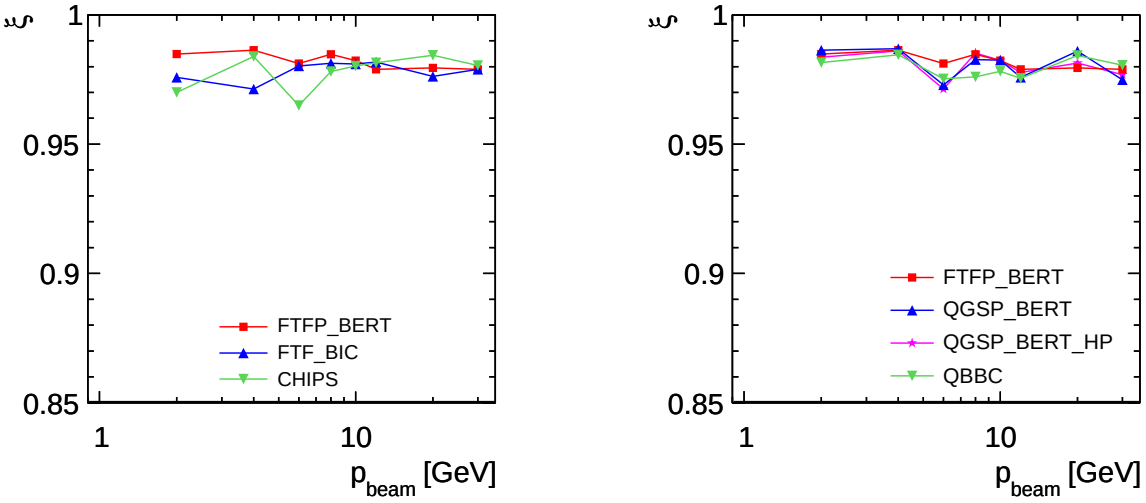

Figure 8.7: (a-b) Quality ξ of the shape agreement of normalized longitudinal profiles for pion cascades between data and Monte Carlo simulations using different GEANT4 physics lists as a function of the pion momentum. The definition of ξ is given in the text.

FTFP_BERT) and the binary cascade model (in FTF_BIC). The mean noise contribution is subtracted for each bin. The figures also illustrate the energy deposited by electrons and positrons, i.e. the electromagnetic fraction, and hadrons in the cascade. Furthermore, the ratios between measured energies and predictions from simulations are presented. The Bertini cascade model describes the longitudinal profile within 5-10% over thefull AHCAL length, whereas the binary cascade model underestimates the energy in the front part of the calorimeter (below $0.5\,\lambda_{\text{int}}$) by up to 20% and overestimates the energy in the rear part of the calorimeter (beyond $2.5\,\lambda_{\text{int}}$) by 10-20%. The different profile shapes predicted by the models is associated with a larger hadronic and a smaller electromagnetic shower component predicted by the Bertini cascade model than by the binary cascade model.

Figures 8.6(c) and 8.6(d) present the measured longitudinal profiles for 6 GeV pions and simulation predictions for FTFP_BERT and CHIPS. The FTFP_BERT physics list shows smaller contributions from the electromagnetic fraction in the shower maximum than CHIPS and underestimates the energy depositions by about 5-10% over the full AHCAL length. CHIPS describes the shower profile within 5% from $1\,\lambda_{\text{int}}$ on and underestimates the energy depositions by up to 20% before this calorimeter depth.

Normalizing the longitudinal profiles to a total visible energy of one allows to compare the overall shape agreement between measured and simulated profiles. The observable ξ quantifies the agreement between profile shapes in data and Monte Carlo simulations, where ξ is the overlap of the normalized profiles, i.e.

$$\xi = \sum_{\text{i}} \min\left(\frac{E_{\text{i}}^{\text{MC}}}{E^{\text{MC}}}, \frac{E_{\text{i}}^{\text{data}}}{E^{\text{data}}}\right), \tag{8.1}$$

where E^{data} and E^{MC} are the mean visible energies in all AHCAL layers from data and simulations and E_i^{data} and E_i^{MC} are the mean visible energies for single layers i. Figures 8.7(a)

and 8.7(b) show ξ as a function of the pion momentum for different GEANT4 physics lists. All physics lists describe the longitudinal pion cascade profiles correctly within 5%. At 2 GeV and 4 GeV pion momentum, the Bertini cascade model describes the profiles better than the CHIPS or the binary cascade model. From 6 GeV to 10 GeV, the agreement for QBBC is smaller than for FTFP_BERT.

The shower depth and the standard deviation of the longitudinal shower extension characterize the longitudinal profile of a cascade. The shower depth in the AHCAL, i.e. the center of gravity in longitudinal direction, is defined for each cascade as

$$Z = \frac{\sum_{\mathrm{i}} E_{\mathrm{i}} z_{\mathrm{i}}}{\sum_{\mathrm{i}} E_{\mathrm{i}}}, \tag{8.2}$$

where z_{i} is the distance of a single energy deposition i from the AHCAL front face. The standard deviation is a measure of the cascade length and is defined as

$$\sigma_{\mathrm{z}} = \sqrt{\frac{\sum_{\mathrm{i}} E_{\mathrm{i}} \cdot (z_{\mathrm{i}} - Z)^2}{\sum_{\mathrm{i}} E_{\mathrm{i}}}}. \tag{8.3}$$

The electron contamination of the 2, 4, and 6 GeV pion data is subtracted from the mean shower depth $\langle Z \rangle$ and the mean standard deviation $\langle \sigma_{\mathrm{Z}} \rangle$ by subtracting the means of the respective observables for electrons weighted by the contamination fraction.

Mean and Standard Deviation: Comparing Data with Previous Measurements

Figures 8.8(a) and 8.8(b) show the mean shower depth and the mean standard deviation calculated with respect to the first inelastic interaction for pion cascades starting within the first five AHCAL layers. The additional cut reduces the effect of longitudinal leakage. The figures compare results obtained for the low-energetic pion data to results obtained for previous measurements at higher beam momenta. The shift of the mean shower depth and the mean standard deviation by up to $0.1\,\lambda_{\mathrm{int}}$ corresponds to the depth of a single layer and is attributed to different algorithms used to identify the point of the first inelastic interaction for the two independent analyses. The clustering algorithm described in Section 6.1 is applied to the low-energetic pion data and yields the position of the first inelastic interaction, whereas the algorithm applied to the high-energetic pion data identifies the first sensitive layer behind this interaction.

Mean and Standard Deviation: Comparing Data with GEANT4 Simulations

Figures 8.9(a) and 8.9(b) present the mean shower depth in the AHCAL as a function of the pion momentum for data and simulations using different physics lists. As expected, the mean shower depth increases logarithmically with increasing pion energy.

Figures 8.9(c) and 8.9(d) present the mean longitudinal shower extension in the AHCAL at different pion energies for measurements and simulations using several physics lists. Between 8 GeV and 30 GeV, the mean shower extension increases logarithmically with increasing pion energy. At lower energies, the shower extension increases again. This change in direction is attributed to the effect of noise in the AHCAL, which affects the extension of pion showers at low energies stronger than at higher energies. For random-trigger events,

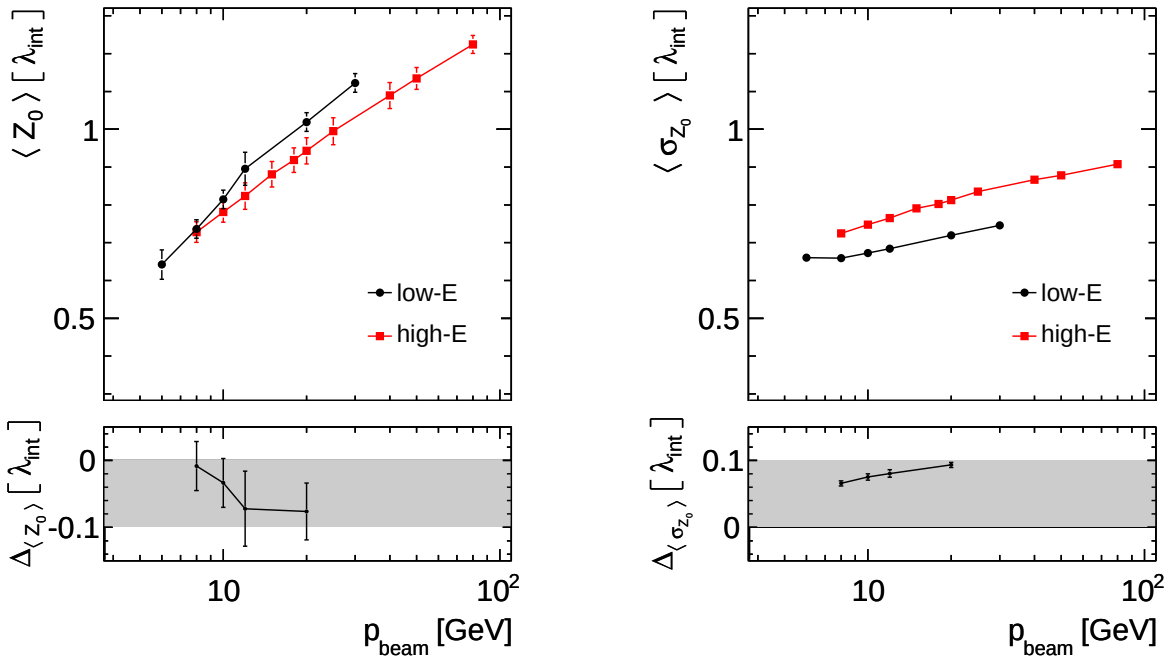

(a) (b)

Figure 8.8: (a) Mean cascade depth $\langle Z_0 \rangle$ with respect to the first inelastic hadron interaction in the AHCAL and (b) mean cascade length $\langle \sigma_{Z_0} \rangle$ for pion data collected at low pion momenta (low-E) and high pion momenta (high-E, from [30]) and the differences $\Delta_{\langle Z_0 \rangle}$ and $\Delta_{\langle \sigma_{Z_0} \rangle}$ between the results from the high-E and the low-E measurements at the beam momenta covered by both data sets. Gray bands indicate the range of agreement within one AHCAL layer.

the mean standard deviation of the longitudinal position of energy depositions above the 0.5 MIP threshold is 1.1 λ_{int}.

The mean shower depth predicted by all physics lists studied in this analysis except for FTF_BIC agree with data within 3% over the covered momentum range from 2 GeV to 30 GeV. The binary cascade model (in FTF_BIC) overestimates the mean shower depth by 5% at 4 GeV. Between 10 GeV and 30 GeV, the low-energy parametrization and the quark-gluon string model in combination with the Bertini cascade model (QGSP_BERT) underestimate the mean shower depth, whereas the Fritiof model in combination with the Bertini model (FTFP_BERT) overestimates this parameter. The predictions for the mean shower depth from the Fritiof model in combination with the Bertini model (FTFP_BERT) agree best with pion data between 2 GeV and 30 GeV.

The mean standard deviation predicted by all physics lists agrees with data within 5%. The Fritiof model in combination with the Bertini cascade model (FTFP_BERT) describes this parameter within 2% agreement with data over the full studied pion momentum range. The quark-gluon string model in combination with the Bertini cascade model (QGSP_BERT) yields mean standard deviations that agree with data within 2% below 10 GeV (Bertini model range) and disagree by up to 5% at 30 GeV with increasing contribution from the quark-gluon string model. The effect of the quark-gluon string model predicting too small standard deviations is reflected by the QBBC physics list yielding smaller standard deviations than FTFP_BERT above 20 GeV as well. Between 6 GeV

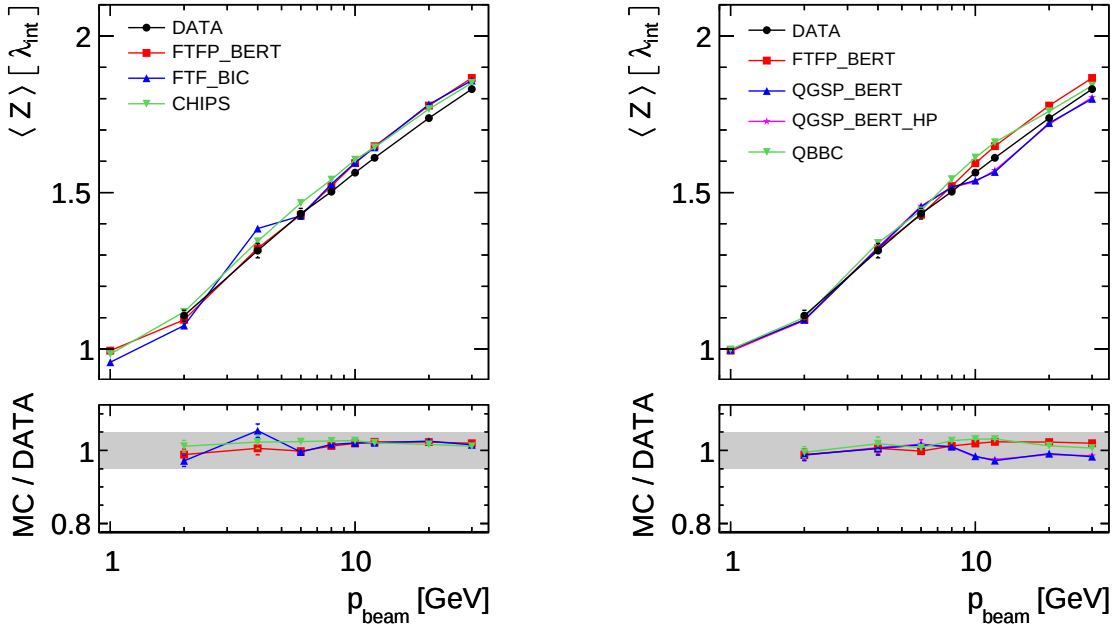

(a)

(b)

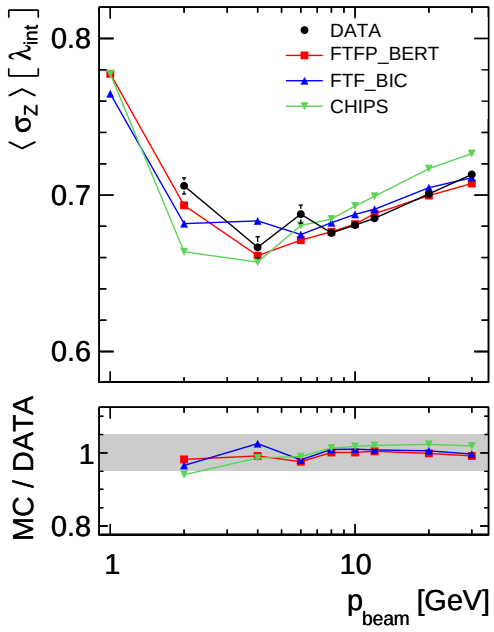

(c)

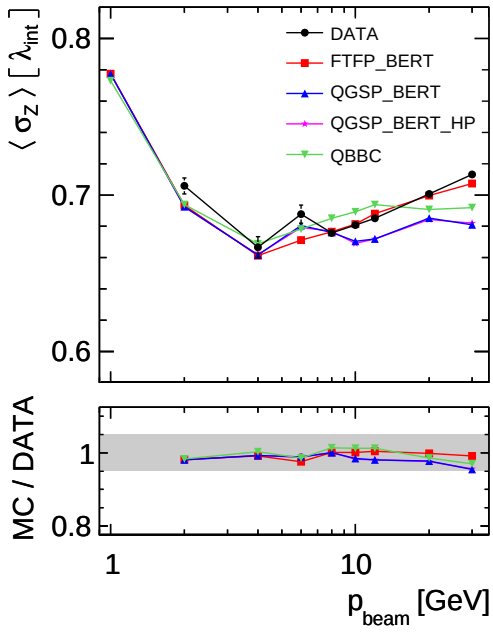

(d)

Figure 8.9: (a-b) Mean cascade depth $\langle Z \rangle$ and (c-d) mean cascade length $\langle \sigma_Z \rangle$ for pion data and Monte Carlo simulations using different GEANT4 physics lists as a function of the pion momentum. The ratios between the predictions from simulations and data are presented as well with gray bands indicating the range of 5% agreement.

and 10 GeV, both QBBC and FTFP_BERT use the Fritiof model with the precompound and the Bertini cascade model for pion interactions. However, QBBC predicts about 1% larger mean shower depths and 1% larger standard deviations than FTFP_BERT due to the different models used for protons and neutrons below 1.5 GeV.

As suggested by the ξ-value comparison of the normalized shower shapes, the predicitions for the longitudinal shower development from the Fritiof string model in combination with the Bertini cascade model agree best with pion data between 2 GeV and 30 GeV beam momentum.

8.3 Radial Pion Cascade Profiles

For the extraction of radial shower profiles, all physical AHCAL cells are subdivided into virtual cells of $1 \times 1\,\mathrm{cm}^2$ [29]. The number of MIP-like energy depositions contributing to the visible energy in each physical cell is estimated and equally distributed over a corresponding number of virtual cells in the area of the physical cell. Because the dimension of the smallest AHCAL cells is $3 \times 3\,\mathrm{cm}^2$, a radial bin width of 3 cm is chosen for the profiles. The profiles are calculated with respect to the center of gravity in the x-y plane for each event.

Figures 8.10(a) and 8.10(b) show the radial profiles for 2 GeV pion data and simulations using the Bertini cascade model (in FTFP_BERT) and the binary cascade model (in FTF_BIC). Analog to the longitudinal shower profiles presented in Section 8.2, the fractions of electromagnetic (electrons and positrons) and hadronic (all other particles) energy deposition are indicated separately. The Bertini cascade model underestimates the energy density up to 240 mm radial distance by 5-10%, whereas the binary cascade model underestimates the energy density up to 100 mm by 5% and overestimates the energy density by 5% between 180 mm and 240 mm radial shower extension. The overall agreement is better for the binary cascade model than for the Bertini cascade model. The figures indicate that the radial shapes are dominated by the hadronic component and that the better shape agreement of the binary cascade model is related to a larger contribution from the electromagnetic fraction at all radial distances.

Figure 8.10(c) presents the radial profile for 8 GeV pions for data and simulations using the Bertini cascade model (in QGSP_BERT). At this pion momentum, the Bertini cascade model underestimates the energy density at all radial distances up to 240 mm by 5%. This underestimation is consistent with the underestimation of the mean visible energy in the AHCAL predicted by the Bertini cascade model for 8 GeV pions. Except for this scale shift, this model describes the radial energy distribution very good at this pion momentum. The figure illustrates the similar level of contributions from the hadronic component and the electromagnetic fraction to the core of the radial shower profile (up to about 90 mm).

Figure 8.10(d) shows the radial profile for 20 GeV pion data and simulations using the CHIPS physics list. Data and simulations agree within less than 5% for radial distances up to 210 mm. According to the simulations, the core of the radial profile (up to about 90 mm) is dominated by the electromagnetic fraction at this pion momentum.

The overall shape agreement between data and simulations is quantified by normalizing the profiles and calculating the ξ value from Eq. (8.3). Figures 8.11(a) and 8.11(b) show the ξ values for radial pion profiles as a function of the pion momentum for different physics

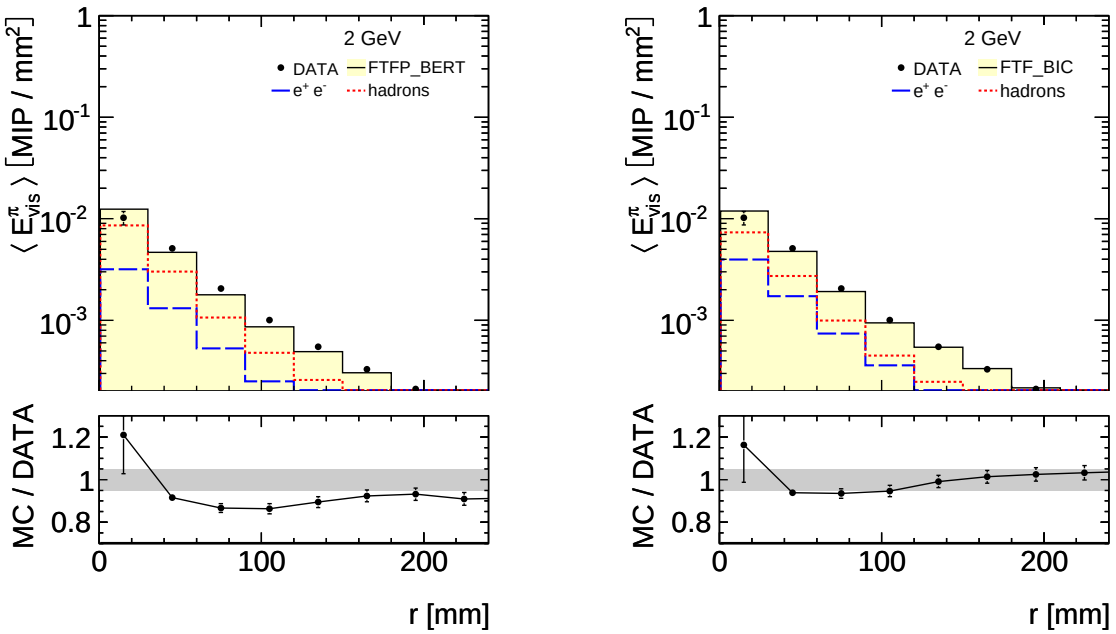

(a)

(b)

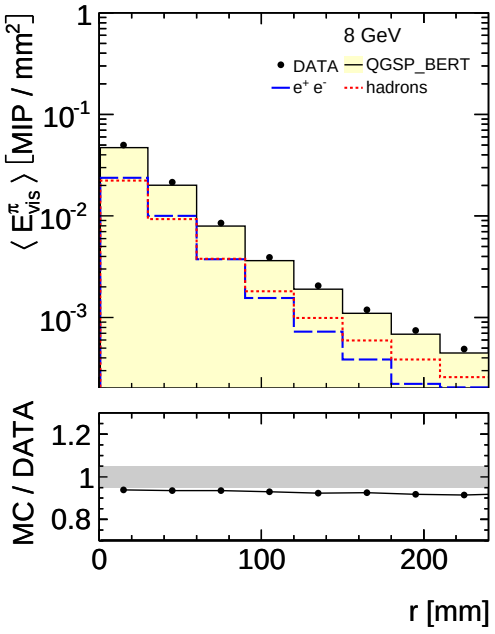

(c)

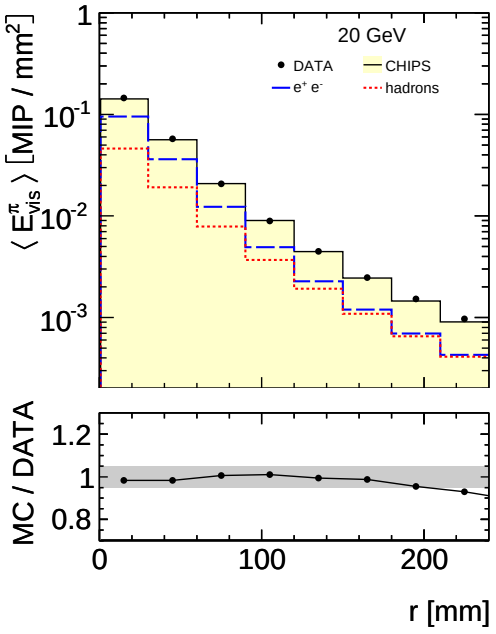

(d)

Figure 8.10: Radial shower profiles, i.e. the mean visible energy $\langle E^{\pi}_{\text{vis}} \rangle$ as a function of the radial distance r from the energy center of gravity, for (a) 2 GeV pion data and simulations using the Bertini cascade model (FTFP_BERT physics list), (b) 2 GeV pion data and simulations using the binary cascade model (FTF_BIC physics list), (c) 8 GeV pion data and simulations using the Bertini cascade model (QGSP_BERT physics list), and (d) 20 GeV pion data and simulations using the CHIPS physics list. Points represent data and histograms (solid lines) the predictions from Monte Carlo simulations. Dashed histograms indicate the energy deposited by electrons and positrons, whereas dotted histograms show the energy deposited by hadrons.

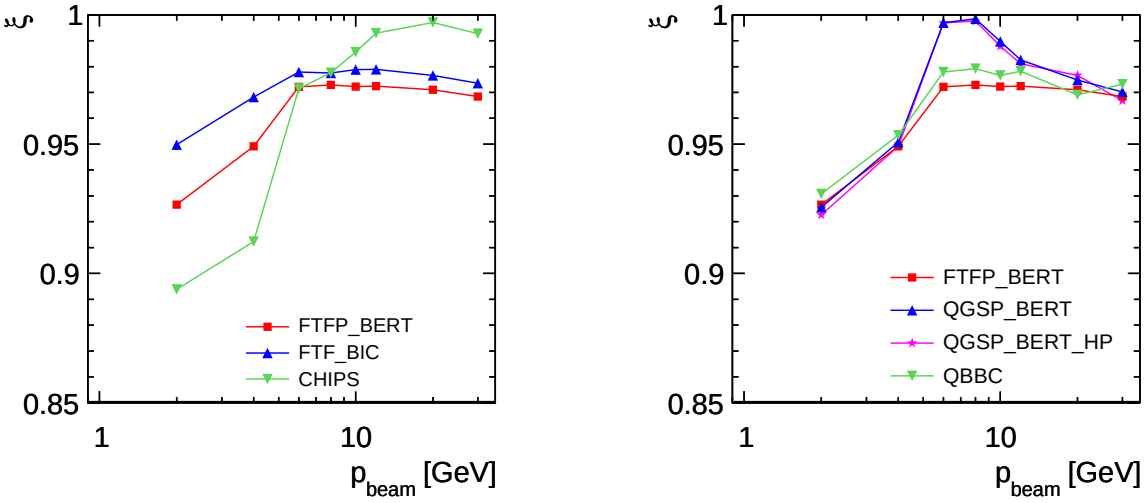

(a) (b)

Figure 8.11: (a-b) Quality ξ of the shape agreement of normalized radial profiles for pion cascades between data and Monte Carlo simulations using different GEANT4 physics lists as a function of the pion momentum. The definition of ξ is given in the text.

lists. Generally, the description of the radial shower profiles by simulations is worse than the description of the longitudinal profiles. At 2 GeV and 4 GeV, the binary cascade model yields the best shape agreement (better than 95%) between data and simulations. The shape agreement between data and CHIPS at these pion momenta is only 90%. However, CHIPS yields the best description of the radial profile shape between 12 GeV and 30 GeV ($\xi = 99\%$). In the pion momentum range between 6 GeV and 10 GeV, the predictions made by the Bertini cascade model (used by QGSP_BERT in this momentum range) agree with data better than 99%, respectively. At 4 GeV and 2 GeV the agreement between the Bertini model (in QGSP_BERT, FTFP_BERT, and QBBC which agree with each other) and data drops to 95% and 93%. The agreement between the Fritiof based physics lists and data (from FTFP_BERT, FTF_BIC, and QBBC) is at 97% between 6 GeV and 30 GeV. With decreasing contribution from the Bertini cascade model and the transition to the LEP and the Quark-gluon string model between 10 GeV and 30 GeV, the agreement between QGSP_BERT and data decreases to the same level as the agreement observed for the physics lists based on the Fritiof string model. As for all other investigated observables, the QGSP_BERT and the QGSP_BERT_HP physics lists give consistent predictions of the shapes of the radial cascade profiles.

Analog to the longitudinal profiles, radial shower profiles are characterized by the mean shower radius and the mean standard deviation of the radial cascade extension. The shower radius for a single event is defined as

$$R = \frac{\sum_{\mathrm{i}} E_{\mathrm{i}} r_{\mathrm{i}}}{\sum_{\mathrm{i}} E_{\mathrm{i}}} \tag{8.4}$$

with a standard deviation of

$$\sigma_{\mathrm{R}} = \sqrt{\frac{\sum E_{\mathrm{i}} \cdot (r_{\mathrm{i}} - R)^2}{\sum_{\mathrm{i}} E_{\mathrm{i}}}} \tag{8.5}$$

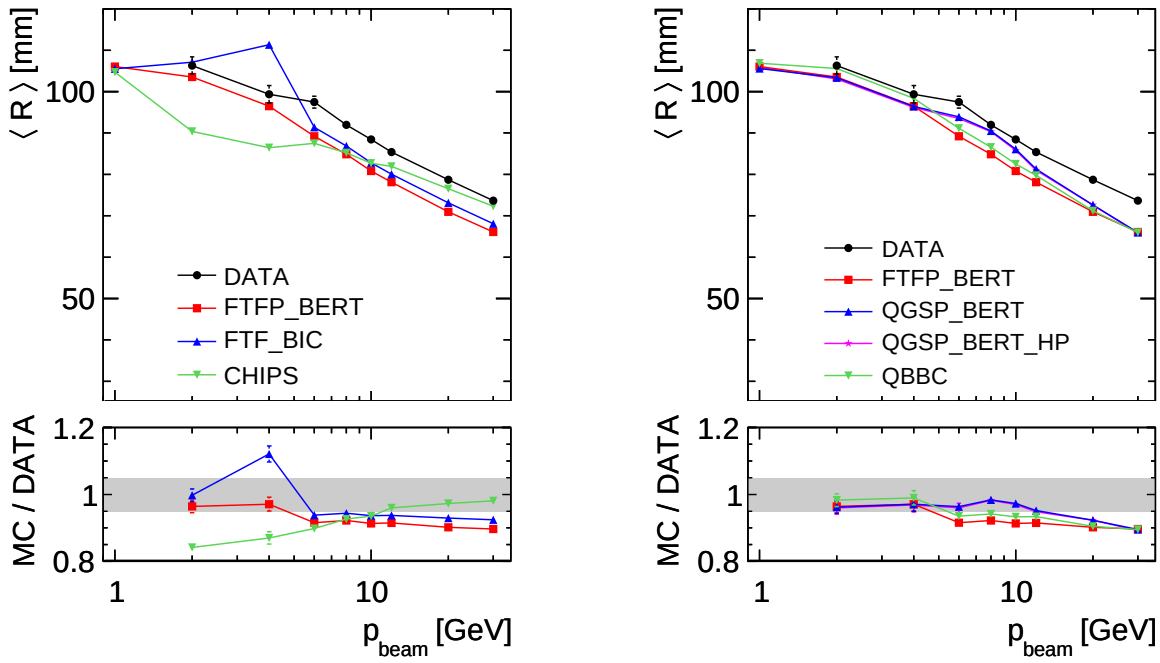

(a)

(b)

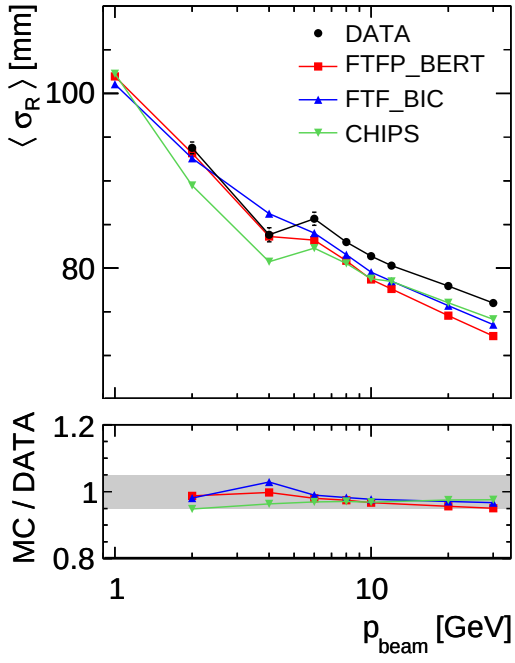

(c)

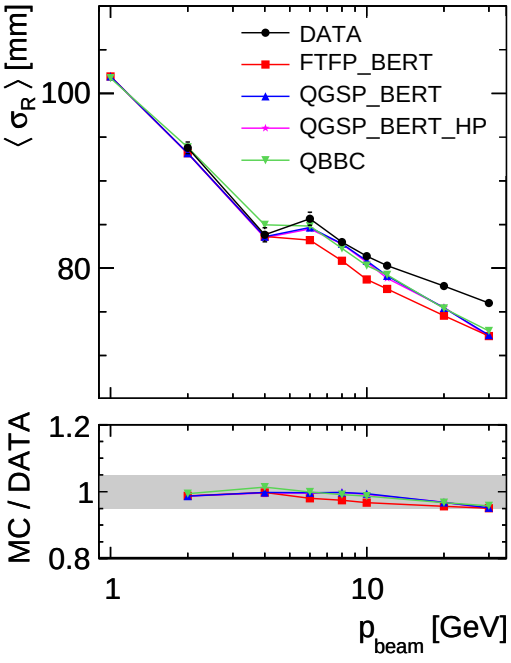

(d)

Figure 8.12: (a-b) Mean cascade radius $\langle R \rangle$ and (c-d) mean radial standard deviation $\langle \sigma_R \rangle$ for pion data and Monte Carlo simulations using different GEANT4 physics lists as a function of the pion momentum. The ratios between the predictions from simulations and data are presented as well with gray bands indicating the range of 5% agreement.

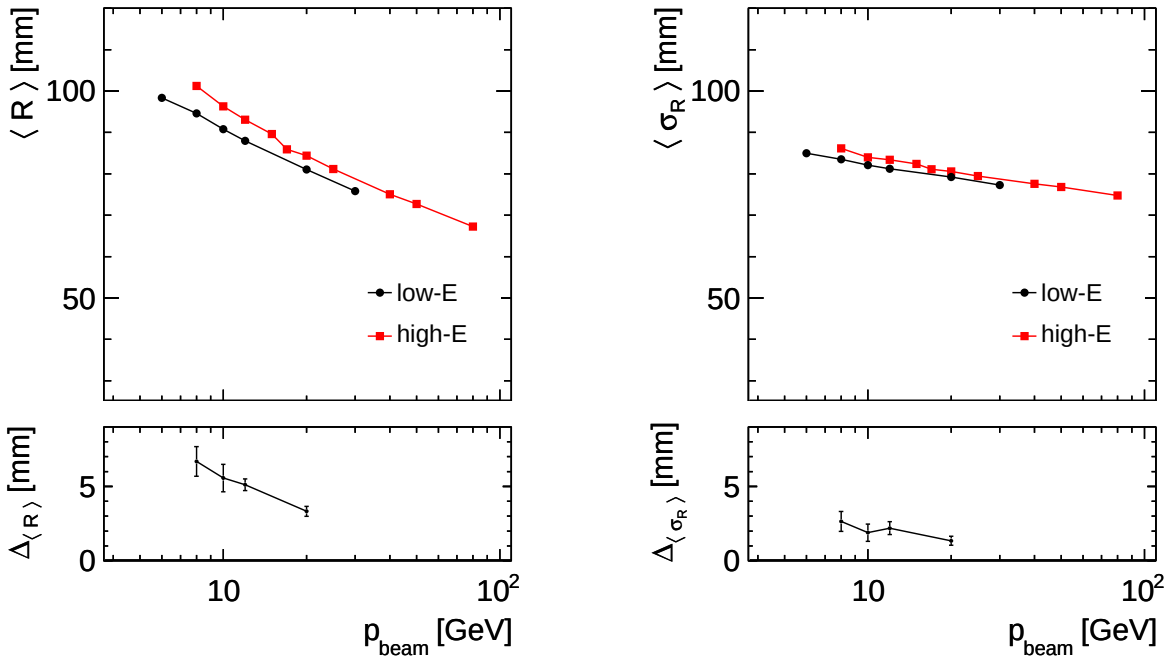

(a) (b)

Figure 8.13: (a) Mean cascade radius $\langle R \rangle$ and (b) mean radial standard deviation $\langle \sigma_{\mathrm{R}} \rangle$ for pion data collected at low pion momenta (low-E) and high pion momenta (high-E, from [30]) and the differences $\Delta_{\langle R \rangle}$ and $\Delta_{\langle \sigma_{\mathrm{R}} \rangle}$ between the results from the high-E and the low-E measurements at the beam momenta covered by both data sets.

using

$$r_{\mathrm{i}} = \sqrt{(x_{\mathrm{i}} - x_{\mathrm{cog}})^2 + (y_{\mathrm{i}} - y_{\mathrm{cog}})^2}\,, \tag{8.6}$$

where x_{i} and y_{i} are the coordinates of the energy depositions E_{i} and x_{cog} and y_{cog} are the coordinates of the energy center of gravity of the cascade. The electron contamination at 2, 4, and 6 GeV is accounted for.

Mean and Standard Deviation: Comparing Data with Previous Measurements

Figures 8.13(a) and 8.13(b) compare the mean shower radius and the mean standard deviation of the shower radius extracted in this analysis for low-energetic pions to previous measurements of pions in a higher momentum range. A containment cut requiring the first inelastic interaction to occur in the first five AHCAL layers is applied for comparability of the independent analyses. The measurements for pions at the overlap momenta differ by less than 10 mm for the mean radius and less than 3 mm for the mean standard deviation. These differences are smaller than half the size of the smallest AHCAL cells. The differences are attributed to a different selection procedures for excluding cells and different beam impact positions. Furthermore, the different calibration sets applied correspond to a different MIP threshold which affects the hits with the lowest energies at the edge of a cascade and thus the lateral shower extension most.

Mean and Standard Deviation: Comparing Data with GEANT4 Simulations

Figures 8.12(a) and 8.12(b) present the mean shower radius as a function of the beam momentum for pion data and Monte Carlo simulations using different physics lists. The mean radius decreases logarithmically with increasing cascade energy because the electromagnetic fraction (with a smaller radial extension than the hadronic component) in the cascade increases. Figures 8.12(c) and 8.12(d) show the mean standard deviation of the shower radius as a function of the pion momentum for data and Monte Carlo simulations using different physics lists. The spread decreases with increasing beam momentum. Because the kink in data at 4 GeV is reproduced by simulations, this feature is attributed to detector effects from noise and excluded cells. The mean standard deviation of the shower radius predicted by all studied physics lists agrees with data within 5%.

The Bertini cascade model (used by the FTFP_BERT and QBBC physics lists at 4 GeV and below and by the QGSP_BERT physics list below 10 GeV) underestimates the mean shower radius by less than 5% in the range from 2 GeV to 10 GeV. The agreement between data and simulations increases with increasing pion momentum in this range, as observed for the overall radial shower shape (ξ values). In this pion momentum range, the standard deviation of the shower radius predicted by the Bertini cascade model agrees with data within less than 2%. The mean shower radius and standard deviation predicted by the other models investigated deviate more from data in this pion momentum range. Although the overall shower shape predicted by the binary cascade at 4 GeV and 2 GeV agrees better with data than the shape predicted by the Bertini cascade model, the binary cascade model overestimates the mean shower radius and the mean standard deviation at 4 GeV by about 10% and 2% and agrees with the Bertini cascade model at 2 GeV.

The CHIPS model underestimates the mean shower radius by 20% with respect to data at 2 GeV. The agreement between CHIPS and data improves for increasing pion momentum and is better than 5% above 10 GeV. This agrees with the observed mismatch of the overall radial profile shape. The standard deviation of the shower radius predicted by CHIPS agrees with data within 5% over the full momentum range covered by this analysis.

The Fritiof model in combination with the binary cascade model (FTF_BIC) predicts about 3% larger shower radii than the Fritiof model in combination with the Bertini cascade model (FTFP_BERT) between 6 GeV and 30 GeV. This overestimate is consistent with the binary cascade model predicting larger shower radii than the Bertini cascade, which is observed at 2 GeV and 4 GeV.

At 20 GeV and 30 GeV, the mean shower radius predicted by CHIPS agrees with data within 2%, whereas the predictions from other models underestimate the mean shower radius by 5-10%.

8.4 Summary

This chapter presents the analysis of pion data collected with the AHCAL physics prototype at pion momenta between 2 GeV and 30 GeV. This is the first analysis based on this detector at energies below 8 GeV. The application of non-native muon calibration factors does not affect the AHCAL response to pions calibrated to the GeV scale, which confirms the portability of the AHCAL muon calibration factors to different experimental setups

and operating conditions discussed in Section 4.2. Comparisons with a previous pion analysis at overlapping energies show a very good agreement for topological variables (mean shower depth and radius and the respective standard deviations). The absolute energy scales of the independent analyses differ by 5% and need further investigation.

The CALICE data complement thin target experiments [90] for the validation of simulations, for exploring the strengths and weaknesses of different models for hadron physics, and for finding indications for ways of refining the simulations of hadron cascades. This analysis covers the transition energies between models combined in single physics lists. These transitions are clearly visible in the comparisons between data and simulations. Furthermore, the pion data at 2 GeV and 4 GeV allow for a direct comparison of the Bertini cascade model, the binary cascade model, and the CHIPS model in this range without influences from other models used at higher energies by the physics lists. In contrast to this, the performance of string models (QGS or FTF) at higher energies always depends on the cascade model used for secondary particles with lower energies. This analysis yields the same results for the QGSP_BERT physics list with or without using the high precision extension, which is attributed to the signal shaping time of the AHCAL (included as time-cut of 150 ns in the simulation) removing contributions from late energy depositions. The QBBC physics list, which has not been validated with CALICE data before, shows a similar agreement with data as FTFP_BERT and QGSP_BERT in the convered energy range.

The pion response predicted by the Bertini cascade model at 2 GeV and 4 GeV agrees with data within 3% calibration uncertainty, whereas the binary cascademodel and the CHIPS model show larger disagreements at these energies. Between 6 GeV and 30 GeV, the CHIPS model shows a stable agreement with data within less than 1%, which is about half the calibration uncertainties. The disagreement for other models in this energy range is larger, but decreases for higher energies. The FTFP_BERT physics list describes the measured pion response within 5% in this energy range. Taking into account the absolute energy scale uncertainty of 5%, FTFP_BERT gives the best overall performance for predicting the AHCAL response to pions.

The best performing physics list for predicting longitudinal pion cascades shapes is FTFP_BERT. Between 2 GeV and 10 GeV, the Bertini cascade model gives the best description of the overall shower shape and predicts the mean shower depth within 3% and the shower length within 2%. Above 8 GeV, all physics lists give comparable results for the shower shape agreement. All physics lists except for FTF_BIC, which overestimates the mean shower depth by 5% at 4 GeV, predict the mean shower depth within 3% and the shower length within 5% of the respective observables for data.

Except for the Binary cascade model at 4 GeV, all models tend to underestimate the mean shower radius and radial standard deviation at all pion energies covred by this analysis. The transverse shower profile shape is best reproduced by the binary cascade model at 2 and 4 GeV, while the Bertini cascade model yields the best shape agreement between 6 GeV and 8 GeV. From 12 GeV to 30 GeV, the CHIPS model gives the best prediction for the mean shower radius with deviations below 5%. The QGSP_BERT physics list underestimates the radius by less than 5% and the radial standard deviation by less than 2% up to 12 GeV and by 10% (mean) and 5% (standard deviation) at 30 GeV. The disagreement above 12 GeV shows a strong energy dependence and worsens with increasing contribution

of the low-energy parametrization and the quark-gluon string model. Nevertheless, the QGSP_BERT phyiscs list shows the best overall performance between 2 GeV and 30 GeV.

From 2 GeV to 8 GeV, the Bertini cascade model shows the best agreement with data for all observables which are compared. Between 12 GeV and 30 GeV, the CHIPS model yields the best agreement with data for all these parameters. This result shows a significant improvement of the CHIPS model in the used version 9.4 of GEANT4 with respect to previous versions, for which the deviations between CHIPS and data in this pion momentum range are much larger (up to 10% deviation for the predicted response and longitudinal cascade extension).

Summary and Outlook

The CALICE collaboration develops highly granular calorimeters for detectors based on the Particle Flow approach. These detectors are expected to meet the jet energy resolution requirements of experiments at a future electron-positron linear collider. CALICE investigates various calorimeter design options and has realized them as physics prototypes, which have been operated in combined setups at several test-beam facilities to demonstrate the viability of the novel technologies employed. This measurement program evaluates not only the operation and performance of single calorimeters, but also the integrated operation of an electromagnetic calorimeter, a hadron calorimeter, and a tail catcher using a common data acquisition system and common test-beam infrastructure. Furthermore, the data collected with the physics prototypes allow to study hadron showers in great detail and are a valuable addition to thin target data for validating the simulation of hadron physics. The measurements allow for exploring the strengths and weaknesses of various simulation models for hadron cascades and for finding indications of how to refine these simulations. In addition, these data are used to test and enhance Particle Flow reconstruction algorithms with real data.

The CALICE Experiment at Fermilab

This thesis reports on the successful commissioning and stable operation of the CALICE experiment including the physics prototypes of the Si-W ECAL, the Sci-ECAL, the AHCAL, the TCMT, and auxiliary beam-line instrumentation at the Fermilab Test-beam facility. A differential Čerenkov detector is used to tag particles of different types. The measurements at Fermilab conclude the physics prototype program for these detector combinations and provide pion, proton, and electron data from 1 GeV to 120 GeV beam momentum complementing existing data sets. The main focus of this thesis lies on the AHCAL physics prototype, which is a scintillator-steel sampling calorimeter for hadrons. The scintillator layers are pieced together from individual tiles with embedded SiPMs for measuring the scintillation light. With a total of 7608 readout channels and its initial commissioning in 2005, the AHCAL physics prototype represents the first large-scale application of SiPMs.

A voltage adjustment procedure is successfully applied during the AHCAL commissioning to shift the mean light yield, a figure of merit related to the signal to noise ratio of the detector, to a target value of $14\,\frac{\text{pix}}{\text{MIP}}$. Establishing this procedures illustrates a good understanding of the SiPM behavior and is therefore an important result for future test-beam measurements as well as for operating calorimeters with SiPM readout in a detector at a collider experiment.

Calibration of Calorimeters with SiPM Readout

Equalizing the response of all cells in a calorimeter with SiPM readout requires measurements of the response of each cell to muons acting as MIPs. This response changes with operating voltage and temperature. The correction of the AHCAL muon calibration factors for the effects of temperature changes is established and leads to a total uncertainty of the response equalization of about 1.6%, which is the dominant source of uncertainties for measuring single electrons below 10 GeV and single pions below 40 GeV.

Using the AHCAL as an example, this thesis demonstrates the possibility to transport a set of muon calibration factors to a different experimental setup and to different operation conditions. Shifts of the MIP scale due to the application of different equalization factors are absorbed by the final calibration to the absolute energy scale. The linearity of the AHCAL response to electrons, the energy resolution for electrons, and the detector response to pions calibrated to the GeV scale are not affected by using a non-native set of response equalization factors. Therefore, it is possible to extract these factors for the layers of a calorimeter using SiPMs in a collider detector with muon beams before installation and to correct them for the effects of changing bias voltages or temperatures during operation.

The identification and exclusion from analysis of 270 dead, noisy, and unstable cells improves the homogeneity and stability of the AHCAL response.

Analysis of Low-energetic Electron and Pion Data and GEANT4 Validation

This thesis presents the analysis of electron data between 1 GeV and 20 GeV beam momentum and pion data between 1 GeV and 30 GeV beam momentum collected with the AHCAL physics prototype with particles impinging directly on this detector. This is the first analysis of AHCAL data using data recorded at Fermilab and the newly obtained calibration factors. Furthermore, this is the first analysis based on this calorimeter extending to energies below 8 GeV. Therefore, understanding the detector behavior and event selections at low energies, as well as the calibration of a data sample collected under different operating conditions and with a different experimental setup than previously analyzed data samples, are an integral part of this analysis.

A procedure is developed to quantify the purity of the analyzed data samples. According to this procedure, the Čerenkov tagging and additional offline event selection criteria yield electron samples with purities above 99.95% at all covered energies and pion samples with purities above 99% at 8 GeV and above. The contributions of residual electron contaminations of pion data at lower beam momenta are subtracted statistically from all analyzed observables. Due to uncertainties about the contamination, the pion data at 1 GeV are excluded from the subsequent analysis.

The linearity of the AHCAL response to electrons and the energy resolution for electrons extracted for the low-energetic electron data agree with the results from previous measurements at higher energies within uncertainties. The MIP/GeV conversion factor is determined as $u = (42.0 \pm 0.5)\,\frac{\text{MIP}}{\text{GeV}}$ with an offset of $v = (-0.8 \pm 1.0)\,\text{MIP}$. The resolution extracted from these data has a stochastic term of $(21.5 \pm 0.2)\,\%/\sqrt{E[\text{GeV}]}$ and a constant term of $(0.0 \pm 1.2)\%$ for a fixed noise term of 40 MeV.

The obtained results for the maxima of the longitudinal shower profiles for low-energetic electron data and simulations agree within uncertainties and are consistent with the results

from high-energy positron data, whereas the visible energies predicted by Monte Carlo simulations show a larger negative offset than observed in data. This offset with respect to data hints to an inaccurate description of detector effects in the simulation. However, this part of the analysis shows that detector calibration and simulation are well enough under control to analyze pion data and to validate pion simulations.

The comparison of the results obtained for the low-energetic pion data with results from previous studies based on pion data from 8 GeV to 80 GeV beam momentum indicate that the scale of the detector response is most difficult to reproduce with different experimental setups, operating conditions, and calibrations. In contrast to this, observables related to the shower shape in longitudinal or radial direction agree well.

The analyzed pion data are used to validate several GEANT4 models and physics lists for the simulation of hadron physics between 2 GeV and 30 GeV pion momentum. This energy range covers the validity limits of several models and transition regions between models combined to physics lists. The comparisons between data and simulations extend from the mean deposited energy to the longitudinal and radial pion shower shapes and the means and standard deviations of the energy depositions in longitudinal and radial direction.

From 2 GeV to 8 GeV, the Bertini cascade model shows the best agreement with data for all observables which are compared. Between 12 GeV and 30 GeV, the CHIPS model yields the best agreement with data for all these parameters. This result shows a significant improvement of the CHIPS model in the used version 9.4 of GEANT4 with respect to previous versions.

The FTFP_BERT physics list describes the measured pion response within 5% over the full energy range covered by this analysis. Taking into account the absolute energy scale uncertainty of 5%, FTFP_BERT gives best overall performance for predicting the AHCAL response to pions. In addition, the FTFP_BERT physics list is the best performing physics list for predicting longitudinal pion cascades shapes between 2 GeV and 30 GeV and predicts the mean shower depth within 3% and the shower length within 5% in this energy range.

The QGSP_BERT physics list shows the best overall performance in predicting the radial profiles of pion cascades between 2 GeV and 30 GeV and underestimates the radius by less than 5% and the radial standard deviation by less than 2% up to 12 GeV and by 10% (mean) and 5% (standard deviation) at 30 GeV.

This analysis yields the same results for the QGSP_BERT physics list with or without using the high precision extension, which is attributed to the signal shaping time of the AHCAL (included as time-cut of 150 ns in the simulation) removing contributions from late energy depositions. The QBBC physics list, which has not been validated with CALICE data before, shows a similar agreement with data as FTFP_BERT and QGSP_BERT in the covered energy range.

Outlook

The measurements conducted at Fermilab in 2008 and 2009 conclude the AHCAL physics prototype program. In addition to the physics prototypes, CALICE constructs engineering prototypes [91] to demonstrate the feasibility to build a full-scale ILD detector segment and to gain insights into the production process, the allowed tolerances, and the overall

costs of building such a detector. Furthermore, these prototypes employ a new generation of integrated electronics.

The effects of the signal threshold on the AHCAL response need further investigation. The difference of the linearity offset observed for electron data and simulations is attributed to these effects and may be due to an inaccurate description of detector effects in the simulation or a result of predictions of the radial extension of electromagnetic cascades deviating from reality. Understanding the threshold effects is also important because they directly affect the observed $\frac{e}{\pi}$ ratio and the calibration of AHCAL data to an absolute energy scale.

The good performance of the Bertini cascade model in describing hadron showers at low energies and the good agreement between CHIPS and data at high energies suggest trying a new physics list combining these two models. Another step for continuing the pion analysis presented in this thesis could be a closer look at the cascade development behind the first inelastic scattering process by locating this interaction and comparing the energy deposited close-by between data and simulations. In addition, splitting energy depositions not only by electromagnetic and hadronic components, but according to the processes that generate the secondaries that eventually deposit the energy, may give clear hints about the origin of the differences between the predictions made by individual models. The measurement uncertainties at 6 GeV and below could be reduced and the analysis extended to 1 GeV if future event selection algorithms are capable of efficiently separating electron from pion events or if the purity of these data samples is estimated with better accuracy.

The data recorded at Fermilab allow for a variety of other analyses like the evaluation of the performance of the integrated detector setup with electromagnetic calorimeter, hadron calorimeter, and tail catcher and the application of Particle Flow algorithms to real data at low energies. The analysis presented in this thesis and the developed procedures form a basis for future analyses exploiting the full potential of these data.

Appendix A

Beam-line Simulation

The simulation of the CALICE test-beam setup presented in this thesis uses Mokka in version 7.06 and the model TBFnal0508_p0709. This model describes the CALICE test-beam setup and beam line instrumentation (drift chambers and scintillators) as described in Section 3.2 (Fig. 3.3 is a visualization of the geometry implemented in the simulation). The material upstream from the CALICE setup is not included (between $0.08 - 0.16\,X_0$, see Section 3.1). Data and simulations use a common coordinate system with the origin at the center of the backplane of the most downstream drift chamber.

The Geant4 particle gun generates primary particles (with defined type, momentum, position, and direction) for simulations. Unless stated otherwise, the Geant4 particle gun is placed 10 cm in front of the AHCAL physics prototype (at $z = 1432\,\text{mm}$) for the simulations presented in this thesis. The momentum uncertainty in the simulation is set to zero.

Placing the particle gun right in front of the AHCAL neglects the material from the CALICE beam line instrumentation in the simulation. Therefore, the difference between the material in the beam line in data and in simulations adds up to values between $0.17\,X_0$ and $0.25\,X_0$ (see Sections 3.1 and 3.2). Figure A.1 shows the ratio of the electron response for the particle gun positioned in front of the AHCAL (at $z = 1432\,\text{mm}$) and at the beginning of the CALICE setup (at $z = -4100\,\text{mm}$), which adds about 0.1 X0 material. The effect of the increased distance and the additional material on the electron response of the AHCAL is 1% at 1 GeV and becomes less for higher electron momenta. After traversing 0.1 X0, an electron looses on average about 10% of its energy due to bremsstrahlung (see Section 1.1.1). The bremsstrahlung-photons are strongly boosted in forward direction and are measured in the AHCAL together with the primary electron. The total energy deposited in the AHCAL is not reduced. At low momenta, the boost of the bremsstrahlung-photons decreases and the fraction of the electron energy that does not reach the AHCAL increases. In addition, the first absorber plate of the AHCAL is more transparent for high-energetic bremsstrahlung-photons for which the dominant interaction process is pair production (mean free path length about 1.5 AHCAL layers, see Chapter 1), while photons of lower energies are absorbed due to different processes and do not reach the first sensitive AHCAL layer. Placing the particle gun in front of the AHCAL instead of accounting for all beam line material increases the visible in the AHCAL by about 1%. The beam line material does not affect the simulated AHCAL response to pions because pions pass

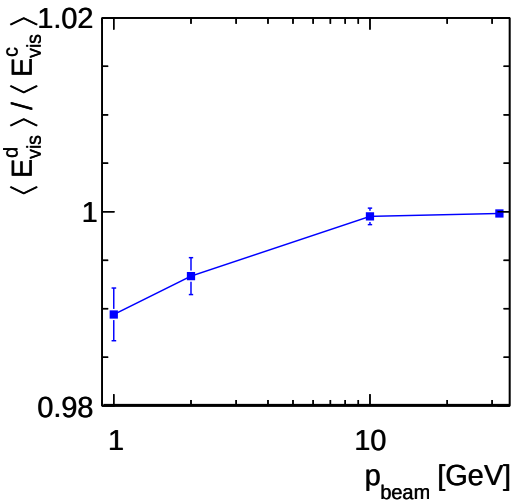

Figure A.1: Change of the mean simulated AHCAL response to electrons due to placing the particle gun upstream of the CALICE beam line instrumentation ($\langle E^d_{\text{vis}} \rangle$) rather than directly in front of the calorimeter ($\langle E^c_{\text{vis}} \rangle$, all material in the beam line is neglected).

the material as minimum-ionizing particles. Pions interacting strongly with the material upstream of the AHCAL are excluded by the event selection (see Section 6.4).

The transverse position of the particle gun in the simulation is at the nominal beam axis, i.e. at $x = 0$ and $y = 0$. Because the transverse profile of the MTest beam is approximately Gaussian, the transverse particle gun position is smeared with a Gaussian distribution. The mean center of gravity in x- and y-direction measured in the AHCAL gives the beam impact position on the AHCAL during data collection. The impact position varies because the AHCAL stage allows for moving the detector to different positions (see Section 3.2). The simulated AHCAL is displaced in x- and y-direction to match the beam impact position in data and simulations. The standard deviation from the measured center of gravity in x- and y-direction is used as sigma for the Gaussian position smearing of the particle gun. The AHCAL displacement and the beam spread are determined independently for each detector position, beam momentum, and particle type. The information from the drift chambers is not available for analysis yet. Figures A.2(a), A.2(b), A.2(c), and A.2(d) show the center of gravity in x- and y-direction for electron data and fully digitized Monte Carlo simulation at 10 GeV and 2 GeV. The distributions reflect the increase of the width of the electron beam used to collect the data with decreasing beam momentum. The peak structure is an artifact of the AHCAL tile size and the distance of the peaks corresponds to the width of a tile, i.e. 30 mm. Each energy deposition in a tile is assigned to the center of the tile. The agreement between data and simulations is very good.

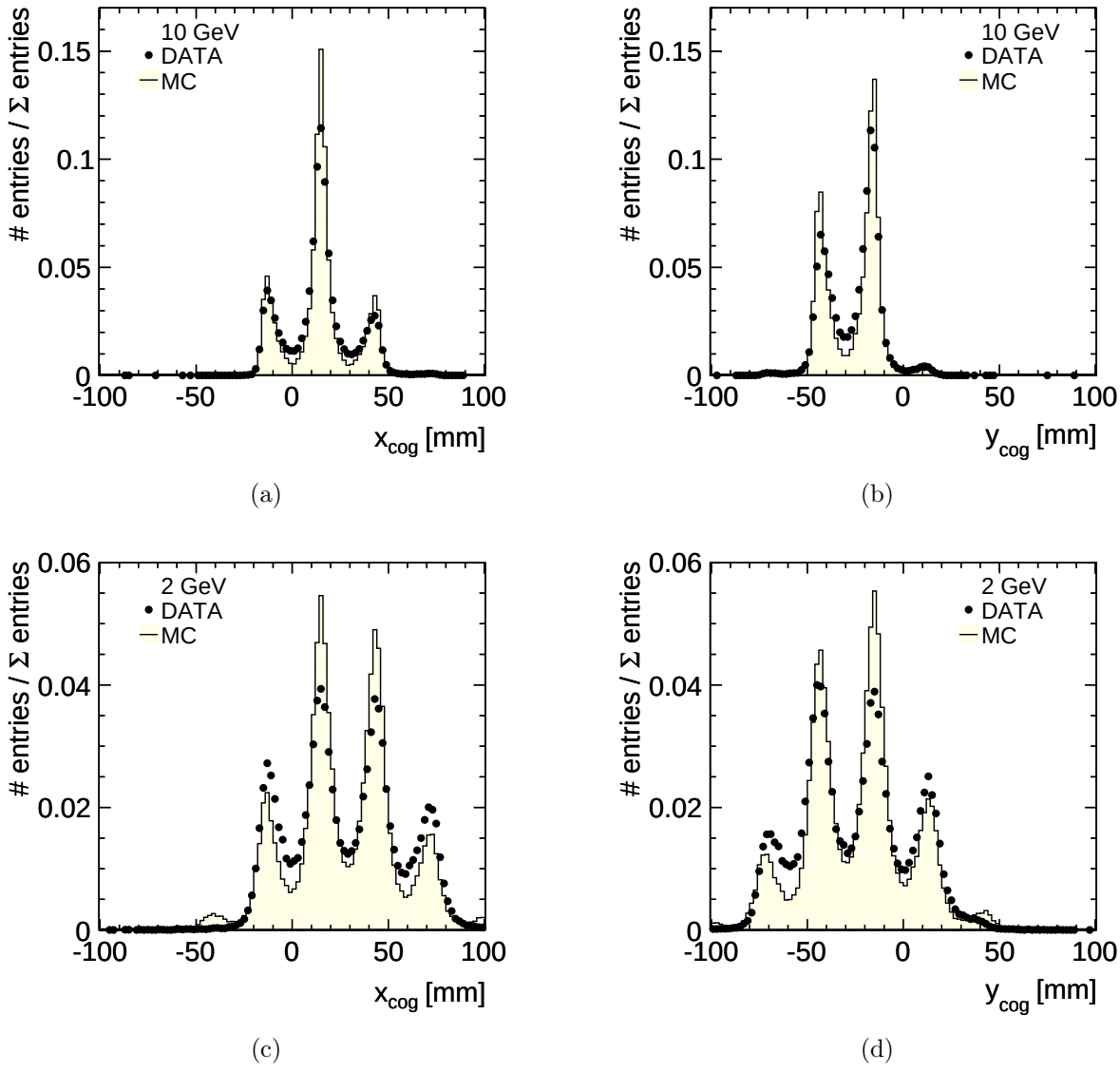

(a) (b)

(c) (d)

Figure A.2: Center of gravity of the AHCAL response to electrons in data (points) and fully digitized simulations (histograms) in (a) x-direction at 10 GeV, (b) y-direction at 10 GeV, (c) x-direction at 2 GeV, and (d) y-direction at 2 GeV beam momentum.

Appendix B

Performance of Applied Algorithms

This section evaluates the performance of the AHCAL and TCMT based tracking algorithms and the clustering algorithm for the AHCAL presented in Section 6.1.

AHCAL and TCMT Tracking

The muon selection efficiency depends on the chosen threshold for the number of hits in a single tower. Closing the MTest beam dump provides a clean 32 GeV muon sample for estimating the efficiency from data (see Section 3.1). For the AHCAL, requiring at least 30 hits yields an efficiency of 79.2% for detecting muons in data. For digitized Monte Carlo simulations, the same threshold yields a muon detection efficiency of 98.5%. The smaller efficiency in data compared to simulations is attributed to the mismatch between the area covered by the sensitive AHCAL layers ($0.72\,\mathrm{m}^2$) and the area of the scintillators used for triggering the data acquisition ($1\,\mathrm{m}^2$, the beam intensity is higher in the center than at the edges). All simulated muons hit the AHCAL. In addition, some muons from the MTest beam hit the AHCAL at a non-orthogonal angle and the track hits are split between two or more towers, whereas the incident angle of all simulated muons is orthogonal to the AHCAL layers. For the TCMT, requiring at least 8 hits in a single tower yields a muon selection efficiency of 91.9% for data and 96.4% for simulations. The efficiencies obtained from data and simulations agree better for the TCMT than for the AHCAL because the sensitive layers of the TCMT ($1\,\mathrm{m}^2$) cover the full trigger area.

For more than 99% of the muon tracks from simulated muons of 20 GeV and above that are identified by the TCMT tracking algorithm, the lateral position determined by the algorithm agrees with the true muon position within ± 1 TCMT tower. The wrong position measurements are due to noise hits in the TCMT. The performance of the TCMT tracking algorithms is sufficient for measuring muon positions in data to estimate the muon identification efficiency of other detectors or algorithms (e.g. the veto wall, see Section 6.2).

AHCAL Clustering and Locating the First Inelastic Hadron Interaction

Figure B.1(a) presents the efficiency of finding the z-position of the first inelastic scattering correctly within ± 1 layer for different pion momenta and different physics lists (only events for which an inelastic scattering is found in the AHCAL are considered). The efficiency is 75-80% at 6 GeV and above and drops down to 65% below. Figure B.1(b) shows the

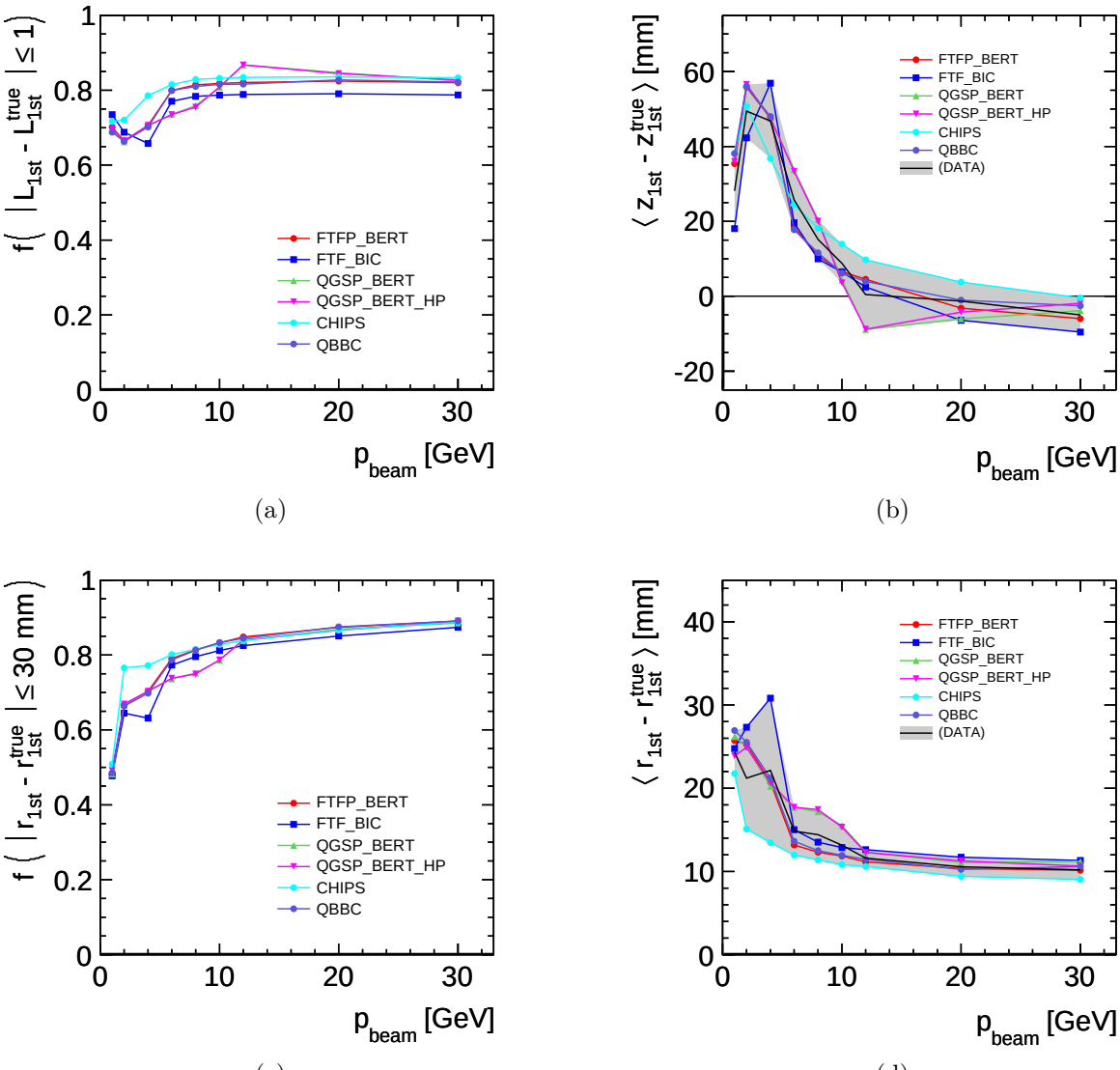

Figure B.1: Fraction f of events at different pion momenta for which the first hard interaction located by the clustering algorithm is in the same or adjacent (a) layer or (c) radial bin (30 mm) as the end point of the simulated pion. Mean difference between (b) the z-position or (d) the radial position of the first hard interaction located by the clustering algorithm and the corresponding position of the end point of the simulated pion as a function of the pion momentum.

TABLE I
OFFSETS FOR THE FIRST INELASTIC HADRON INTERACTION LOCATED IN DATA.

p_{beam} [GeV]	Δ_{z} [mm]	Δ_{r} [mm]
1	28 ± 10	24 ± 3
2	49 ± 7	21 ± 6
4	47 ± 10	22 ± 9
6	26 ± 8	15 ± 3
8	15 ± 5	14 ± 3
10	9 ± 5	13 ± 2
12	0 ± 9	12 ± 1
20	-1 ± 5	11 ± 1
30	-5 ± 5	10 ± 1

mean difference between the z position z_{1st} of the first hard interaction identified by the clustering algorithm and the true position $z_{\text{1st}}^{\text{true}}$ provided by the simulation as a function of the beam momentum for various physics lists. Knowing this difference, or offset, allows to correct the position extracted from the clustering algorithm for this offset. However, the difference between the true starting point of the cascade and the measured position is not known for data. Therefore, the center value for all physics lists (it is not known which physics list describes the difference best for data) is taken as best offset estimate for data (black line in Fig. B.1(b)). Half of the maximum difference between the predictions from different physics lists at a given pion momentum is used as uncertainty for the difference in data and is illustrated by the shaded area in Fig. B.1(b). At 6 GeV and above, the mean offset is smaller than the thickness of an AHCAL layer (3 cm). Table I summarizes the estimated offsets Δ_{z} for data.

Figures B.1(c) and B.1(d) present the efficiency of finding the radial position $r = \sqrt{x^2 + y^2}$ correctly within ± 30 mm (smallest AHCAL cell size) and the mean radial offset between the identified and the true cascade start for different beam momenta and different physics lists. Analog to the z offset, the central offset of all Monte Carlo predictions is taken as mean radial offset Δ_{r} for data. Half the maximum difference between the predictions from different physics lists at a given beam momentum gives the uncertainty of this offset. The values for Δ_{r} are listed in Table I. At 6 GeV and above, the mean radial offset is smaller than half the extension of a single AHCAL cell (30 mm).

This cluster-based algorithm is capable of locating the three dimensional position of the first inelastic hadron interaction in the AHCAL at 6 GeV and above with a mean precision of the order of the detector granularity (1 layer in z-direction, 1 cell in x- and y-direction). Appendix C presents the efficiency of this algorithm for locating any hard interaction in the AHCAL for simulated pion events of different beam momenta. The efficiency is higher than 98% for beam momenta of 4 GeV and above and drops to 65% at 2 GeV and 27% at 1 GeV. Therefore, this algorithm is only considered applicable for locating the first inelastic hadron interaction for pions with momenta of 4 GeV and above. The efficiency drop at 2 GeV and 1 GeV is attributed to the lower average energy density at lower pion momenta.

Appendix C

Event Selection Efficiencies

Table I summarizes several studied event selection criteria for electrons, where $z_{\mathrm{cog}}^{\mathrm{AHCAL}}$ is the longitudinal center of gravity in the AHCAL, E_{i-j}^{AHCAL} is the total visible energy in AHCAL layers i to j, $E_{\mathrm{cluster}}^{\mathrm{AHCAL}}$ is the energy assigned to a single AHCAL cluster, and $N_{\mathrm{cluster}}^{\mathrm{AHCAL}}$ is the number of cells contributing to a single AHCAL cluster. Figures C.1(a) and C.1(b) present the selection efficiencies (fraction of events passing the cut) for simulated electron and muon events (after digitization) at different beam momenta for the individual event selection criteria. Cut e-1 is applied for selecting electron events all beam momenta, while cuts e-3 and e-5 are only used for 1 GeV electrons and e-2 and e-4 are used from 2 GeV to 20 GeV.

Table II summarizes several studied event selection criteria for pions, where E^{TCMT} is the visible energy in the TCMT, $N_{\mathrm{track}}^{\mathrm{TCMT}}$ is the number of strips contributing to the longest track found in the TCMT, $N_{\mathrm{track}}^{\mathrm{AHCAL}}$ is the number of cells contributing to the longest track found in the AHCAL, $L_{\mathrm{1st}}^{\mathrm{AHCAL}}$ is the layer of the located first inelastic scattering, N^{AHCAL} is the number of hits in the AHCAL, and $E_{\mathrm{i-j}}^{\mathrm{AHCAL}}$ is the total visible energy in AHCAL layers i to j.

Figures C.2(a) and C.2(b) present the efficiencies of selection criteria π-1 to π-5 for simulated pion and muon events as a function of the beam momentum. A simple cut on the TCMT energy sum E^{TCMT} (cut π-1) excludes most muon events, but also lets only

Table I
Cuts for electron selection.

Cut	Description
e-1	$z_{\mathrm{cog}}^{\mathrm{AHCAL}} < 1892\,\mathrm{mm}$
e-2	$E_{29-38}^{\mathrm{AHCAL}} < 5\,\mathrm{MIP}$
e-3	$E_{19-38}^{\mathrm{AHCAL}} < 8\,\mathrm{MIP}$
e-4	$E_{\mathrm{cluster}}^{\mathrm{AHCAL}} \geq 18\,\mathrm{MIP} \wedge N_{\mathrm{cluster}}^{\mathrm{AHCAL}} \geq 2$
e-5	$E_{\mathrm{cluster}}^{\mathrm{AHCAL}} \geq 6\,\mathrm{MIP} \wedge N_{\mathrm{cluster}}^{\mathrm{AHCAL}} \geq 2$

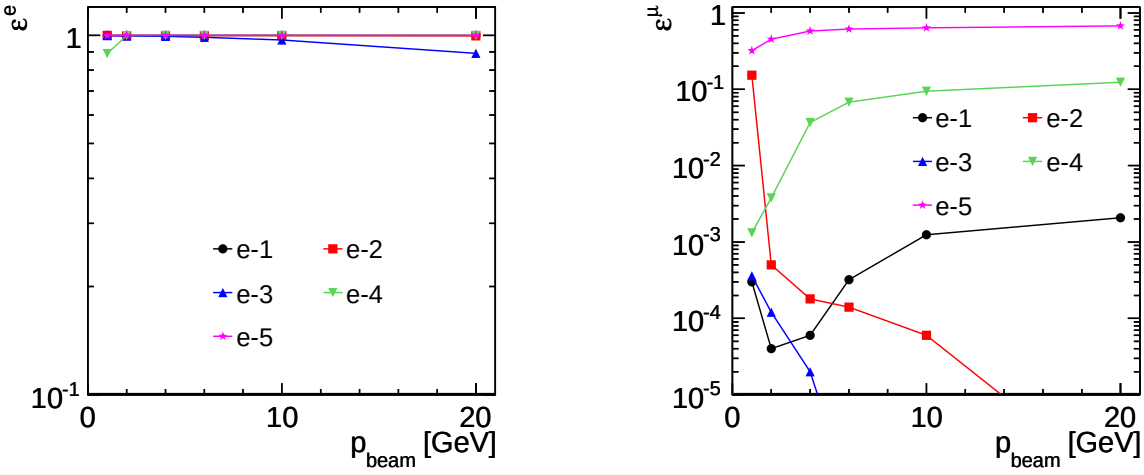

(a) (b)

Figure C.1: Selection efficiency for electrons (a) and muons (b) for various event selection criteria used to purify the electron data samples at different beam momenta. The efficiencies are estimated from digitized Monte Carlo simulations using the FTFP_BERT physics list.

few pion events pass. The TCMT tracking algorithm (explained in Section 6.1) yields higher pion selection efficiencies at comparable muon selection efficiencies compared to the AHCAL tracking algorithm (cut π-4, $N_{\text{track}}^{\text{TCMT}}$ is the number of hits in the maximum tower).

Figures C.2(a) and C.2(b) present the efficiencies of selection criteria π-4, π-6, and π-7, and π-8 for simulated pion and muon events as a function of the beam momentum for beam momenta between 1 GeV and 10 GeV. The pion selection efficiency for 4 GeV pions is larger for cut π-4 than for cut π-8 while the muon selection efficiency is smaller. Therefore, cut π-4 is used at this beam momentum.

Muons from pion decays in the beam line after the last bending magnet and collimator have smaller momenta than the initial pions. Therefore, the selection efficiencies estimated in this section with muons of the same momentum as pions overestimates the overall muon rejection power of these cuts. Furthermore, the effect of multiple scattering becomes more important at low momenta and causes muons to traverse the AHCAL at non-orthogonal angles. Since the muon cuts are tested for muons impinging orthogonally on the AHCAL, this is another overestimate.

Cut π-4 is used from 4 GeV to 30 GeV. From 8 GeV to 30 GeV, cut π-5 is used in addition. At 1 GeV only cut π-6 and at 2 GeV only cut π-7 is applied.

TABLE II
CUTS FOR PION SELECTION.

Cut	Description
π-1	$E^{\mathrm{TCMT}} < 12\,\mathrm{MIP}$
π-2	$N^{\mathrm{TCMT}}_{\mathrm{track}} < 8$
π-3	$N^{\mathrm{AHCAL}}_{\mathrm{track}} < 20$
π-4	$L^{\mathrm{AHCAL}}_{\mathrm{1st}} \geq 1 \wedge L^{\mathrm{AHCAL}}_{\mathrm{1st}} \leq 38$
π-5	$N^{\mathrm{AHCAL}} > 60$
π-6	$E^{\mathrm{AHCAL}}_{29-38} < 4\,\mathrm{MIP}$
π-7	$E^{\mathrm{AHCAL}}_{33-38} < 3\,\mathrm{MIP}$
π-8	$E^{\mathrm{AHCAL}}_{34-38} < 5\,\mathrm{MIP}$

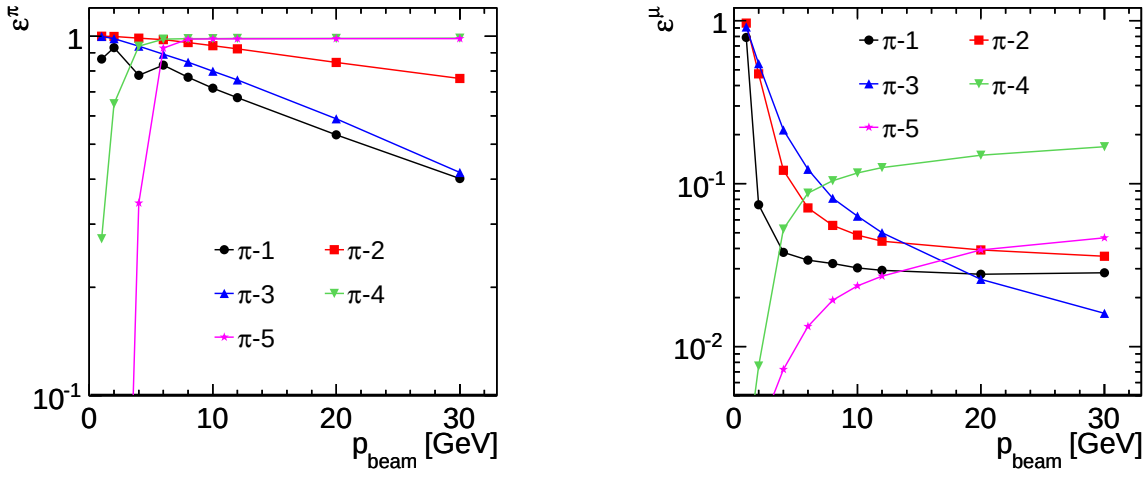

(a) (b)

Figure C.2: Selection efficiency for pions (a) and muons (b) for various event selection criteria used to purify the pion data samples at different beam momenta. The efficiencies are estimated from digitized Monte Carlo simulations using the FTFP_BERT physics list.

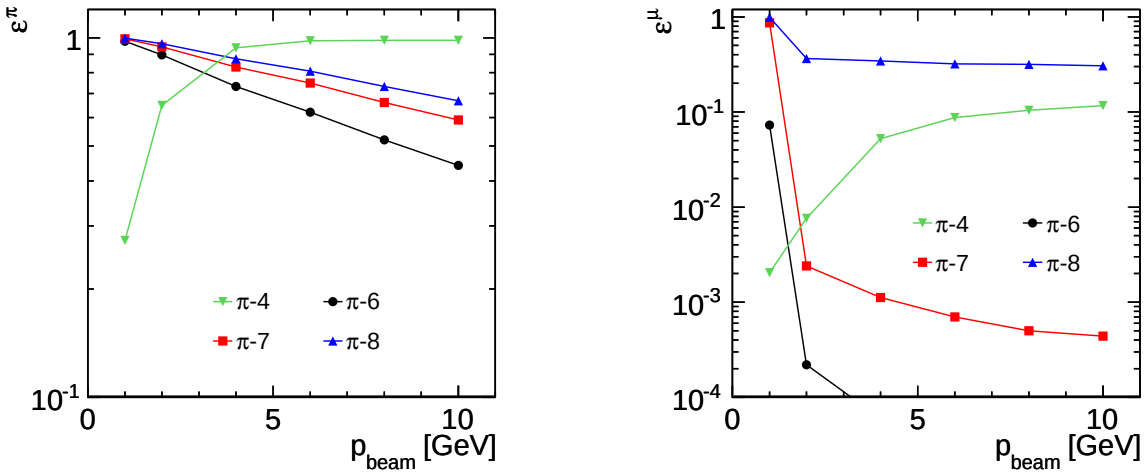

(a) (b)

Figure C.3: Selection efficiency for pions (a) and muons (b) for various event selection criteria used to reduce the muon contamination of pion data at beam momenta between 1 GeV and 10 GeV. The efficiencies are estimated from digitized Monte Carlo simulations using the FTFP_BERT physics list.

Appendix D

Supplementary Tables

Table I
Parameters extracted from electron data.

p_{beam} [GeV]	$\langle E^e_{\mathrm{rec}} \rangle$ [GeV]	$\sigma^e_{\mathrm{rec}}/\langle E^e_{\mathrm{rec}} \rangle$ [%]	t_{max} [X_0]
1	0.99 ± 0.03	22.9 ± 0.7	2.99 ± 0.02
2	2.04 ± 0.04	15.6 ± 0.3	3.72 ± 0.02
4	4.02 ± 0.07	10.8 ± 0.2	4.40 ± 0.01
6	6.1 ± 0.1	8.6 ± 0.2	4.77 ± 0.01
10	10.0 ± 0.2	6.7 ± 0.1	5.27 ± 0.01
20	19.5 ± 0.4	4.9 ± 0.1	6.02 ± 0.01
	Fig. 7.2(b)	Fig. 7.6	Fig. 7.9

Table II
Parameters extracted from pion data.

p_{beam} [GeV]	$\langle E^\pi_{\mathrm{rec}} \rangle$ [GeV]	$\langle Z \rangle$ [λ_{int}]	$\langle \sigma_z \rangle$ [λ_{int}]	$\langle R \rangle$ [mm]	$\langle \sigma_{\mathrm{R}} \rangle$ [mm]
2	1.35 ± 0.03	1.11 ± 0.02	0.706 ± 0.005	106 ± 2	93.8 ± 0.7
4	2.88 ± 0.06	1.31 ± 0.02	0.667 ± 0.007	99 ± 2	83.8 ± 0.8
6	4.68 ± 0.08	1.43 ± 0.02	0.688 ± 0.006	97 ± 1	85.6 ± 0.8
8	6.3 ± 0.1	1.503 ± 0.003	0.676 ± 0.001	92.0 ± 0.1	83.0 ± 0.1
10	8.0 ± 0.1	1.563 ± 0.003	0.681 ± 0.001	88.5 ± 0.1	81.4 ± 0.1
12	9.7 ± 0.2	1.611 ± 0.002	0.685 ± 0.001	85.4 ± 0.1	80.3 ± 0.1
20	16.5 ± 0.4	1.738 ± 0.003	0.701 ± 0.001	78.7 ± 0.1	78.0 ± 0.1
30	25.0 ± 0.7	1.830 ± 0.003	0.713 ± 0.001	73.7 ± 0.1	76.0 ± 0.1
	Fig. 8.5(a) Fig. 8.5(b) Fig. 8.2	Fig. 8.9(a) Fig. 8.9(b)	Fig. 8.9(c) Fig. 8.9(d)	Fig. 8.12(a) Fig. 8.12(b)	Fig. 8.12(c) Fig. 8.12(d)

Tables I and II list the parameters obtained within this analysis from the low-energetic electron and pion data collected with the AHCALphysics prototype at Fermilab. The parameters, their extraction, and their uncertainties are discussed in Chapters 7 and 8. The tables also provide references to the figures which visualize the respective values.

Bibliography

[1] A. Salam, "Elementary Particles," *Contemp. Phys.*, vol. 1, pp. 337–354, 1959.

[2] S. Glashow, "Partial Symmetries of Weak Interactions," *Nucl. Phys.*, vol. 22, pp. 579–588, 1961.

[3] S. Weinberg, "A Model of Leptons," *Phys. Rev. Lett.*, vol. 19, pp. 1264–1266, 1967.

[4] L. Evans and P. Bryant, "LHC Machine," *JINST*, vol. 3, p. S08001, 2008.

[5] J. Brau *et al.*, "International Linear Collider Reference Design Report (1: Executive Summary, 2: Physics at the ILC, 3: Accelerator, 4: Detectors)," 2007, `ILC-REPORT-2007-001`.

[6] T. Abe *et al.*, "The International Large Detector: Letter of Intent," 2010.

[7] S. Agostinelli *et al.*, "GEANT4: A Simulation Toolkit," *Nucl. Instrum. Meth.*, vol. A506, pp. 250–303, 2003.

[8] R. Wigmans, *Calorimetry*, 1st ed. Oxford University Press, 2000.

[9] C. Leroy and P. Rancoita, "Physics of Cascading Shower Generation and Propagation in Matter: Principles of High-energy, Ultrahigh-energy and Compensating Calorimetry," *Rept. Prog. Phys.*, vol. 63, pp. 505–606, 2000.

[10] K. Nakamura *et al.*, "Review of Particle Physics," *J. Phys.*, vol. G37, p. 075021, 2010.

[11] T. A. Gabriel *et al.*, "Energy Dependence of Hadronic Activity," *Nucl. Instrum. Meth.*, vol. A338, pp. 336–347, 1994.

[12] D. E. Groom, "Energy Flow in a Hadronic Cascade: Application to Hadron Calorimetry," *Nucl. Instrum. Meth.*, vol. A572, pp. 633–653, 2007.

[13] A. Stirling *et al.*, "Small-angle Charge Exchange of pi- Mesons between 6 and 18 GeV/c," *Phys. Rev. Lett.*, vol. 14, pp. 763–767, 1965.

[14] A. Barnes *et al.*, "Pion Charge Exchange Scattering at High Energies," *Phys. Rev. Lett.*, vol. 37, p. 76, 1976.

[15] U. Amaldi, "Fluctuations in Calorimetry Measurements," *Phys. Scripta*, vol. 23, p. 409, 1981.

[16] R. Wigmans, "The DREAM Project: Results and Plans," *Nucl. Instrum. Meth.*, vol. A572, pp. 215–217, 2007.

[17] R. Wigmans, "The DREAM Project: Towards the Ultimate in Calorimetry," *Nucl. Instrum. Meth.*, vol. A617, pp. 129–133, 2010.

[18] A. Driutti *et al.*, "Towards Jet Reconstruction in a Realistic Dual Readout Total Absorption Calorimeter," *J. Phys. Conf. Ser.*, vol. 293, p. 012034, 2011.

[19] C. Fabjan *et al.*, "Iron Liquid-argon and Uranium Liquid-argon Calorimeters for Hadron Energy Measurement," *Nucl. Instrum. Meth.*, vol. 141, p. 61, 1977.

[20] T. Akesson *et al.*, "Properties of a Fine Sampling Uranium-copper Scintillator Hadron Calorimeter," *Nucl. Instrum. Meth.*, vol. A241, p. 17, 1985.

[21] T. Akesson *et al.*, "Performance of the Uranium / Plastic Scintillator Calorimeter for the Helios Experiment at CERN," *Nucl. Instrum. Meth.*, vol. A262, p. 243, 1987.

[22] P. Adzic *et al.*, "Energy Resolution of the Barrel of the CMS Electromagnetic Calorimeter," *JINST*, vol. 2, p. P04004, 2007.

[23] I. Park, "Experience with the ZEUS Calorimeter," in *Proc. Beijing Calorimetry Symposium*, Beijing, China, Oct. 1994.

[24] J.-C. Brient and H. Videau, "The Calorimetry at the Future e+ e- Linear Collider," in *Proc. APS/DPF/DPB Summer Study on the Future of Particle Physics (Snowmass 2001)*, Colorado, Jul. 2001.

[25] V. L. Morgunov, "Calorimetry Design with Energy-flow Concept (Imaging Detector for High-energy Physics)," in *Proc. Tenth International Conference Pasadena*, California, Mar. 2002.

[26] M. A. Thomson, "Particle Flow Calorimetry and the PandoraPFA Algorithm," *Nucl. Instrum. Meth.*, vol. A611, pp. 25–40, 2009.

[27] F. Simon, "Particle Showers in a Highly Granular Hadron Calorimeter," *J. Phys. Conf. Ser.*, vol. 293, p. 012073, 2011.

[28] M. Groll, "Construction and Commissioning of a Hadronic Test-Beam Calorimeter to Validate the Particle-Flow Concept at the ILC," Ph.D. dissertation, University of Hamburg, 2007, `DESY-THESIS-2007-018`.

[29] B. Lutz, "Hadron Showers in a Highly Granular Calorimeter," Ph.D. dissertation, University of Hamburg, 2010, `DESY-THESIS-2010-048`.

[30] A. Kaplan, "Hadronic Imaging Calorimetry," Ph.D. dissertation, University of Heidelberg, 2010.

[31] C. Adloff *et al.*, "Construction and Commissioning of the CALICE Analog Hadron Calorimeter Prototype," *JINST*, vol. 5, p. P05004, 2010.

[32] J. Repond *et al.*, "Design and Electronics Commissioning of the Physics Prototype of a Si-W Electromagnetic Calorimeter for the International Linear Collider," *JINST*, vol. 3, p. P08001, 2008.

[33] C. Adloff *et al.*, "Electromagnetic response of a highly granular hadronic calorimeter," *JINST*, vol. 6, p. P04003, 2011.

[34] G. Bondarenko *et al.*, "Limited Geiger-mode Microcell Silicon Photodiode: New Results," *Nucl. Instrum. Meth.*, vol. A422, pp. 187–192, 2000.

[35] P. Buzhan *et al.*, "An Advanced Study of Silicon Photomultiplier," *ICFA Instrum. Bull.*, vol. 23, p. 28, 2001.

[36] P. Buzhan *et al.*, "Silicon Photomultiplier and its Possible Applications," *Nucl. Instrum. Meth.*, vol. A504, pp. 48–52, 2003.

[37] N. Feege, "Silicon Photomultipliers: Properties and Application in a Highly Granular Calorimeter," Diploma thesis, University of Hamburg, 2008, `DESY-THESIS-2008-050`.

[38] K. Kotera, "First Stage Analysis of the Energy Response and Resolution of the Scintillator ECAL in the Beam Test at FNAL, 2008," CALICE analysis note 16, May 2010.

[39] K. Francis, "Results of Beam Tests of a Prototype Calorimeter for a Linear Collider," Ph.D. dissertation, Norther Illinois University, 2010.

[40] M. Yokoyama *et al.*, "Development of Multi-Pixel Photon Counters," in *Proc. International Symposium On Detector Development For Particle, Astroparticle And Synchrotron Radiation Experiments*, California, Apr. 2006.

[41] S. Gomi *et al.*, "Development and Study of the Multi Pixel Photon Counter," *Nucl. Instrum. Meth.*, vol. A581, pp. 427–432, 2007.

[42] B. Dolgoshein *et al.*, "Status Report on Silicon Photomultiplier Development and its Applications," *Nucl. Instrum. Meth.*, vol. A563, pp. 368–376, 2006.

[43] M. Danilov, "Scintillator Tile Hadron Calorimeter with Novel SiPM Readout," *Nucl. Instrum. Meth.*, vol. A581, pp. 451–456, 2007.

[44] L. Landau, "On the Energy Loss of Fast Particles by Ionization," *J. Phys. (USSR)*, vol. 8, pp. 201–205, 1944.

[45] CALICE, "Muon Calibration and Portability of Calibration Constants in a Highly Granular Hadron Calorimeter," in preparation.

[46] C. Adloff *et al.*, "Tests of a Particle Flow Algorithm with CALICE Test Beam Data," *JINST*, vol. 6, p. P07005, 2011.

[47] C. Adloff *et al.*, "Response of the CALICE Si-W Electromagnetic Calorimeter Physics Prototype to Electrons," *Nucl. Instrum. Meth.*, vol. A608, pp. 372–383, 2009.

[48] C. Adloff *et al.*, "Study of the Interactions of Pions in the CALICE Silicon-tungsten Calorimeter Prototype," *JINST*, vol. 5, p. P05007, 2010.

[49] J. Apostolakis *et al.*, "Validation of GEANT4 Hadronic Models Using CALICE Data," `EUDET-MEMO-2010-15`.

[50] E. Ramberg, "A broad Energy Range Detector Test Beam Facility at Fermilab," in *Proc. IEEE Nuclear Science Symposium and Medical Imaging Conference (NSS MIC 07)*, Honolulu, Hawaii, Oct. 2007.

[51] The Fermilab Test Beam Facility. [Online]. Available: http://www-ppd.fnal.gov/FTBF

[52] M. Popovic *et al.*, "Fermilab Linac Injector, Revisited," in *Proc. 16th IEEE Particle Accelerator Conference (PAC 95) and International Conference on High-energy Accelerators (IUPAP)*, Dallas, Texas, May 1995.

[53] J. Lackey *et al.*, "Operation and Performance of the New Fermilab Booster H^- Injection System," in *Proc. Particle Accelerator Conference (PAC 07)*, Albuquerque, New Mexico, Jun. 2007.

[54] R. Coleman, private communication.

[55] H. C. Fenker, "A Standard Beam PWC for Fermilab," `FERMILAB-TM-1179`.

[56] T. Ikuno, private communication.

[57] CALICE, "The Scintillator-ECAL Beam Test at DESY in 2007 - Update 1," CALICE analysis note 6, Oct. 2007.

[58] J. Litt and R. Meunier, "Cerenkov Counter Tchnique in High-energy Physics," *Ann. Rev. Nucl. Part. Sci.*, vol. 23, pp. 1–44, 1973.

[59] B. Lang *et al.*, "The Use of Cerenkov Counters at MTEST," 2004. [Online]. Available: http://www-ppd.fnal.gov/FTBF/Facility/Inst_Cerenkov/cc_mtest.pdf

[60] P. S. Auchincloss *et al.*, "A Study of the Energy Dependence of the Mean, Truncated Mean, and Most Probable Energy Deposition of High-energy Muons in Sampling Calorimeters," *Nucl. Instrum. Meth.*, vol. A343, pp. 463–469, 1994.

[61] W. Lohmann *et al.*, "Energy Loss of Muons in the Energy Range 1 GeV to 10000 GeV," `CERN-85-03`.

[62] M. Ramilli, private communication.

[63] V. Ivanchenko *et al.*, "Recent Improvements in GEANT4 Electromagneticx Physics Models and Interfaces," in *Proc. Joint International Conference on Supercomputing in Nuclear Applications and Monte Carlo 2010*, 2010.

[64] V. Ivanchenko *et al.*, "GEANT4 Models for Simulation of Multiple Scattering," in *Proc. Computing in High-energy and Nuclear Physics (CHEP 09)*, 2009.

[65] "GEANT4 Physics Reference Manual." [Online]. Available: http://cern.ch/geant4/UserDocumentation/UsersGuides/PhysicsReferenceManual/fo/PhysicsReferenceManual.pdf

[66] A. Heikinnen *et al.*, "Bertini Intra-nuclear Cascade Implementation in GEANT4," in *Proc. Computing in High-energy and Nuclear Physics (CHEP 03)*, 2003.

[67] J. Wellisch and G. Folger, "The Binary Cascade," in *Proc. Computing in High-energy and Nuclear Physics (CHEP 04)*, 2005.

[68] G. Folger and J. Wellisch, "String Parton Models in GEANT4," in *Proc. Computing in High-energy and Nuclear Physics (CHEP 03)*, 2003.

[69] N. Amelin *et al.*, "Semihard Collisions in Monte Carlo Quark Gluon String Model," *Phys. Rev.*, vol. D46, pp. 4873–4881, 1992.

[70] B. Andersson *et al.*, "A Model for Low p(t) Hadronic Reactions, with Generalizations to Hadron-nucleus and Nucleus-nucleus Collisions," *Nucl. Phys.*, vol. B281, p. 289, 1987.

[71] B. Andersson, "The Fritiof Dynamics," invited talk at the Shandong Workshop on Multiparticle Production, Jinan, China, 1987.

[72] J. M. Quesada, "Recent Developements in Pre-equilibrium and De-excitation Models in GEANT4," in *Proc. Monte Carlo Conference (MC 10)*, 2010.

[73] H. Fesefeldt, "The Simulation of Hadronic Showers: Physics and Applications," 1985, `PITHA-85-02`.

[74] J. Apostolakis *et al.*, "GEANT4 Physics Lists for HEP," in *Nuclear Science Symposium Conference Record 2008 (NSS 08)*, Oct. 2008, pp. 833–836.

[75] A. Ribbon *et al.*, "Status of GEANT4 Hadronic Physics for the Simulation of LHC Experiments at the Start of LHC Physics Program," `CERN-LCGAPP-2010-02`.

[76] P. Adragna *et al.*, "Testbeam Studies of Production Modules of the ATLAS Tile Calorimeter," *Nucl. Instrum. Meth.*, vol. A606, pp. 362–394, 2009.

[77] E. Abat *et al.*, "Study of the Response of the ATLAS Central Calorimeter to Pions of Energies from 3 to 9 GeV," *Nucl. Instrum. Meth.*, vol. A607, pp. 372–386, 2009.

[78] P. Adragna *et al.*, "Measurement of Pion and Proton Response and Longitudinal Shower Profiles up to 20 Nuclear Interaction Lengths with the ATLAS Tile Calorimeter," *Nucl. Instrum. Meth.*, vol. A615, pp. 158–181, 2010.

[79] F. Simon, "Measurements of the Time Structure of Hadronic Showers in a Scintillator-Tungsten HCAL," in *Proc. Technology and Instrumentation in Particle Physics 2011 (TIPP 11)*, Jun. 2011.

[80] Mokka - a GEANT4 Application to Simulate the Full ILD Geometry. [Online]. Available: http://polzope.in2p3.fr:8081/MOKKA

[81] A. Lucaci-Timoce, "HCAL Prototype in the Test Beam Mokka Model." [Online]. Available: http://www.desy.de/~lucaci/Others/hcalTBeam.pdf

[82] J. B. Birks, *The Theory and Practice of Scintillation Counting*, 1st ed. Macmillan, 1964.

[83] M. Hirschberg *et al.*, "Precise Measurement of Birks kB Parameter in Plastic Scintillators," *IEEE Trans. Nucl. Sci.*, vol. 39, pp. 511–514, 1992.

[84] Marlin - Modular Analysis and Reconstruction for the Linear Collider. [Online]. Available: http://ilcsoft.desy.de/marlin

[85] S. Richter, "Validation of the Calibration Procedure for a Highly Granular Calorimeter with Electromagnetic Processes," Diploma thesis, University of Hamburg, 2008.

[86] R. Brun *et al.* ROOT Data Analysis Framework. [Online]. Available: http://root.cern.ch

[87] R. J. Barlow and C. Beeston, "Fitting Using Finite Monte Carlo Samples," *Comput. Phys. Commun.*, vol. 77, pp. 219–228, 1993.

[88] G. Barbiellini *et al.*, "Energy Resolution and Longitudinal Shower Development in a Si/W Electromagnetic Calorimeter," *Nucl. Instrum. Meth.*, vol. A235, p. 55, 1985.

[89] I. Marchesini, "Triple Gauge Couplings and Polarization at the ILC and Leakage in a Highly Granular Calorimeter," Ph.D. dissertation, University of Hamburg, 2011.

[90] S. Banerjee *et al.*, "Validation of GEANT4 Hadronic Generators versus Thin Target Data," in *Proc. Monte Carlo Conference (MC 10)*, 2010.

[91] M. Terwort, "Concept and Status of the CALICE Analog Hadron Calorimeter Engineering Prototype," 2011, in preparation.

Acknowledgments

Writing a dissertation is a demanding task, and I am indebted to all the people who have helped me during this process and throughout my research.

First of all, I would like to express my gratitude to my supervisor Prof. Dr. Erika Garutti, who gave me the unique opportunity to work on a project involving all the steps from the commissioning of a detector to the analysis of test-beam data. I thank her for her guidance, her motivating nature, many interesting and fruitful discussions, and all the confidence she put into my ability to successfully meet a large variety of challenges.

In addition, I thank Prof. Dr. Dieter Horns and Prof. Dr. Peter Schleper for examining my work, and Prof. Dr. Günter Huber for chairing my disputation. Besides, an honorable mention goes go to Mark, Clemens, Madalina, Beni, and Martina for extensively proof-reading the manuscript for this thesis.

It has been my pleasure to be a part of the CALICE collaboration and the FLC group at DESY and I am grateful to our group leaders Dr. Ties Behnke and Dr. Felix Sefkow, our secretaries Ramona Matthes and Andrea Schrader, and all of my colleagues. Getting to know and working with these people was just wonderful. In particular, I thank Andy, Burak, Daniel, and David for reviewing part of my analysis, Angela, Beni, Niels, and Shaojun for our joint efforts to improve our various software packages, Vasily for helping me to understand more about calorimetry and the physics of hadronic cascades, and Nanda and Beni for lots of shared tea and cookies. I appreciate all the things I have learned from Beni and Alex about our calorimeter and its little secrets and I really enjoyed the nights we spent together to commission this detector and to optimize its performance.

My experiences during the CALICE test-beam activities at Fermilab as a member of the shift crew, detector expert, and eventually run coordinator have been particularly rewarding. Many people have made vital contributions to the success of this measurement program, and I would like to express my sincere thanks to Erik, Rick, Satoru, Katsu, Vishnu, Kurt, Rick, Sven, Karsten, Paul, and all the others I have not named here explicitly.

I warmly thank my family for their continuous assistance in the past years. Furthermore, I give my thanks to Marius, Michi, Lucy, and all of my other friends who have not forgotten me during my absence for business trips around the world and worked-through weekends and who successfully dragged me away from my desk every now and then. Finally, I would like to express my heartfelt thanks to my beloved Karla for her relentless support and her firm trust in me and my capabilities.